SANDIA REPORT

Vortical Structures In Pool Fires: Observation, Speculation, and Simulation

Sheldon R. Tieszen, Vernon F. Nicolette, Louis A. Gritzo,
Jens K. Holen, Doug Murray, Jamie L. Moya

Vortical Structures in Pool Fires: Observation, Speculation, and Simulation

Sheldon R. Tieszen[*], Vernon F. Nicolette[*], Louis A. Gritzo[*],
Jens K. Holen[†], Doug Murray[‡], and Jaime L. Moya[**]

Abstract

This report describes observations, speculations, and numerical simulations of vortical structures in pool fires. Vortical structures are observed in fires with length scales ranging from those that bend millimeter-thick flame zones to those that entrain air many meters from the edge of the fire to its centerline. We propose that baroclinic vorticity generation is primarily responsible for production of rotational motion at small scale and that amalgamation is responsible for the production of large-scale rotational structures from the myriad of small-scale structures. Numerical simulations show that vortical structures having time-mean definitions can be resolved with a Reynolds-Averaged Navier-Stokes (RANS) approach. However, for vortical structures without time-mean definition, RANS is inappropriate, and another technique, such as Large Eddy Simulation (LES), should be employed.

* Unsteady and Reactive Fluid Mechanics Department, Sandia National Laboratories, Albuquerque, NM 87185-0836
† Division Thermodynamics, SINTEF/NTH, Trondheim, Norway
‡ Code 528200D, Naval Air Warfare Center, China Lake, California
** Mechanical and Thermal Environments Department, Sandia National Laboratories, Albuquerque, NM

Acknowledgments

Contents

Figures

Tables

Executive Summary

This report describes observations, speculations, and numerical simulations of vortical structures in pool fires. Fires involve highly nonlinear phenomena from fluid transport to combustion and radiation over length scales from millimeters to many meters. These phenomena are tightly coupled, that is, fire is a *natural balance* between all these physical phenomena. The objective of this study is to gain a qualitative understanding of how vortical flow structures inherent in fires are created and how they control fire phenomena such as air entrainment, combustion, and soot/smoke formation. Entrainment, combustion, and soot/smoke formation are responsible for high temperatures and significant soot/smoke concentrations that, in turn, control radiative heat transfer. The study is motivated by the thermal consequences of fire on hazardous materials and personnel.

We present observational data from fire experiments conducted at the CT4 test facility at the Naval Air Warfare Center (NAWC), China Lake, California (for the Defense Special Weapons Agency) and at the Lurance Canyon test facility at Sandia National Laboratories (SNL), Albuquerque, New Mexico (for the Department of Energy). Visualization of the luminous soot emissions and the path of the smoke particles provides useful insight into the underlying fluid flow that is a consequence of a fire. Large-scale, coherent, vortical structures are clearly present in the fire, with some as large as the fire diameter. In addition to the vortical structures present in calm conditions, a crosswind will form columnar vortical structures on the leeward side.

We propose that three mechanisms are primarily responsible for turbulent flow structures in fires. The first is baroclinic vorticity generation, which produces rotational motion at small scale. Baroclinic vorticity generation is the consequence of misalignment of density and pressure gradients. The second is amalgamation, which produces larger-scale rotational structures from the smaller ones, and the third is the turbulent cascade from larger to smaller structures. The largest vortical structures dominate the entrainment of air into the fire plume, but then stirring and mixing occur over the complete range of scales down to molecular level.

The length and time scales over which these processes occur are beyond the current computer capability to resolve. Therefore, using engineering judgement, we assume a model behavior for all processes below a certain length scale and compute the large-scale effects. When the larger vortical structures exhibit a meaningful time-average value, the established Reynolds-Averaged Navier-Stokes (RANS) technique is successful. However, when the structures are very transient, a technique that employs less time-averaging, such as Large Eddy Simulation (LES), is a better approach.

Introduction

The ability to predict the consequence of fire is hindered by the number and complexity of the phenomena inherent in fires. Fires involve numerous phenomena that span convective-and-diffusive, length-and-time scales including turbulent fluid motion, entrainment, stirring and mixing of scalars, combustion, soot and smoke formation, and participating media radiation. The phenomena are highly nonlinear. For example, the nonlinear advection term in the Navier-Stokes equations for the fluid motion results in a full spectrum of fluid length scales associated with turbulent flow. As a result, even in "steady state," the velocity field is transient and three dimensional. This behavior occurs because of the distribution of turbulent eddies, or vortical structures, which are nonhomogeneous, intermittent, and transient. Further, combustion rates are exponentially dependent on temperature, and radiation heat transfer is dependent on temperature to the fourth power.

The phenomena in fires are tightly coupled. Fire is the *natural balance* between all physical phenomena. This feature is different from most combustion phenomena in which some external control exists on either the momentum or scalar flow-fields (that is, the inlet velocities or fuel/air ratios). Fire is not a process with inputs and outputs in the usual engineering sense; rather, it is a balance point that is a result of the circular closure of the mechanisms. For example, heat flux to a liquid pool surface results in fuel vaporization. The vaporized fuel mixes with air and ignites, which results in flames. Radiative heat transfer from the flames results in a heat flux to the liquid pool surface, which results in fuel vapor, and the process repeats itself. If any change occurs in any of the flow conditions, that is, geometry, wind, fuel, etc., the balance point will shift to a new equilibrium point. The fire will then consist of different combustion rates, temperatures, and radiative heat fluxes. In the same vein, the vortical structures found at all length scales in a fire can be interpreted as being a simultaneous cause and a consequence of the heat release in a fire.

While all fires are complex and involve many phenomena, this report is limited to large, turbulent liquid-hydrocarbon pool fires. Large, liquid-hydrocarbon pool fires present a risk in petrochemical storage and processing facilities and transportation systems that contain large amounts of liquid hydrocarbons. Typical transportation systems are aircraft and large ground vehicles. Accidents involving the rupture of fuel tanks and subsequent ignition form the conditions for a pool fire (Tieszen, 1995; Tieszen and Attaway, 1996). Defining the risk involved in such accident scenarios requires the definition of both the probability of occurrence and the consequence. The probability of occurrence is often obtained from historical accident data for the appropriate industry or mode of transportation. The consequence depends on the end-response of concern. In air transport, for example, the response of both hazardous (chemical, biological, nuclear) cargo and people can be of concern. Hazardous cargo is often shipped in containers that can survive considerable impact loads but can be severely damaged by the long-duration, high incident-heat-fluxes associated with a pool fire. Heat flux from a fire is also a threat to people, although they are often overcome by smoke and toxic gases prior to being burned and are relatively sensitive to impact forces.

To determine the heat flux to a person or an object, it is necessary to understand the physical mechanisms in a fire that have a dominant, first-order effect on the radiative heat transfer from a fire. Mechanisms such as air entrainment, combustion, and soot/smoke formation have a first-order effect on the temperatures and radiative transport properties. Underlying these mechanisms is the turbulent fluid motion that creates, and responds to, the large temporal and spatial fluctuations inherent in fires. It is important to understand the nature of the underlying turbulence in fires in order to understand the magnitude of the heat flux to a person or object from a fire.

The objective of the present study is to gain a qualitative understanding of how time-dependent vortical flow structures inherent in turbulent flows are created in fires and how they affect the fire phenomena important to heat transfer such as entrainment, smoke formation, and combustion. To achieve this understanding, three approaches have been taken. The results of these approaches form the next three sections of this report. The first approach is experimental. Qualitative observations of the various length and time scales of the vortical structures were made using flame zones and smoke layers as flow visualization mechanisms. The second approach involves speculation and hypothesis as to the underlying mechanisms based on phenomenological reasoning. The hypotheses are evaluated against the observations. The third approach involves numerical simulation of fires. Engineering models based on Computational Fluid Dynamics (CFD) approaches have recently become available for the study of fires. In the final section of this report, conclusions are drawn based on the approaches taken.

Observation of Vortical Structures

In this section, we present observational data from fire experiments conducted 1) at the CT4 test facility at the Naval Air Warfare Center (NAWC) at China Lake, California, for the Defense Special Weapons Agency and 2) at the Lurance Canyon test facility at Sandia National Laboratories (SNL) in Albuquerque, New Mexico, for the Department of Energy. Both facilities conduct tests with liquid jet fuel floated on a pool of water. The pool at CT4 is circular with a diameter of 18.9 m, while the pools at Lurance Canyon are rectangular with dimensions of 9 m × 18 m and 2 m × 6 m. The observational data used in this study are qualitative; however, quantitative temperature and heat flux data were obtained for the tests and are available upon request from the authors.

Limitations on print media make it difficult to present time-dependent phenomena such as the motion of the flow under the influence of vortical structures. To compensate partially, arrows have been drawn on the photos as appropriate to indicate features in the flow. Primarily, 35-mm still photography was used to capture the images. The film used was typically Kodak color print film with an ASA of 200, although some ASA 400, 100, and 25 were also used. For time-averaged photographs, differing levels of neutral density filters were also employed. Some video was also employed and is available upon request from the authors.

The resulting images are a combination of light from two sources. For soot that is sufficiently hot, luminous emission from the fire (basically a participating medium) results in the oranges and yellows interpreted as flame zones. The remaining colors are from the scattering of sunlight from the surrounding objects. Smoke is black because the soot temperature is too low for the emission to occur within the visible regime, and it absorbs sunlight in the visible wavelengths.

Visualization of the luminous soot emissions and the path of the smoke particles provides useful insight into the underlying fluid flow that is a consequence of the fire. Since the images are the result of emission and scattering of light from within a participating medium, one must keep in mind that one is seeing an optical depth or so into the fire at the wavelength of the light that is captured on the film. Also, what the eye sees when looking at a fire and what the camera sees can be different, even for the same wavelengths of light. This phenomenon occurs because the mind does not resolve time scales below about 1/15 of a second, while the camera used can have an arbitrarily short or long time averaging window up to several seconds (or more with the correct filters) and down to 1/2000 of a second (for the camera used).

For convenience of discussion, the observations are presented according to the size or scale of the vortical structures with the largest scales first. It is to be understood that all scales exist in each flow. The vertical direction beginning at the base of the fire will be referred to as the axial direction. The radial direction is from the center of the fire outward, and the azimuthal direction is perpendicular to both the radial and axial directions. The images shown in this section are not unique to the test facilities chosen but are com-

mon to all fires of this type and have been observed as long as man has been observing fires. Our purpose in presenting the images is to lead into the discussion of the physical mechanisms that cause the vortical structures to exist and to assess their impact on the thermal hazard posed by the fire.

Large-Scale Structures

The largest scale vortical structures observed in a fire are on the order of the fire diameter in scale. Observation of structures in pool fires shows distinctly different structures present in fires with and without a crosswind. These scenarios will be discussed separately.

No Crosswind

Without the presence of a crosswind, the largest rotational structures appear as horizontal rings or ring arcs. Figure 1 shows large organized structures that are almost symmetric, indicating that the largest vortical structures in the flow can become sufficiently coherent to form complete rings. The photograph in Figure 1 is not typical however; more commonly, only ring arcs or segments can be seen. Figures 2 through 4 are more typical of the structures seen in a fire. Figure 2 shows that the segment is coherent over about half the periphery of the fire. Figures 3 and 4 show structures that have transverse dimensions on the same order as their axial and radial dimensions. They appear as smoke or flame balls.

It was observed that structures having large characteristic length scales on the order of the fire radius begin to develop a minimum of one radius from the fire base. At elevations closer to the toe of the fire, smaller structures were observed. In general, it was observed that the scale of the structures increases as distance increases from the toe of the fire. The structures are coherent such that in a video picture, the structures can be tracked for some distance. However, pairing is evident, so two axially adjacent smoke or flame balls will pair up and become a larger one. Therefore, the scale of the large rotational structures appears to increase with increasing distance from the toe of the fire.

Without wind, the formation and growth of the structures from the toe of the fire can be quite periodic and large. This behavior is typically referred to as puffing. It has been observed to occur over a large range of length scales in buoyant flows including large fires (Cetegen and Ahmed, 1993). Figure 5 shows eight frames of a video sequence in which a large puff is observed forming and passing downstream. In the eighth frame, the new "puff," or large ring vortex-like structure, is being formed under the smoke layer at the same elevation as observed in the first frame. Puffing can also be characterized by the motion near the toe of the fire. As seen on the lower left of each frame in Figure 5, the flame zone near the toe of the fire is nearly horizontal, while the ring-vortex is low (as in the first and last frames). The base of the fire begins to stand up more towards vertical as the puff moves away from the base of the fire.

Figure 1.   Large Ring Vortices.   SNL Lurance Canyon Facility, 3/13/87; conducted in the 9 m by 18 m rectangular pool in calm conditions.
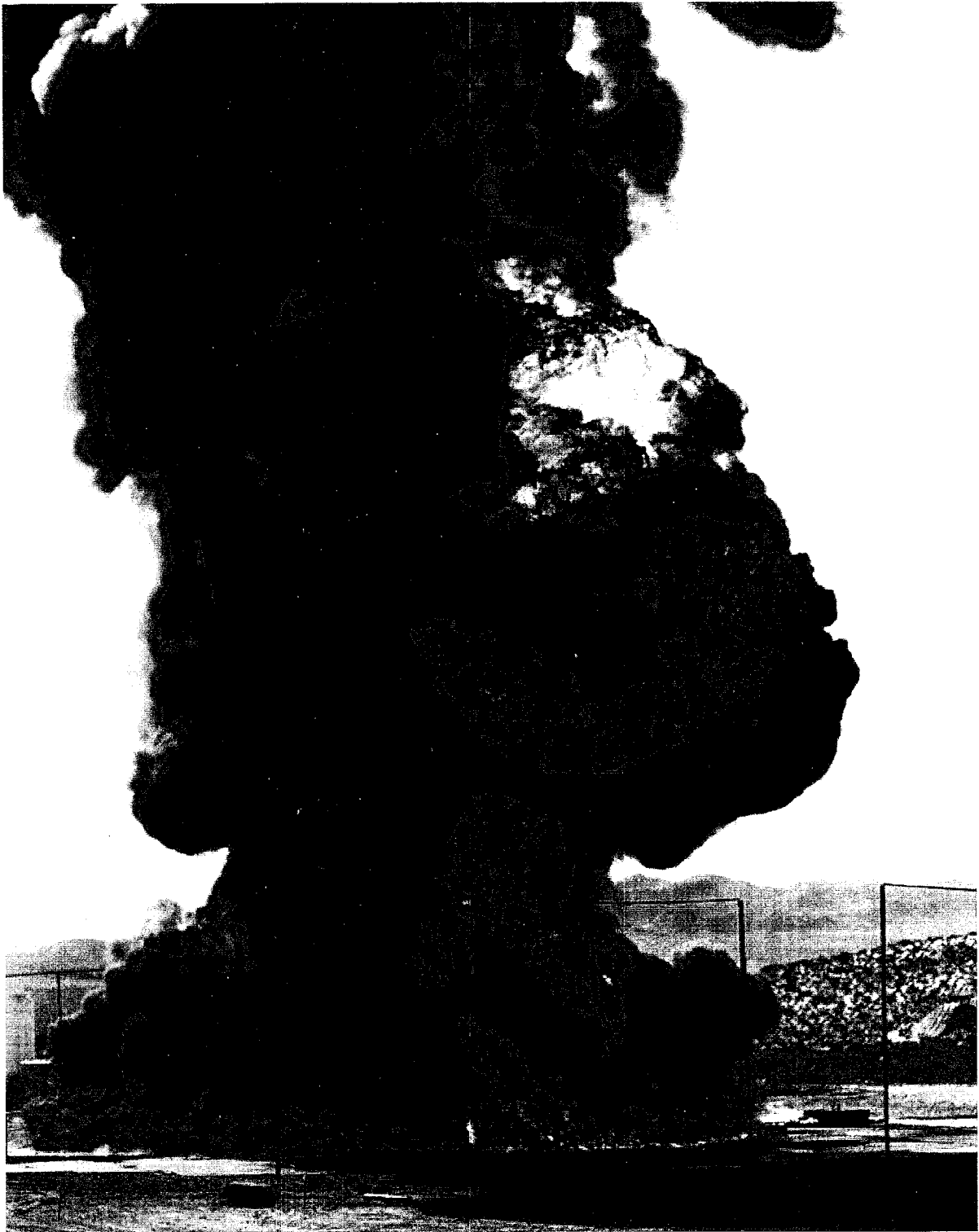
Figure 2.   Large Ring Arc. NAWC at China Lake, 1/28/94; conducted in the 18.9 m
diameter pool with a crosswind of about 0.7 m/s from approximately 20° off
the camera normal.

Figure 3.   Ring Segments. NAWC at China Lake, 1/28/94; conducted in the 18.9 m diameter pool with a crosswind of about 0.7 m/s from approximately 20° off the camera normal.

Figure 4.   Additional Ring Segments. NAWC at China Lake, 1/28/94; conducted in the 18.9 m diameter pool with a crosswind of about 0.7 m/s from approximately 45° off the camera normal.
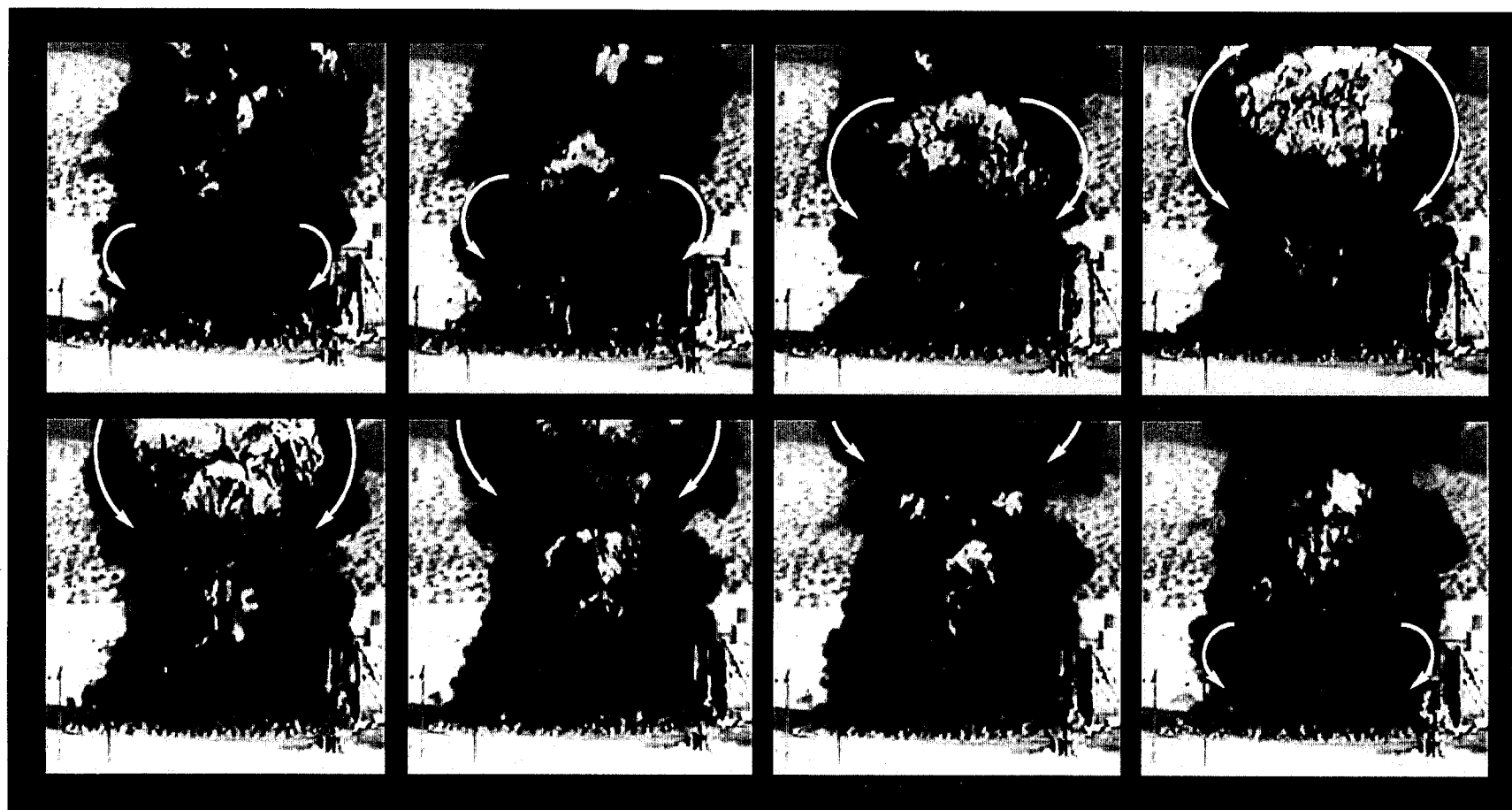
Figure 5.   Video Frames Sequence Showing a Fire Puffing. NAWC at China Lake, 9/16/93; conducted in the 18.9 m diameter pool in calm conditions. Time between frames is 1/3 second.

It was also observed that the rotational structures formed without the presence of a crosswind, while coherent, are continuously moving and thereby produce no time-mean effect at a fixed location. In this sense, they have no time-mean definition. While the rotation of the structure may be steady in a temporal sense, the position of the structure is not because it is being continuously advected up the fire plume. Therefore, in any instantaneous picture, such as those in Figures 1 through 4, one will find large rotational structures that have an azimuthal component of rotation. However, if one chooses a long duration exposure, then the photographs show no sign of the rotational structures. A typical example is shown in Figure 6, which has a duration of 30 seconds. A long duration means an exposure time longer than several lifetimes of the observed rotational structures. Technically, long exposures do not time-average but time-integrate the light reaching the film. However, for the purpose of establishing the unsteadiness of the rotational structures, long exposures can be considered as representing a time-average. The purpose for observing the relative steadiness to the vortical structures is that turbulence models typically imply some time-averaging. This aspect will be discussed in the Numerical Simulation section.

In a Crosswind

In a crosswind, the vortical structures that formed in no wind conditions are still formed on the upwind (or windward) side of the fire. In addition, new rotational structures are formed on the downwind (or leeward) side of the fire and appear to have a relatively steady mean. It should be noted that the wind speeds for this study are reported from a single measurement station although multiple measurements were made in many tests.

On the upstream side of the fire, vortical structures are observed that appear to have characteristics very similar to those formed in the absence of a crosswind. The rotational structures increase in scale from the toe of the fire as seen in Figure 7. In Figure 7, the wind is from the left and the toe of the fire is just out of view on the left side of the photograph. The increasing scale of the rotational structures is best seen along the upper edge of the fire against the background. Figures 8 and 9 show the same pattern of increasing scale as the structures move away from the toe of the fire. Figure 8 is an intermediate-range view, while Figure 9 is a longer range view that includes more smoke plume.

From video sequences, the upwind structures appear periodic because the structures pass a given point in space with a relatively constant frequency. However, their effect on the toe of the fire may not be as pronounced as in the no-wind case. Because of the crosswind, the structures are quickly advected downstream away from the toe before growing to large length scales. Because the term "puffing" is applied to fires with no crosswind and not, to the authors' knowledge, to fires in a crosswind, it appears that the effect of the structures on the toe of the fire is the distinguishing feature of puffing rather than the formation of large vortical structures.

The large vortical structures are coherent in that they can be tracked until they visually appear to pair with, or roll up into, each other. This pairing phenomena can be observed as occurring for several generations in which a paired structure pairs with another paired structure. As in the no-wind case, the rotational structures formed on the upstream edge of
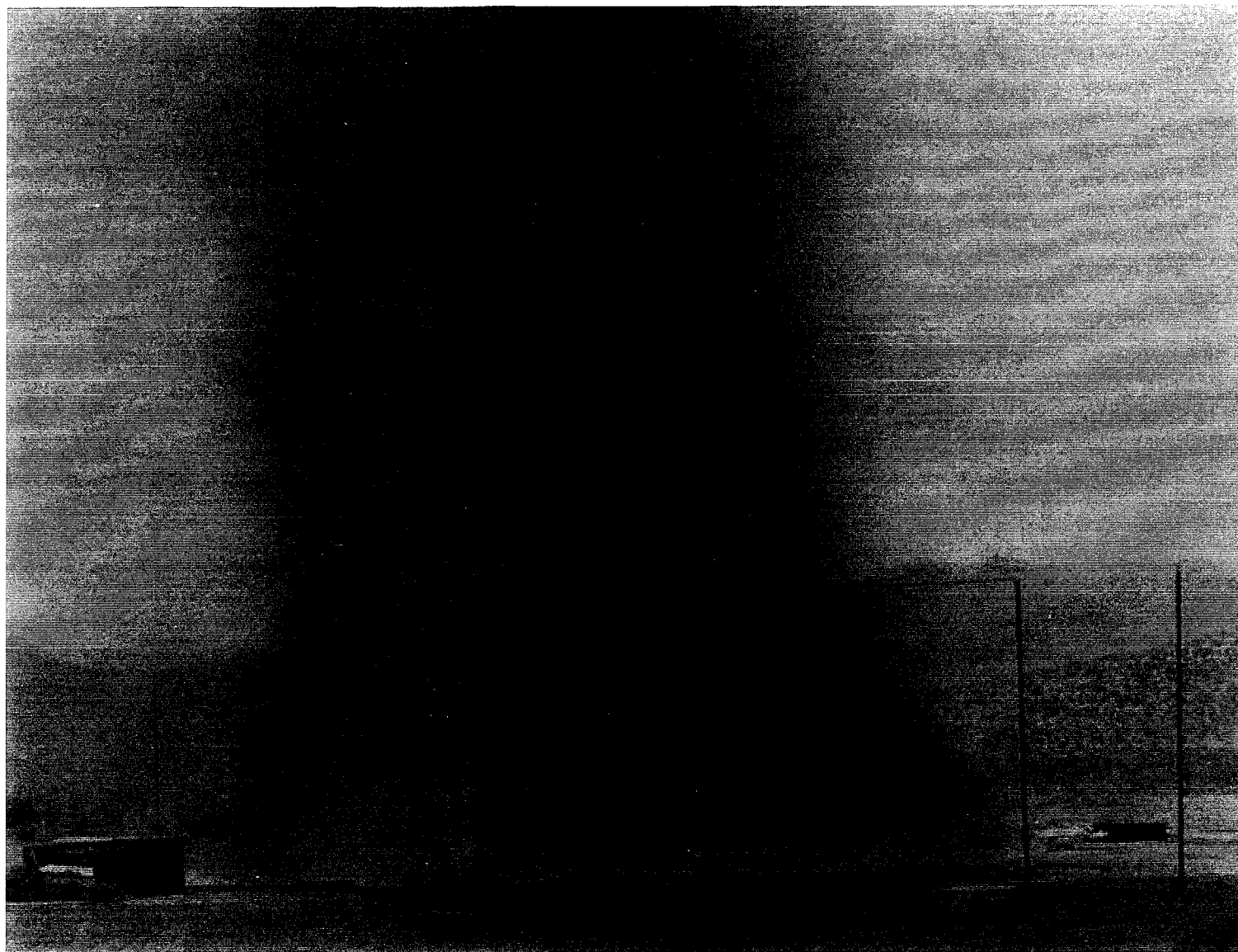
Figure 6. Time-Averaged Photograph of a Fire. NAWC at China Lake, 1/28/94; conducted in the 18.9 m diameter pool with a cross-wind of about 0.7 m/s from approximately 20° off the camera normal. Exposure time is 30 seconds.

13

Figure 7. Toe of a Fire Showing Rotational Structures that Increase in Scale with Distance from the Toe of the Fire. NAWC at China Lake, 3/18/94; conducted in the 18.9 m diameter fire test facility with a 3.5 m/s crosswind from approximately 90° off the camera normal.

14
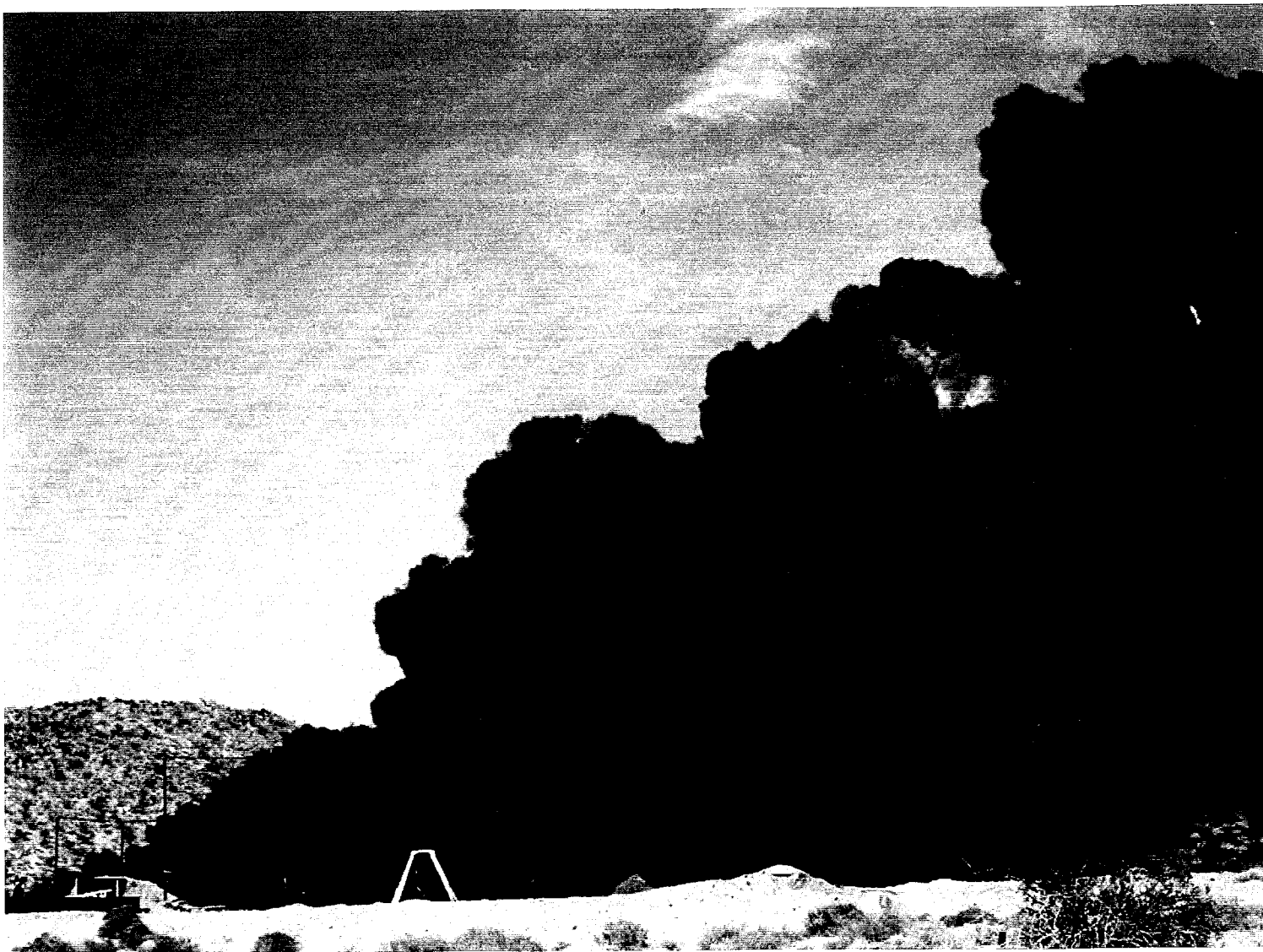
Figure 8. Intermediate Range View of a Fire Showing that Upstream Structures Increase in Scale with Increasing Distance from the Toe of the Fire. NAWC at China Lake, 3/18/94; conducted in the 18.9 m diameter pool with a 5.5 m/s crosswind from approximately 60° off the camera normal.
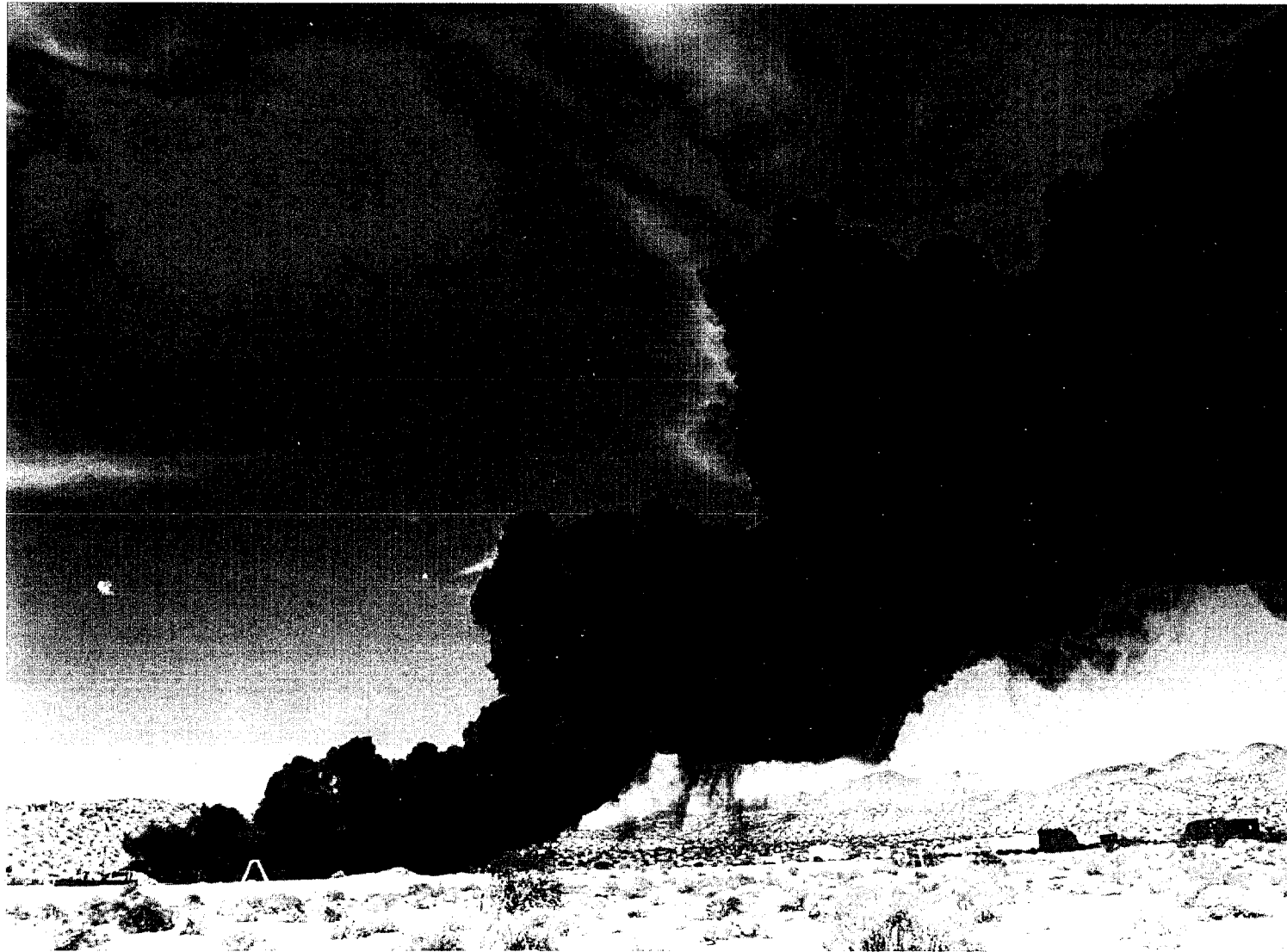
Figure 9. Long-Range View of a Fire Showing that Upstream Structures Increase in Scale with Increasing Distance from the Toe of the Fire. NAWC at China Lake, 3/18/94; conducted in the 18.9 m diameter pool with a 5.5 m/s crosswind from approximately 60° off the camera normal.

the fire do not have a time-mean definition at a fixed location because the rotational structures are advected downstream. Therefore, a long-duration photograph will not show their presence. Figure 10 shows the absence of such structures on the upwind side of the fire. The photograph has been averaged over 4 seconds.

The vortical structures formed on the downwind side of the fire are distinct from those formed on the upwind side of the fire. On the downwind side, the dominant direction of rotation is axial. The structures are quite coherent and appear as tall counter-rotating columns. Sometimes two columns exist (Figure 11), and other times only one column exists (Figure 12). In each case, the axis of rotation is oriented axially along the plume direction.

The columnar rotational structures formed on the downwind side of a fire have a time-mean definition, although they are not completely steady. Figures 13 and 14 show time exposures of 1 second and 0.5 second, respectively. The dominant direction of the smoke and flame streaks is upward. However, the streaks are not completely vertical, but sweep inward from each side. This means that over the time period of the photographs, the vortical structures have an associated time-mean rotational velocity. Neither photograph is averaged over sufficient time to capture the passage of more than one of the very large-scale structures high in the fire. Therefore, Figure 13 shows the ring arc formed on the front side of the fire rolling around the back into the columnar vortices just above the luminous zone. Figure 14 shows that sufficient rotation can be generated to divide the plume into two counter-rotating plumes. This phenomenon has also been observed in nonfire generated plumes (A. Ghoniem, personal communications, Jan. 1995).

Video was taken at the base of the fire for the test conducted at the NAWC, China Lake, on 1/28/94. The test had crosswinds of 2 - 4 m/s during the first few minutes after ignition in the 18.9 m diameter pool. Observations showed that while the columnar vortices have a long lifetime, they are not completely stable. Once formed, a columnar vortex will slowly grow in size. As it grows, the base of the vortex will move farther downstream from the fire. Instantly, the fire in the vortex will extinguish and further visualization is not possible because of the lack of a flame or smoke. Typically, the second columnar vortex (shown in Figure 11) will grow in size, while a new columnar vortex will begin forming where the original one formed. The process will repeat itself with the vortices on each side growing, having their base move downstream of the fire and then blowing out. It is not clear why the vortices blow out; however, this may occur because as the vortices moved downstream from the pool, they could no longer entrain fuel vapor from the pool.

The location of the columnar vortices in a crosswind can occur either at the lee side of the pool or considerably downwind, depending on the strength of the crosswind. The higher the wind velocity, the larger both the tilt of the flame plume and the ground surface area covered by the fire. For example, Figure 15 shows the "footprint" (soot outline) of a fire with a 3.0 m/s to 7.0 m/s crosswind.

This topic has been limited to single fires with wind conditions not affected by terrain producing a spin. Under certain wind and terrain conditions, the entire fire can be spun into a single columnar vortex. This condition is termed a "fire-whirl" and produces heat fluxes

Figure 10. Time-Averaged Photograph of a Fire in a Crosswind. Vortical structures formed on the upstream edge of the fire have no time-mean definition. NAWC at China Lake, 7/13/94; conducted in the 18.9 m diameter pool with a 2.4 m/s crosswind from approximately 90° off the camera normal. Exposure time is 4 seconds.
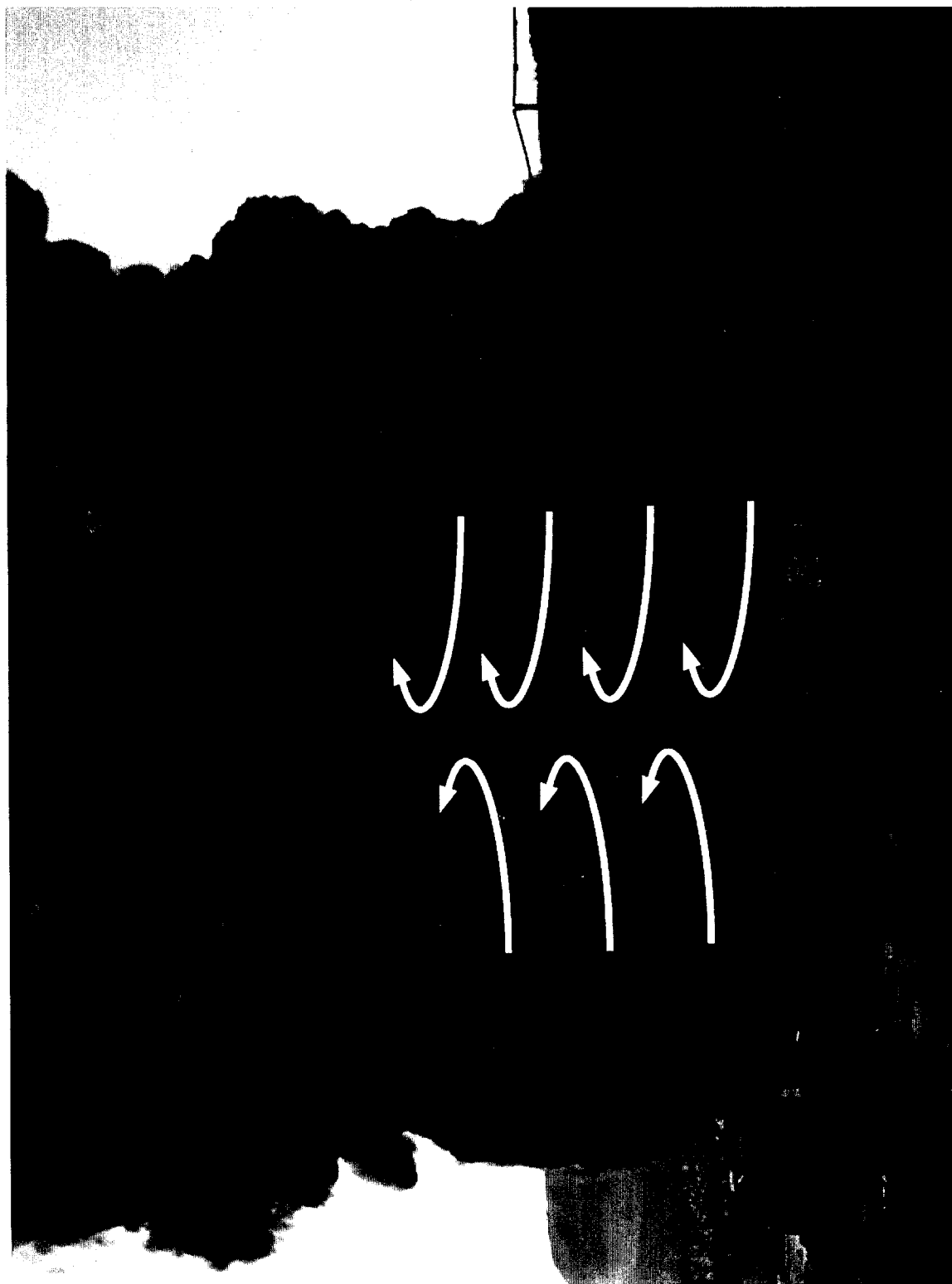
Figure 11. Columnar Rotational Structures are Formed on the Downwind Side of Fires in a Crosswind. Example of two structures. NAWC at China Lake, 1/28/94; conducted in the 18.9 m diameter pool with a 0.7m/s crosswind from approximately 60° off the camera normal.

Figure 12. Columnar Rotational Structures are Formed on the Downwind Side of Fires in a Crosswind. Example of a single structure. NAWC at China Lake, 1/28/94; conducted in the 18.9 m diameter pool with a 0.7 m/s crosswind from approximately 60° off the camera normal.

Figure 13. Time-Averaged Photograph of Columnar Structures Formed on the Down-wind Side of a Fire in a Crosswind. First example. NAWC at China Lake, 9/29/94; conducted in the 18.9 m diameter pool with a 2.5 m/s crosswind from approximately 0° off the camera normal.

Figure 14. Time-Averaged Photograph of Columnar Structures Formed on the Down-
wind Side of a Fire in a Crosswind. Second example. NAWC at China Lake,
9/29/94; conducted in the 18.9 m diameter pool with a 2.5 m/s crosswind
from approximately 0° off the camera normal.
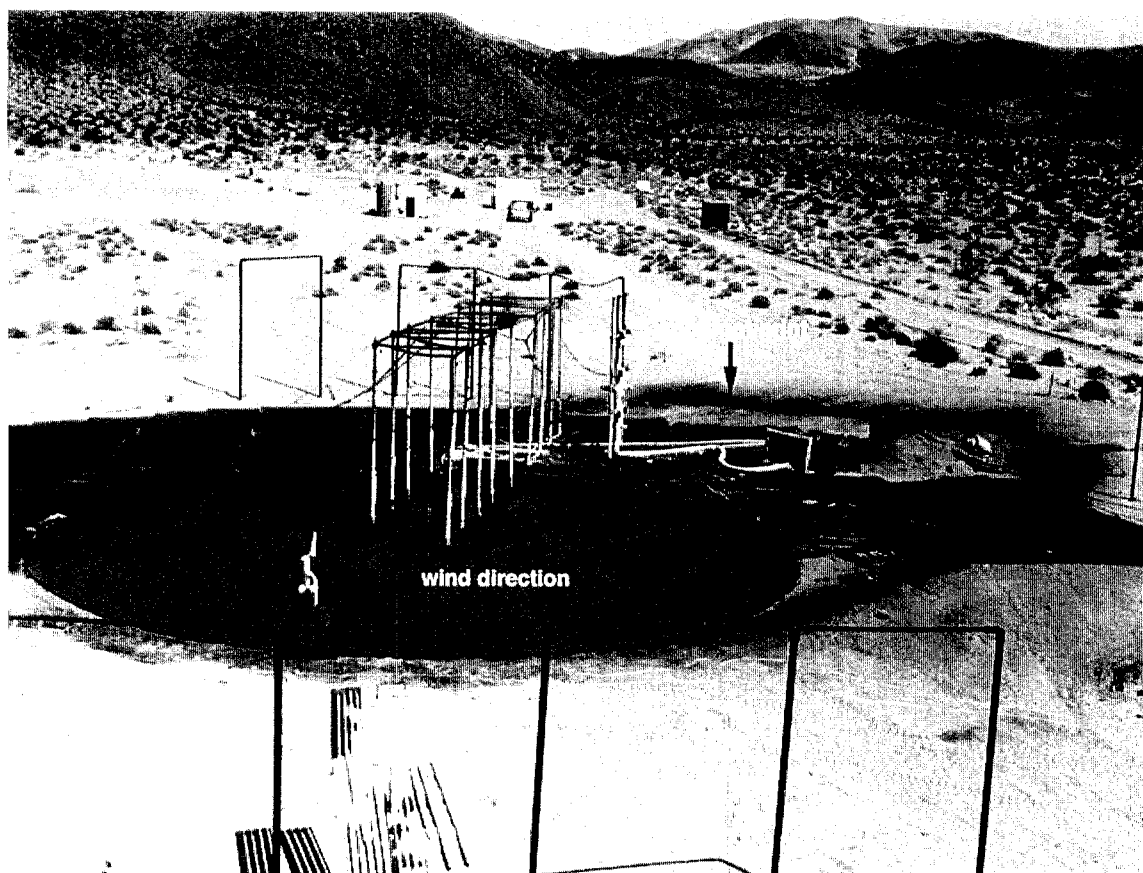
Figure 15. Footprint of a Fire in a Crosswind. The soot outlines the base of the fire on the ground. The columnar vortices can be located significantly downwind of the pool. NAWC at China Lake, 3/18/94; conducted in the 18.9 m diameter pool with a crosswind between 3.0 and 7.0 m/s.

that are particularly destructive. (See Soma, S. and Saito, K., 1991 for a description of the phenomena.)

Intermediate-Scale Structures

Intermediate-scale structures are most visible in the smoke layer surrounding the fire, as shown in Figure 16. Similar effects can be seen from either the smoke or flame texture in Figures 1 through 4, which show smaller scale structures existing within the larger scale structures. In some cases, it is clear from video observations that the largest structures are composed of intermediate scale structures in the process of pairing into the larger structure (see Figures 7, 8, and 9). Other cases are not as obvious. However, the common view of turbulence suggests that smaller structures are the result of the unstable cascade from larger structures. This process is apparently not as easily seen as the pairing process, in which smaller structures appear to become larger. The pairing process is readily visual-

Figure 16. Photograph Showing Intermediate-Scale Rotational Structures. The fire and smoke form "spherical" structures that increase in scale with increasing elevation. NAWC at China Lake, 3/18/94; conducted in the 18.9 m diameter pool with a 3.0 m/s crosswind approximately 30° off the camera normal.

ized from video images of the smoke layer, while the unstable cascade is not. The burnout of an eddy and its roll-up into a large smoke-filled structure is shown in Figure 17.

Transient vortical structures are also observed in the wake of a crosswind fire (as shown in Figures 18 and 19). The wake vortices are seen by dust entrained into the vortex rather than smoke. Dust entrainment indicates that the vorticity source is from the ground rather than the fire or fire plume. This is consistent with the explanation of the phenomena by Fric and Roshko, 1994 for wake vortices behind jets in crossflow. The difference in phenomena between a fire and a jet should not affect the formation of wake vortices. The wake vortices are infrequently observed in fires, presumably because the vorticity strength must be high to entrain sufficient dust to make the wake vortices visible. Vortices of this type were observed more frequently from the rectangular pool at the Lurance Canyon test facility than from the circular pool at the NAWC CT4 test facility. It is unclear what effect geometry has in the formation of these vortices. Very large wake vortices have also been observed in very large fires (Soma, S., and Saito, K., 1991).

Partially or totally engulfed objects are another source of vortical structures in fires. The range of scale and complexity of possible object shapes allows only general observations. Objects can significantly affect the fire. The effect becomes more apparent with increasing wind speed. The heat flux measurements taken downstream of a large object in a 10 m/s crosswind were approximately a factor of two higher because of the object (Gritzo et al., 1995). The high heat fluxes indicate enhanced mixing of the fuel and air, resulting in more efficient combustion. The enhanced mixing can be attributed to the turbulence induced by the object in crossflow.

The effect of objects within a fire is important but the visual changes in the turbulent structures, even from the presence of large objects, can be relatively subtle. Objects affect the mean flow because they represent a blockage. The effect on the mean flow of a large 4.3 meter diameter cylinder placed just above and downstream of the pool center is shown in Figures 20, 21, and 22. However, a comparison of Figure 20 with Figure 8 shows no vortical structures unique to the object. The same vortical structures, with an azimuthal rotation, appear on the upstream side of the fire with or without the object in the flow. Columnar vortices appear on the downstream side of the fire with or without an object, as shown by comparing Figure 11 to Figure 22. In Figure 22, the columnar vortices are tilted more toward the horizontal because of the higher wind. However, the presence of the obstacle elevates the base of the columnar vortices above the ground. This allows an air layer to exist under the vortices and directly in back of the object. The air layer may account for the enhanced mixing. Or vorticity shed from the object boundary layer at smaller length scales may account for the enhanced mixing. Because the interactions are complex, quantitative research beyond the current study is needed.

The effect of objects on heat fluxes can be seen at high wind speeds; however, high winds are not required. Even with no wind present, a fire will create its own inflow velocity, as shown in Figure 5. To the right of the base of the fire is a large plate at the lip of the pool (used for a calorimeter study, Gritzo et al., 1994). The plate interrupts the radial inflow into the fire and may act as a flame holder. The columnar vortices on the downstream

25
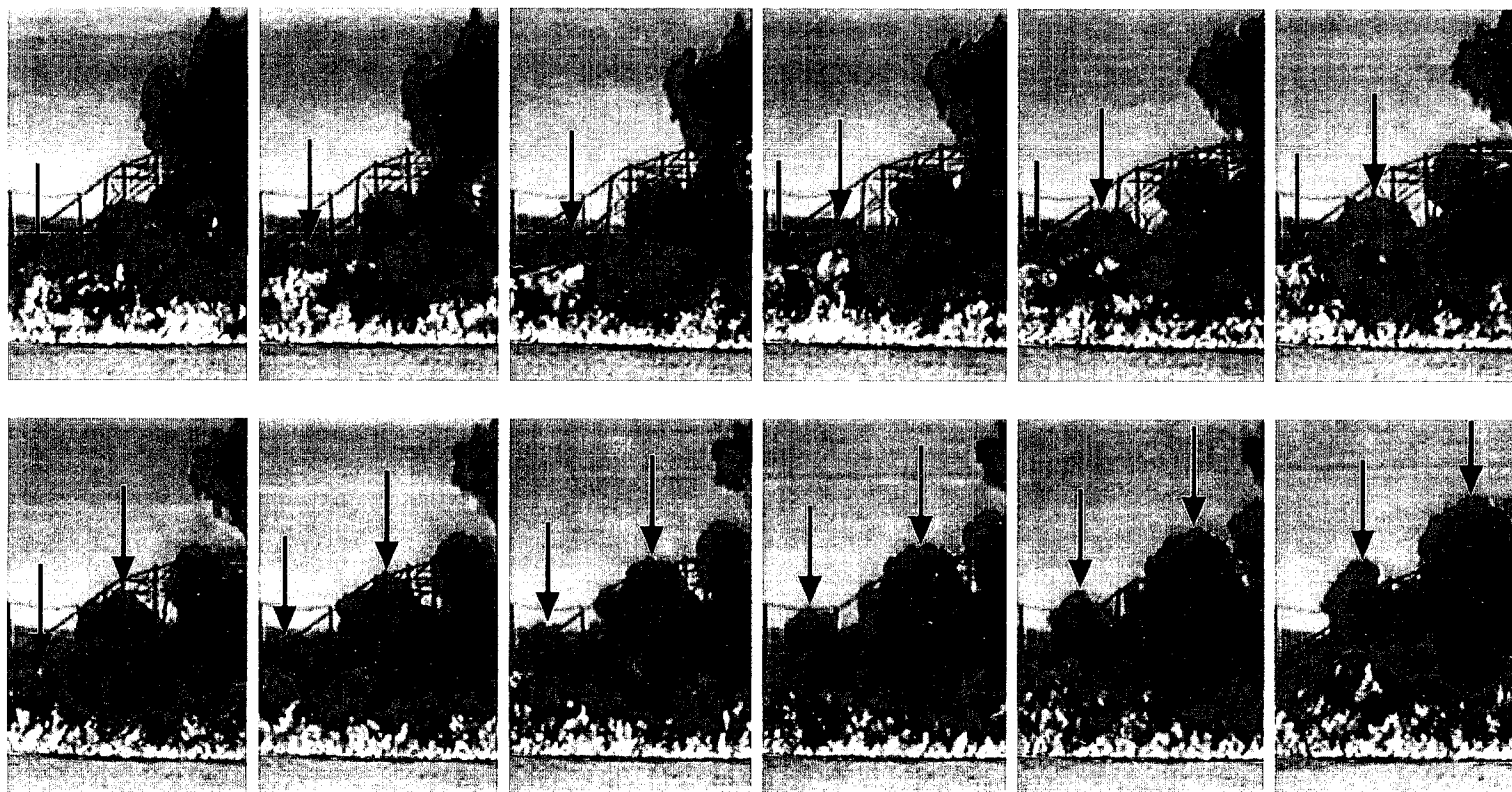
Figure 17. Sequence of Video Frames Showing the Formation of Smoke. NAWC at China Lake, 8/12/93; conducted in an approximate 1.0 m/s crosswind in the 18.9 m diameter pool. Time between frames is 0.1 second.

Figure 18. First Example of Wake Vortices. SNL at the Lurance Canyon Facility, 1986. Conducted in the 9 m by 18 m rectangular pool.

Figure 19. Second Example of Wake Vortices. NAWC at China Lake, 8/23/94; conducted in the 18.9 m diameter pool with a 1.3 m/s crosswind approximately 90° off the camera normal.

Figure 20. Effect of a Large Object on a Fire in a Crosswind. NAWC at China Lake, 1/11/95; conducted in the 18.9 m diameter pool with a 4.0 m/s crosswind from approximately 90° off the camera normal.
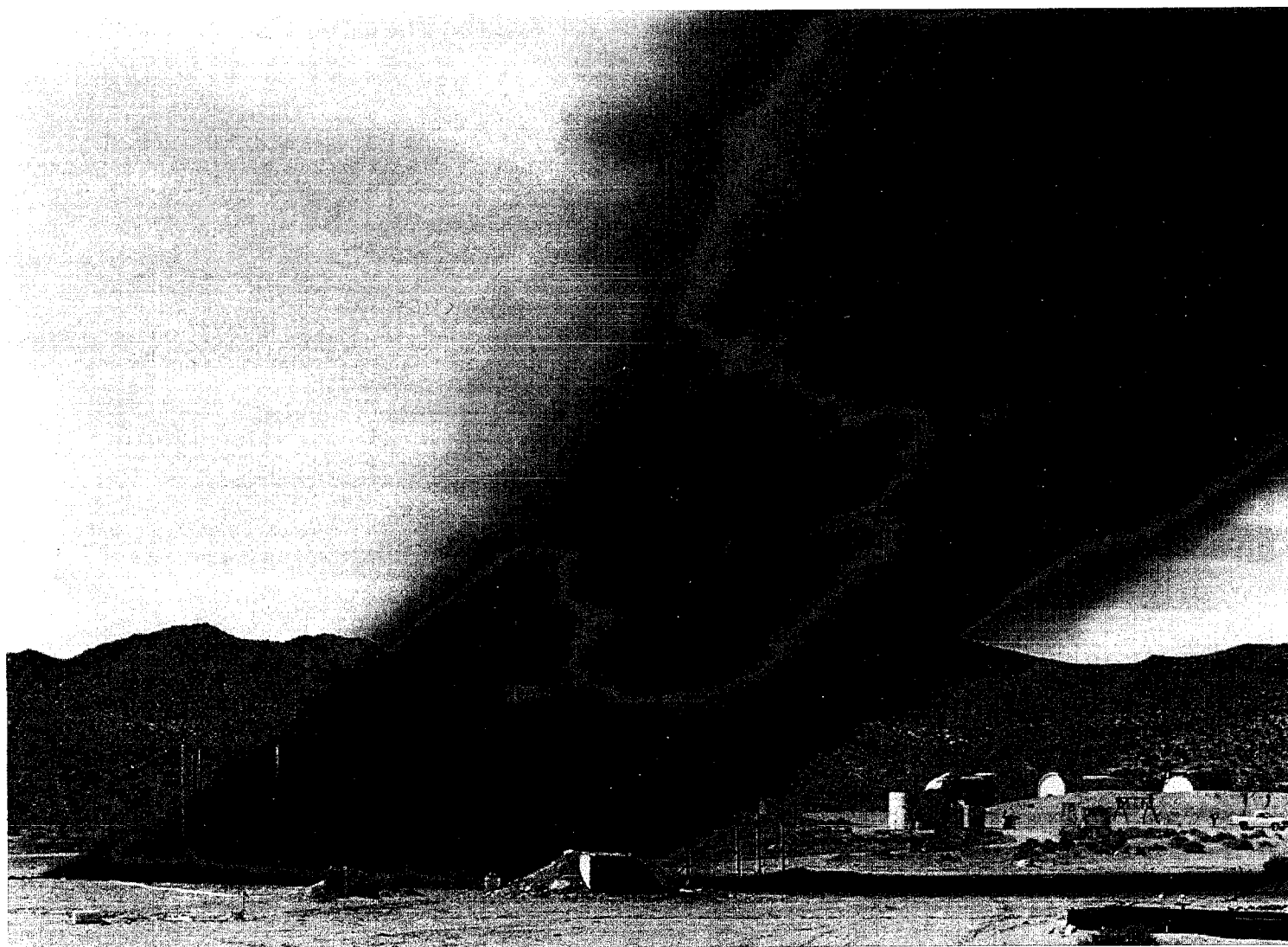
Figure 21. Time-Average Photograph of a Large Object on a Fire. NAWC at China Lake, 1/11/95; conducted in the 18.9 m diameter pool with a 4.0 m/s crosswind from approximately 90° off the camera normal. Exposure time is 4 seconds.
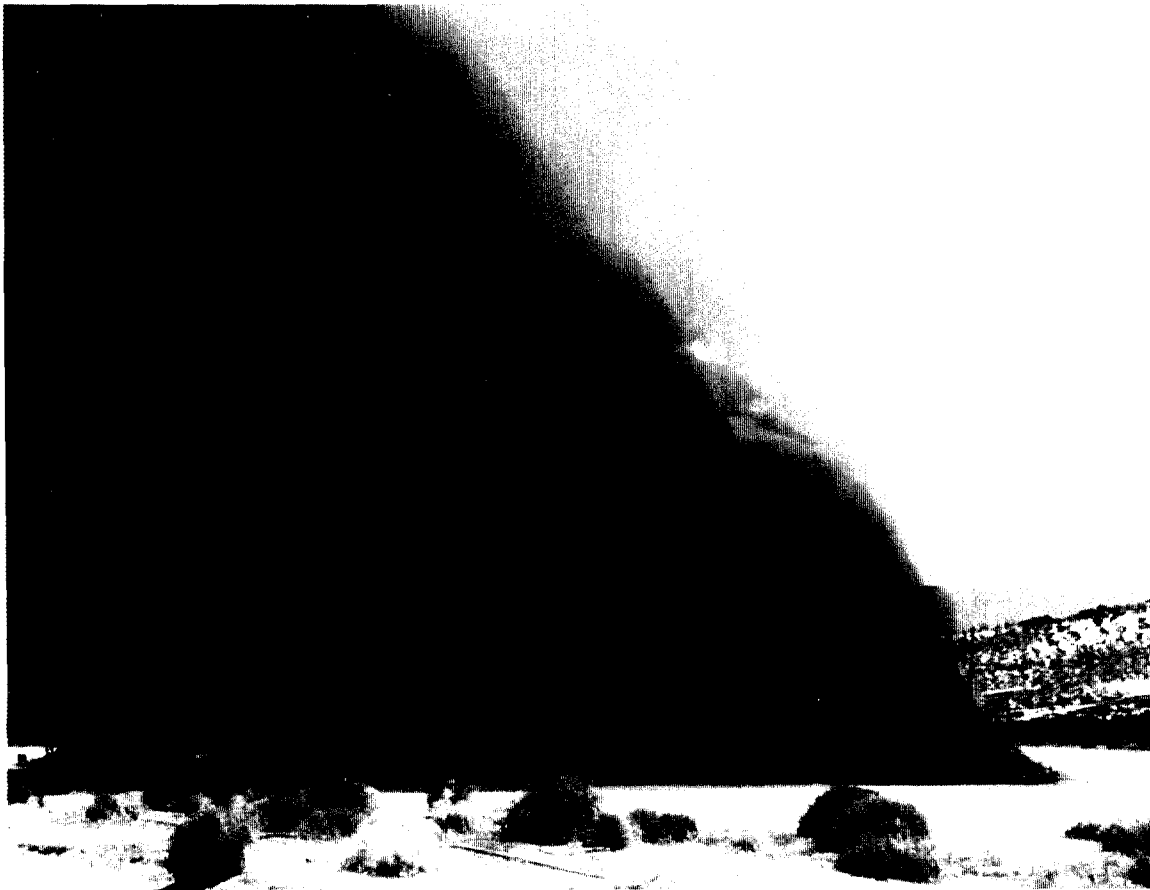
Figure 22. Time-Average Photograph of the Wake of a Large Object on a Fire. NAWC at China Lake, 4/13/95; conducted in the 18.9 m diameter pool with a 10.0 m/s crosswind from approximately 45° off the camera normal. Exposure time is 8 seconds.

edges of the plate, that is, facing the fire, are the result. The effect is seen most clearly in the third and fourth frames as a bright yellow column on the near edge of the plate. The puffing action is so strong in Figure 5 that even the columns on the plate puff.

Small Scale Structures

The smallest scale of rotational structure that can be observed by using smoke and flame sheets as indicators is the scale of structure that causes the flame sheets to bend, as shown in Figures 23 and 24. In both figures, as the flame sheets in the photographs appear smooth over much surface area but bend sharply between the smooth areas. The bends may be from diffusional instabilities or small vortices. If the bends are caused by small vortices, then they are relatively widely spaced, because the space between the bends in the flame sheet are generally much larger than the diameter of the bends.

Figure 23. Small-Scale Vortical Structures Wrinkle the Flame Front. SNL at the Lurance Canyon Facility, 6/16/94; conducted in the 2 m by 6 m rectangular pool.
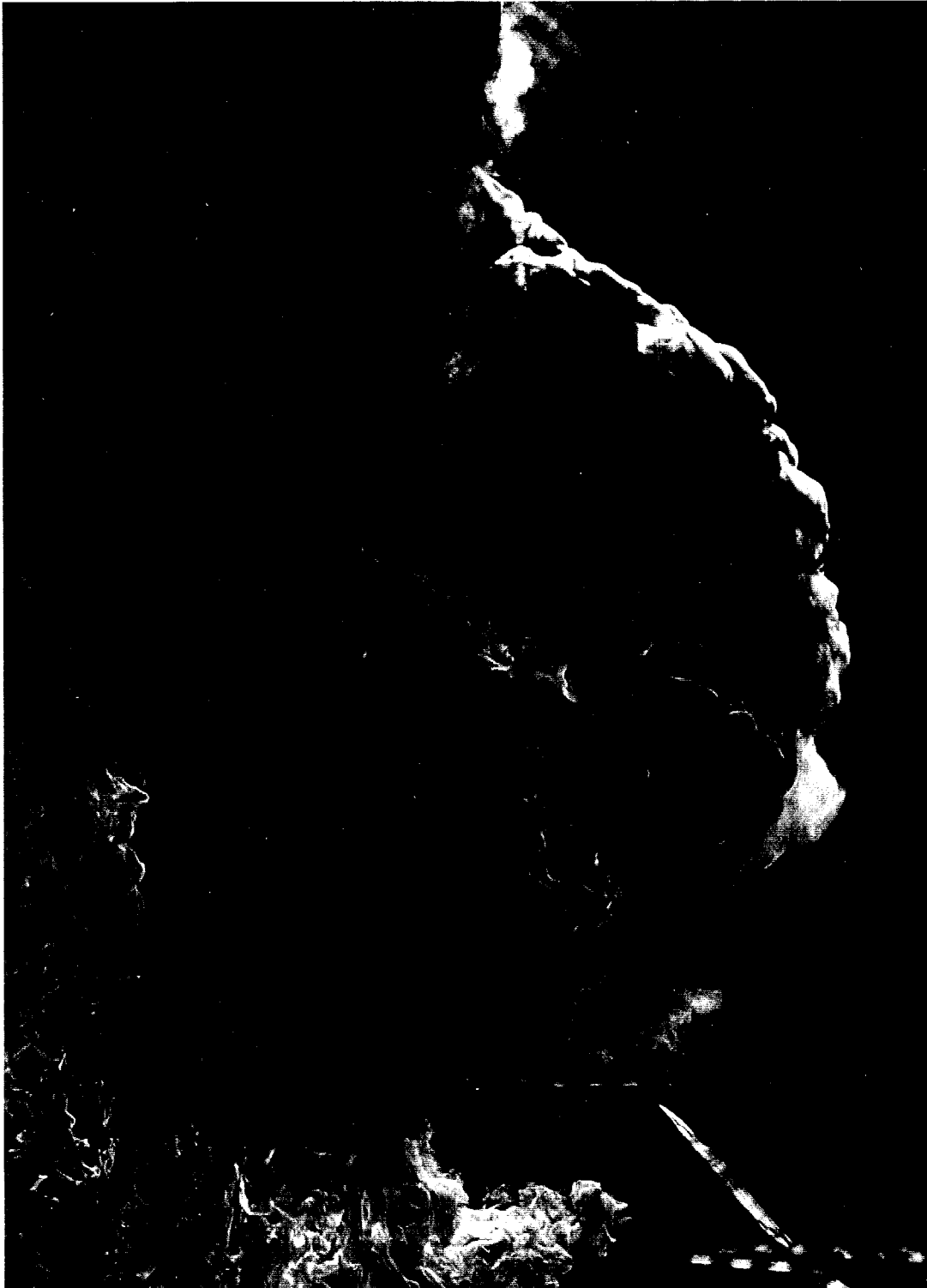
Figure 24. Wrinkled Flame Front on a Rotational Structure about 1/2 m in Diameter. SNL at the Lurance Canyon Facility, 6/16/94; conducted in the 2 m by 6 m rectangular pool.

In Figure 23, tongues of flame are rolling outward on the left edge of the fire. These tongues are similar to those in Figure 7 at the toe of a much larger fire. In both cases, the wrinkled flame surface is being rolled into larger and larger structures as the height above the fire increases. Video shows that this process continues in scale in the large fires until the process shown in Figure 17 results in a smoke layer.

The flame surfaces shown in Figures 23 and 24 are for a relatively small fire. For a larger fire, it is difficult to visualize the flame sheets away from the toe of the fire because they are hidden behind the smoke layer that forms at a relatively small elevation, as shown in Figure 16. However, in a crosswind, the large columnar vortices are relatively clear of smoke. Figure 25 shows the highly wrinkled flame surface on the exposed outward edge of a large columnar vortex on the lee side of the fire.

Figure 25. Flame Sheet on the Exposed Edge of a Large Columnar Vortex. NAWC at China Lake, 1/28/94; conducted in the 18.9 m diameter pool with a crosswind of about 3.0 m/s from approximately 60° off the camera normal.

Postulation of the Source and Effect of Vortical Structures in Fires

This section contains a series of speculative arguments on the source and the effect of vortical structures in fires. The arguments are based on phenomenological reasoning and the observation of fires reviewed in the previous section. The discussion is not intended to be comprehensive but is intended to identify the first order cause and effects of vortical structures in fires.

Source of Vorticity in Fires

We propose that three mechanisms are primarily responsible for the turbulent structures in fires. The first is baroclinic vorticity generation that produces rotational motion at small scale; the second is amalgamation, or pairing, which produces large-scale rotational structures from the myriad of small-scale structures; and the third is the cascading from larger to smaller structures. This view is consistent with that proposed by Lakkis and Ghoniem, 1995, based on two-dimensional vortex dynamics simulations of fires. Baroclinic vorticity generation, amalgamation, and turbulent cascade processes are the subject of current, extensive research beyond the scope of this study. However, each will be discussed in a *qualitative, heuristic sense* as applicable to fires. For convenience, the discussion of the source of vorticity will be divided into two sections: no crosswind and crosswind.

No Crosswind

We will interpret turbulent motions, not as a series of random velocity fluctuations, but as a collection of rotational structures at various length scales and characteristic rotational velocities. It is convenient to think of the characteristic rotational velocities in terms of vorticity and a length scale. Vorticity is defined as being equal to twice the angular rotation rate of a solid body. For example, the z-component of the vorticity vector is defined as,

$$\omega_z = \left(\frac{\partial V}{\partial x} - \frac{\partial U}{\partial y}\right), \tag{1}$$

where V is the flow velocity in the y coordinate direction and U is the flow velocity in the x coordinate direction.

Because we are interested in how rotational motion is created and transported, it is convenient to recast the linear-momentum equations into vorticity transport equations. The various terms can then be directly interpreted as creating, destroying, or transporting rotational motion. Taking the curl of the Navier-Stokes equations gives the vorticity transport equations. The resulting vector equations are,

$$\frac{D\vec{\omega}}{Dt} = (\vec{\omega} \bullet \nabla)\vec{u} - \vec{\omega}(\nabla \bullet \vec{u}) + \frac{\nabla\rho \times \nabla P}{\rho^2} + \nu\nabla^2\vec{\omega} , \tag{2}$$

where $\vec{\omega}$ is the vorticity vector, $\vec{u}$ is the velocity vector, ρ is the density, ν is the viscosity, and P is the pressure.

Figure 26 shows physical interpretations of the various terms. Rotational elements are translated, and their rotation rate is increased or decreased according to the terms on the right side of the vorticity transport equation. The third term on the right side is called the baroclinic vorticity generation term. The acceleration of an object is the applied force divided by the mass. In a fluid, the force is given by the spatial gradient of the pressure, and the density is the mass per unit volume. When the density also has a spatial gradient, and is not in the same direction as the pressure gradient, the fluid is subject to an unequal acceleration. The resulting velocity difference leads to rotational motion, which is called vorticity. The baroclinic generation of vorticity is defined by $(\nabla \rho \times \nabla P)/\rho^2$, where nabla ($\nabla$) gives the gradient and the vector cross ($\times$) shows that the largest effect is produced when the gradients are normal to each other.

In a pool fire scenario, the pressure gradient exists as the hydrostatic pressure field because of gravity in the vertical direction, and the density gradient is the difference between the hot gases and the surrounding ambient conditions in the horizontal direction. Hence, the gradients are misaligned and the conditions exist for baroclinic vorticity generation. Both density and pressure gradients will vary spatially with a fire because of variations in gas temperatures, compositions, and hydrodynamic effects. However, the density gradient will be the largest when the spatial separation between hot and cold gases is the smallest, so the thickness of the density layer will control variations in baroclinic vorticity production. Thus, while vorticity may be produced at all scales, we expect the strongest vorticity to be produced at the smallest scales.

This small-scale vorticity may combine with other regions of vorticity; and if the rotational sense is the same, a larger scale vortex may grow out of the small ones. However, large-scale turbulent motion exhibits the character of an energy cascade down to small-scale random motion. Therefore, in a pool fire we see 1) small-scale vorticity from the density differences misaligned with the gravity vector; 2) growth of large vortices from the small vortices; and 3) the turbulent breakup of large eddies into small eddies.

The last term in Equation 2 becomes very important near solid surfaces such as the ground plane or objects in the fire. The no-slip condition at solid surfaces subject to a tangential flow results in significant vorticity generation. As shown in Figure 27, the gradient in the flow between the free-stream and the object surface produces circulation that has a time-rate-of-change equal to the kinetic energy of the free-stream. Downstream of a bluff object, the vorticity generated along the object surface will be advected into the flow in the form of a wake. Wake flows can result in significant convective stirring downstream of an object.

$$\frac{D\vec{\omega}}{Dt} = (\vec{\omega} \bullet \nabla)\vec{u} - \vec{\omega}(\nabla \bullet \vec{u}) + \frac{\nabla\rho \times \nabla P}{\rho^2} + \nu\nabla^2\vec{\omega}$$

Time Rate of Change of Vorticity

Vortex Stretching

Volumetric Expansion

Baroclinic Vorticity Generation

Diffusion of Vorticity
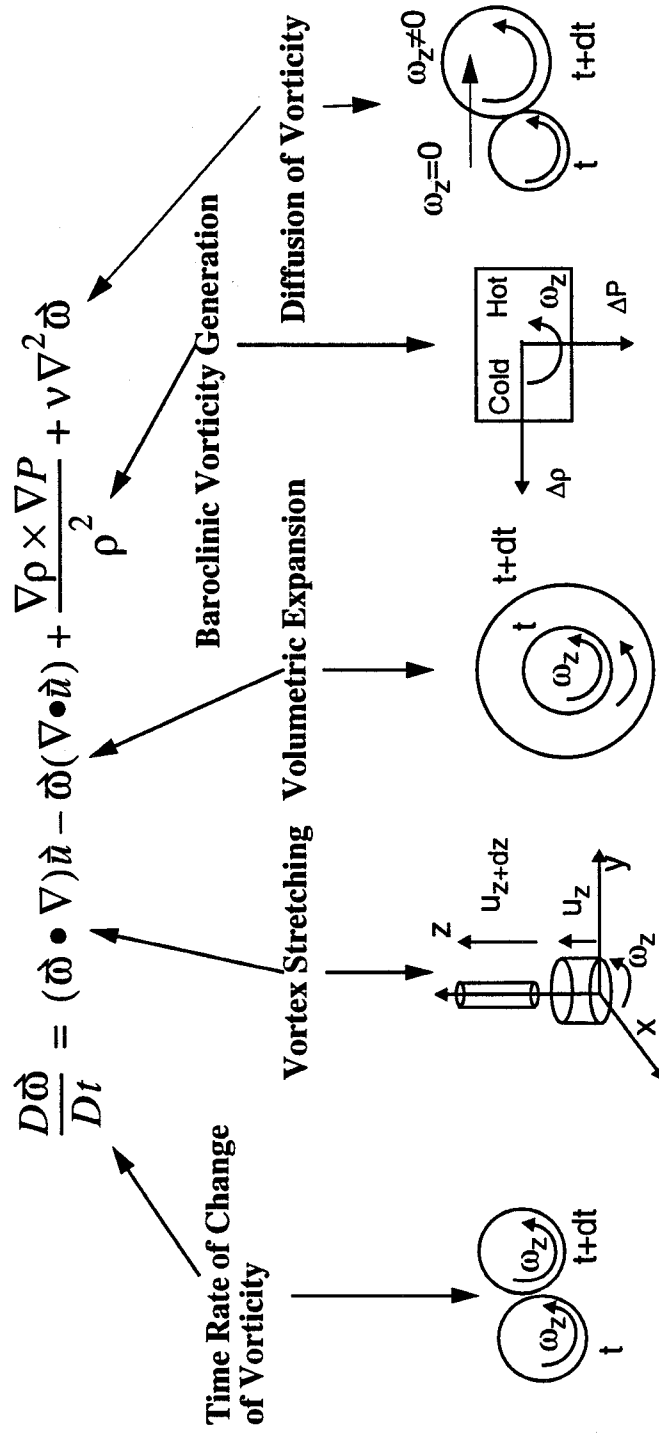
Figure 26. Vorticity is Twice the Solid Body Rotation Rate. It is a vector quantity and examples show the z-component only. The vorticity transport equation is obtained from the curl of the Navier-Stokes equations.

39

In a Crosswind

In the preceding discussion on baroclinic vorticity generation, it was assumed that the pressure gradient was hydrostatic. This assumption will not be strictly true once flow is induced by the fire because the pressure field and the velocity field are coupled. This coupling is particularly relevant in a fire with a crosswind. As shown in Figure 28, a crosswind introduces horizontal pressure gradients. As the crosswind approaches the fire, the upward momentum of the fire results in a transition of the horizontal momentum of the crosswind into vertical and lateral momentum at the leading edge of the fire. Therefore, the pressure is higher on the upstream edge of the fire. As the flow passes around the fire in the horizontal plane, the flow reaccelerates (streamlines converge), and the pressure is at a relative low as the crosswind passes by the side of the fire. The pressure then returns to the mean value associated with the incident wind behind the fire. Hence, pressure gradients are formed on the edge of the fire, with the lowest pressure along the sides and increasing pressure to the front and back. The density gradients are normal to the fire surface. According to Equation 2, this misalignment of density and pressure gradients will result in the baroclinic production of vorticity.
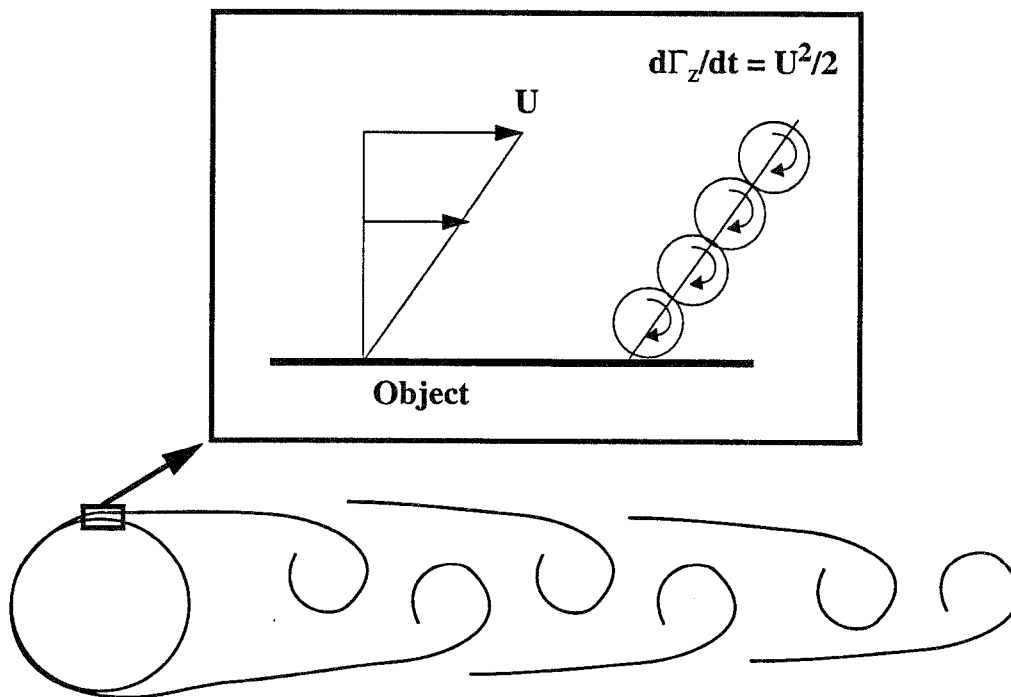
Figure 27. Vorticity is Generated at the Boundary of an Object due to the No-Slip Boundary Condition.
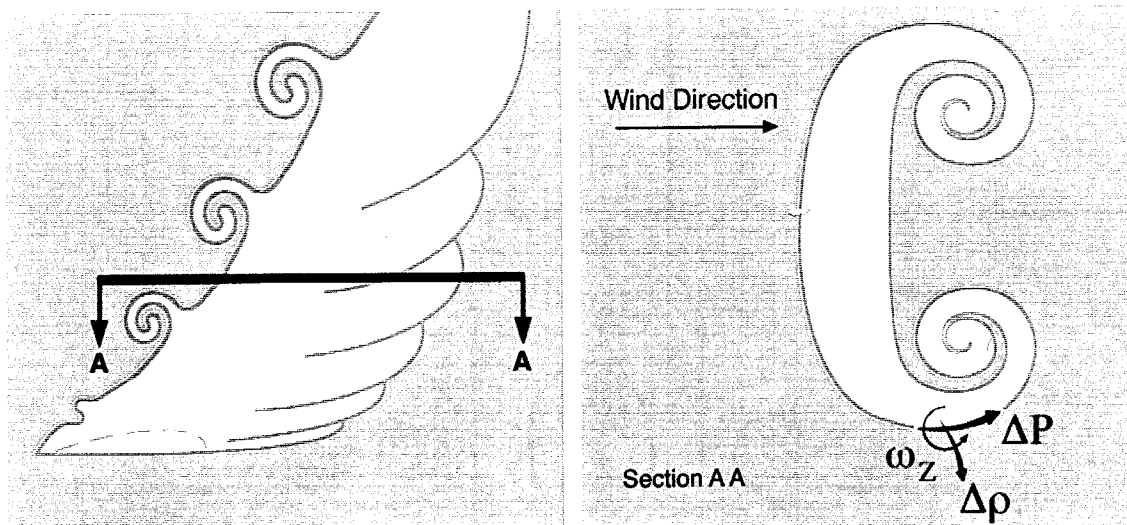
Figure 28. Baroclinic Vorticity Generation in a Crosswind.

Advection of Vorticity in Fires

Once vortical motion is produced, it is advected downstream in the flow. Because the flow is subsonic, the presence of vorticity in one part of the flow affects the velocity at all points in the flow. The exact mechanism by which vortical structures change scale is a subject of much speculation. However, two processes, amalgamation and cascading, are considered important in determining the scale of the rotational structures. These are opposite processes, as amalgamation increases the scale of the turbulent structures while cascading decreases the scale. For convenience, the discussion of the vorticity advection in fires will be divided into three sections: no crosswind, crosswind, and the effect of objects on fire-induced flows.

No Crosswind

Vortex amalgamation is responsible for the formation of large-scale coherent structures found in shear flows (Bernal, 1988). Figure 29 heuristically illustrates this process. Two vortices begin rotation about a common axis, as shown in Figure 29a. The rotation is shown at every 1/4 turn about this common axis. Pairing can also occur at larger scales. Figure 29b shows the same motion as Figure 29a, except that each vortex in the pair is now the same as the one shown in the last frame of Figure 29a. In this manner, large-scale coherent structures can form. The exact mechanism of pairing, and specific growth rates of these structures in even simple shear flows, is the subject of current fluids research.

(a)

(b)
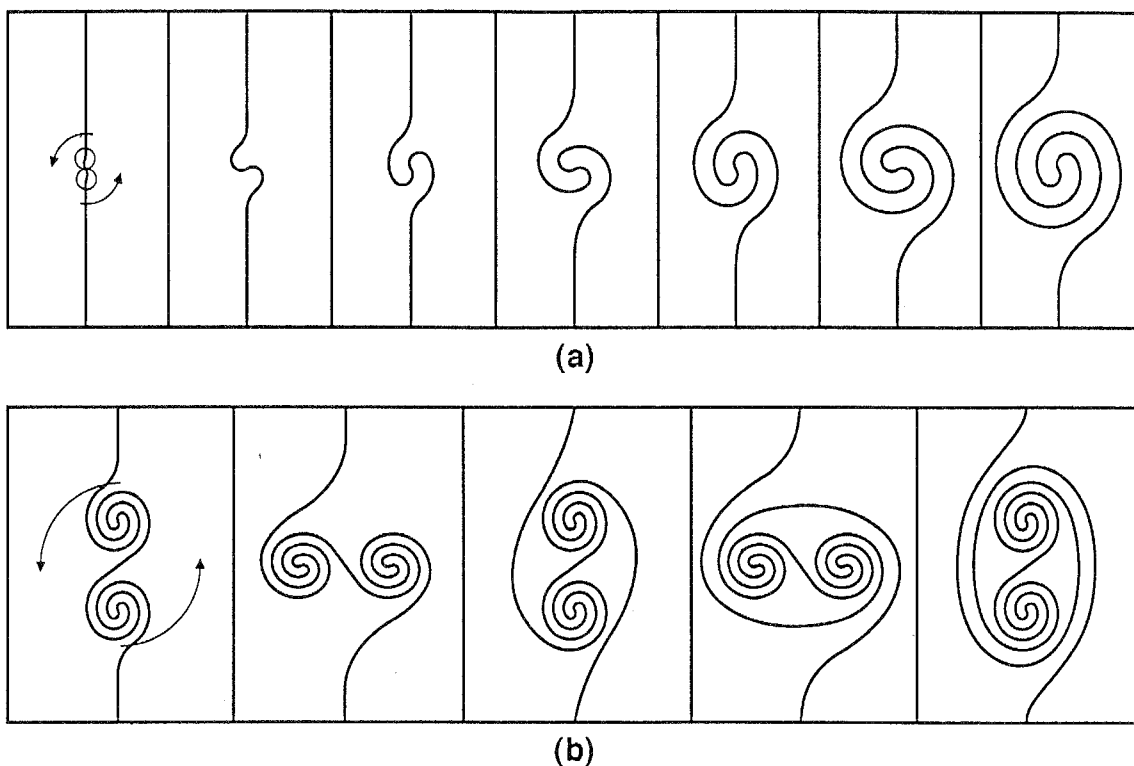
Figure 29. Heuristic Example of Vortex Pairing. (a) Two vortices begin pairing process by a perturbation in the flow. Each frame shows 1/4 rotation to 1.5 rotations. (b) Amalgamation can occur at larger scales. The process is the same as in (a) except that the two vortices have been replaced by two pair of vortices. One rotation is shown.

The importance of this amalgamation process is shown schematically in Figure 30, where the underlying momentum field shown in Figure 29 is combined with a representation of the scalar concentration field. Yellow corresponds to fuel vapor, blue to air, and red to fire. The density difference between the fire and air produces the baroclinic vorticity generation everywhere along the interface. Figure 29 shows two vortices for clarity. However, the baroclinic production of vorticity will produce a sheet of vortices, and pairing will occur along the sheet marking the interface.

The authors speculate that the presence of a vorticity production mechanism in the flow-field is the major difference between the turbulence found in momentum driven flows and that found in fires. In momentum driven flows, the source terms are all at the flow field boundaries with solid objects, as shown in Figure 27. There is no source term for the production of vorticity in the flow-field itself; that is, production is a surface phenomena. The "turbulence" in momentum driven flows can be thought of in terms of *advection* of vorticity. However, in fires (and, as the authors will argue, buoyant flows in general), there is both *volumetric-production and advection* of vorticity, because of the presence of the baroclinic vorticity generation. The existence of a production term has many implications for vorticity in the flowfield. For example, because pressure gradients (appearing in the

momentum equations) and density gradients (appearing in scalar equations) are equally involved in baroclinic vorticity production, the momentum and scalar transport equations are coupled much more tightly than in momentum driven flows. It is the tight coupling and highly nonlinear phenomena that make fires a challenge to model computationally.

The amount of interfacial area burning in the last frames of Figure 30a-30b is substantially higher than in the first frames. This increase in the combustion rate increases the amount of high-temperature products formed. The increase in the amount of high-temperature products increases the buoyancy, which results in higher flow velocities and an increase in the baroclinic vorticity generation along the interface. The process escalates until it is limited on one side by the axisymmetric constraint along the centerline (for no wind) and the structure size is on the order of the diameter of the fire. The production will continue and the structures will continue to grow in scale until the fuel is consumed. At this time, the rate of production of vorticity will decrease, while amalgamation continues to increase the scale of the structures well into the smoke plume.

The process of amalgamation is easier to identify with a crosswind because the wind tends to spread out the structures formed on the upstream side; therefore, the structures do not roll up on themselves as in a fire with no wind. For example, the increase in scale of the rotational structures, as distance from the toe of the fire increases, is shown in Figures 7, 8, and 16.

(a)

Flame
Air   Fuel

(b)
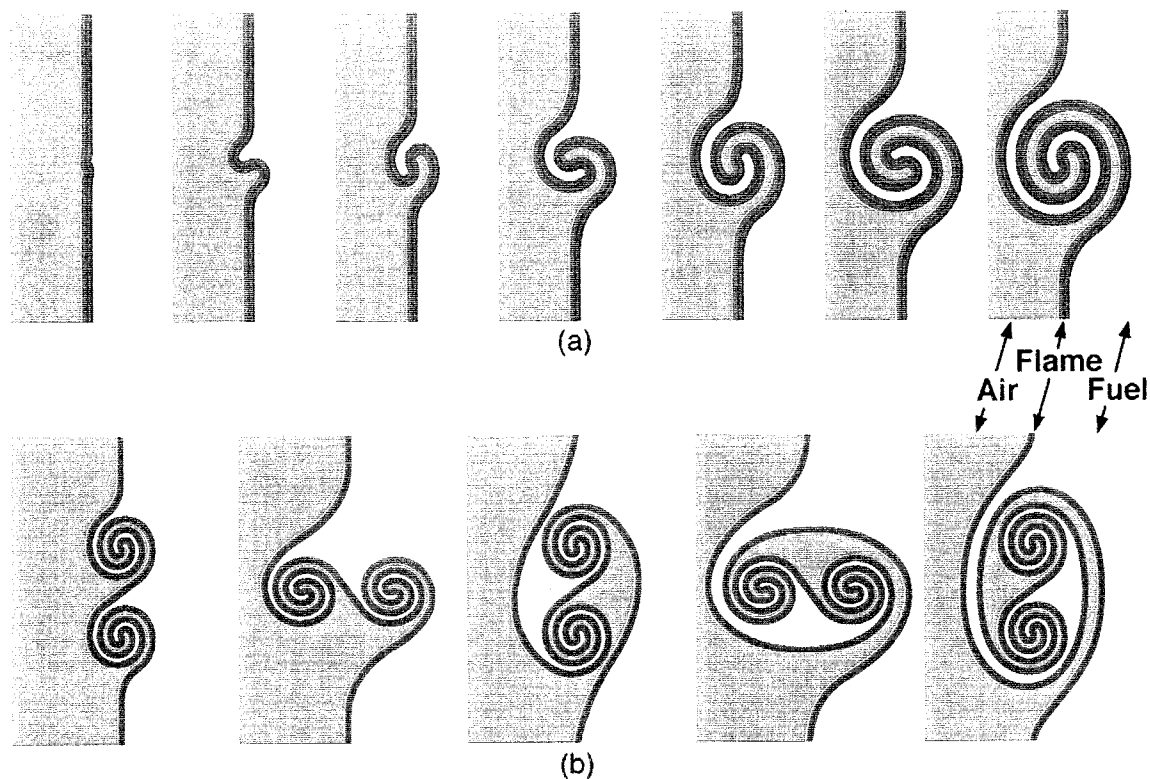
Figure 30. Mixing of the Scalar Concentration Field as a Result of Pairing. Blue is air, yellow is fuel, and red is fire. The underlying flow is described in Figure 5. Note the large increase in interfacial area burning as the pairing occurs.

Heuristically, the growth of rotational structures in a fire without wind is shown in Figure 31. Smaller rotational structures exist at the base of the fire and increase in scale up the sides of the fire. The rotational structures are swept up the sides of the fire by the local flow velocity, as they continue to grow in scale. By this process, air is entrained deeper within the fire. Eventually, air penetrates to the centerline of the fire, which results in the termination of the pure fuel region known as the "vapor dome." By this time the rotational structures have amalgamated and the diameter of the rotating structure is on the order of the fire radius shown in Figure 5. From observation of fires, the elevation above the fire base where the rotational structure reaches from the centerline to the edge of the pool is on the order of one pool diameter.

The formation and growth of the rotational structures is continuous. On a time-averaged basis, the growth rate of the structures determines the "width" of the baroclinically generated vorticity layer. In this manner the "baroclinic layer" is analogous to a "shear layer" formed from a splitter plate, or round jet, except the baroclinic layer has a source of vorticity production (that is, the misalignment of pressure and density gradients) in addition to the advection of vorticity found in both flows.

The authors believe that baroclinic vorticity generation is high along the edge of the fire from the toe upward. However, because the flow velocities near the base of the fire are
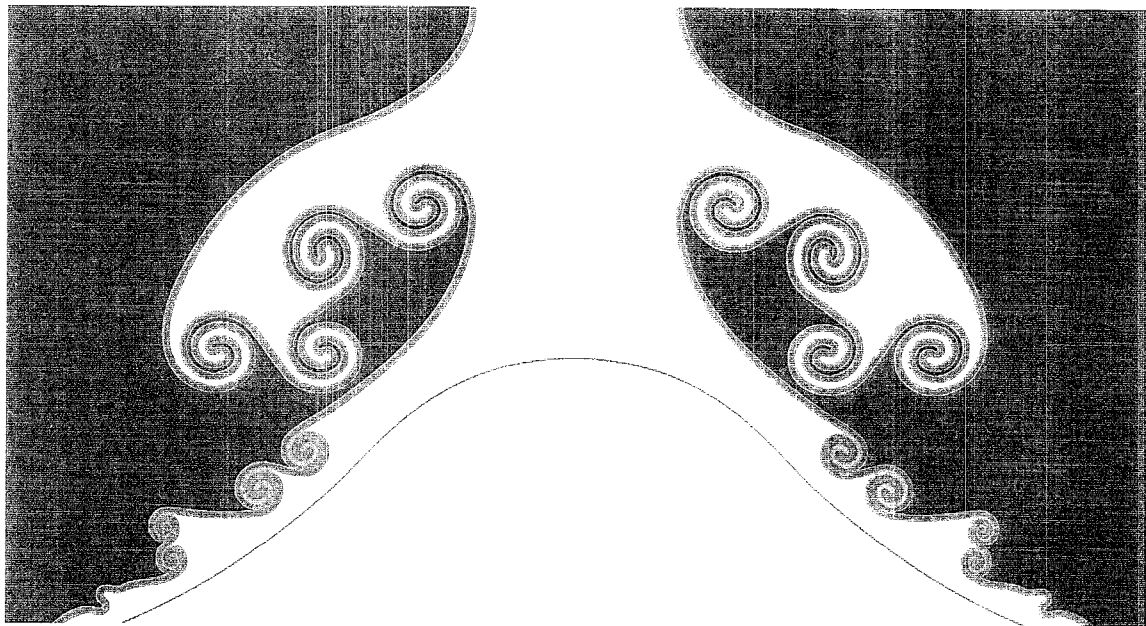
Figure 31. Vortex Amalgamation Results in the Formation of Large-Scale Coherent Structures Responsible for the Puffing Motion in Fires. The scale of the structures grows up the sides of the fire because of amalgamation. Inside this mixing zone is a vapor dome. Without wind, the largest coherent amalgamation is on the order of the diameter of the fire.

low, the amount of boundary layer vorticity production is also low. Under these conditions the total circulation is relatively low. At the toe of the fire, the conditions may be laminar for short distances, until either vorticity is advected into the flow or the baroclinic production is sufficiently high that rotational flow is formed. Because baroclinic production occurs along the surface of the fire, the total circulation increases with elevation. The upward, vertical velocity in the fire also increases with elevation. These two phenomena are related. While buoyancy normally is thought to induce the vertical velocity in fires, the circulation produced by baroclinic vorticity generation at the boundaries between the low and high density regions can be thought of as producing the vertical velocity, as shown in Figure 32.

The authors note that the scale of the structures increases rapidly with elevation from the toe of the fire. Therefore, the rate of amalgamation is fast relative to the flow velocity. Large structures have the circulation to influence the low velocity flow at the base of the fire. This is the source of the "puffing" phenomenon. If there were no coupling between the large-scale structures and the flow at the toe of the fire, there would be no puffing. In a crosswind, production of periodic large structures occurs, but the structures are swept downstream at a higher convective velocity because of the wind momentum and have less effect on the toe of the fire. The large scale structures appear to induce sufficient horizontal momentum at the base of the fire to lay the sides of the fire downward. This decreases baroclinic vorticity generation when the large ring structure has enough circulation and is low enough to influence the toe. However, the large ring structure will be swept axially
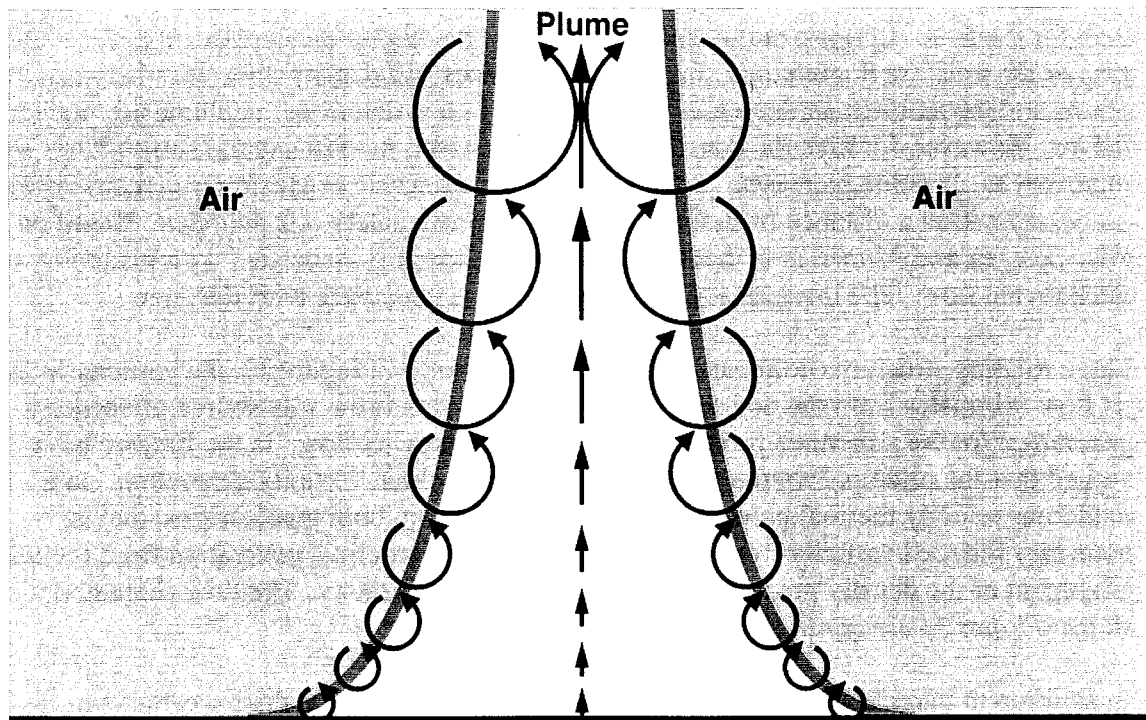
Figure 32. Plume Centerline Velocity Increases in Direct Proportion to the Increase in Circulation (Produced by Baroclinic Vorticity Generation).

along at the local flow velocity. As the large structure moves away from the base of the fire, the radial inflow lessens and baroclinic production of vorticity increases as the side of the fire returns to the vertical. Production and amalgamation of the advected structures both reach the elevation and scale of the previous structure and the process repeats itself. The visual "puffing" effect of the large vortex ring is enhanced by the lack of vorticity production when the vortex ring influences the toe of the fire.

This sequence is shown in Figure 5, which shows the formation of a puff in its early stages at the base of the fire. It can be seen in the first frame on the left side near the base of the fire. Tracking the fire surface upward on the left side, initially the surface of the fire curves inward towards the center of fire. Then it stops abruptly and gradually flows outward. This point is the base of a large amalgamation seen progressing up the fire in the succeeding frames. The last frame shows a new puff in the same early formation state as shown in the first frame. The puffing process repeats itself continuously. The puffing frequency, that is, the frequency of passage of these structures, has been shown to correlate to the inverse of the square root of the fire diameter (Hamins, Yang, and Kashiwagi, 1992; Cetegen and Ahmed, 1993).

While our arguments regarding the influence of vortical structures in the flow have been made for fires, they are also applicable to buoyant flows in general. For example, puffing is not limited to fires. Cetegen and Ahmed, 1993, have shown that puffing occurs in isothermal helium plumes, finding that the puffing frequency for the helium plumes is approximately the same as for fires with the same source diameter and flow rate. The puffing intensity, as measured by the pressure fluctuations, was less for the helium plumes than for the fires. Cetegen and Ahmed showed that the higher the density difference, the greater the pressure fluctuations. In the helium plumes, the density difference between the plume and the ambient air decreases with increasing elevation from the plume mixing with the air. However, for fires the density difference between the fire and the surrounding air increases as elevation increases. This is caused by volumetric expansion from combustion processes within a distance from the fire base of approximately one diameter. Based on this, Cetegen and Ahmed note that the puffing phenomena is associated with instability of the buoyant flow. The interpretation presented here is consistent with this view.

Large rotating structures dominate many flows. As shown in Figure 33, the vorticity in the jet flow originates from the nozzle boundary layer, as this is the sole source of vorticity generation for the structures produced in constant-density jet flow. In the fire, we have argued that the principal source of the vorticity is baroclinic vorticity generation. In a moderate velocity thermal plume, the vorticity arises from both mechanisms, that is, boundary induced vorticity from the exhaust stack and baroclinic generation from the misalignment of the density gradient from the hot plume and gravity. The flow characteristics shown Figure 33 are *qualitatively* compared in Table 1.

In addition to baroclinic vorticity generation and amalgamation, a third mechanism, cascading from larger to smaller scales, may be important in fires. The classical view of turbulence is that energy is transferred from large-scale eddies to smaller scale eddies through velocity/vorticity interactions (Tennekes and Lumley, 1972). In shear flows, vor-

46

Jet   Thermal Plume   Pool Fire
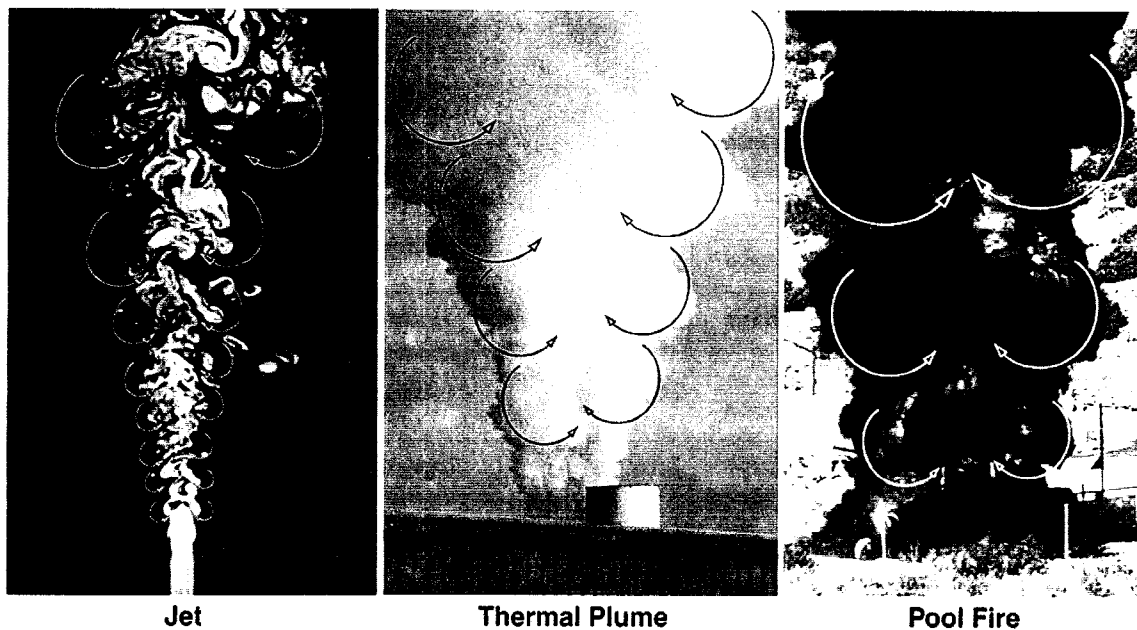
Decreasing source velocity (no-slip production of vorticity) ⟶

Increasing density difference (baroclinic production of vorticity) ⟶

Figure 33.   Large-Scale Vortical Structures Found in Fires are Common to a Number of
Flows.

tex interaction with a mean flow gradient can intensify vorticity at length scales smaller
than the characteristic gradient length scale, thereby transferring kinetic energy to smaller
scales. The extent to which this mechanism occurs in fires is not clear from the qualitative
observations. The argument that small scales exist in fires, which can clearly be seen in
photographs, is not sufficient to suggest that a cascade caused their presence because pro-
duction may also occur from baroclinic vorticity generation.

While it is argued that turbulent production occurs at the largest scales, observation of
structures pairing in fires indicates that the largest structures are amalgamations of smaller
ones, rather than spontaneously produced from large-length-scale density gradients that
may be associated with the broadening mixing layer. The classical view of turbulence is
usually developed in constant density flows in which vorticity is produced at a wall and
advected into the fluid. One can postulate that as the ratio of advected vorticity to produc-
tion of vorticity increases the flow will become more and more like a standard shear flow
(see the plume data of Dai and Faeth, 1995). Seventy diameters from the plume source,
the turbulent statistics for a buoyant plume are not substantially different from that
expected for a jet source.

In a fire, baroclinic vorticity production will occur at the interfaces with cold air and will
then be advected upward with the flow. The consequence of the advection of vorticity is

47

Table 1. Qualitative Relationships Between Jets, Plumes, and Fires

		Flow Type		
		Jet	**Plume**	**Fire**
Mean Axial Centerline Velocity	Just Above the Base	High	Moderate to Low	Low
	Change with Increasing Elevation	Decreasing	Decreasing	Increasing (up to 1 dia.)
Vorticity	Just Above the Base	High	Moderate	Low
	Change with Increasing Elevation	Zero	Increasing	Increasing
Vorticity Production	Just Above the Base	Zero	Moderate	Moderate
	Change with Increasing Elevation	Zero	Decreasing	Increasing (up to 1 dia.)
Scale of the Rotational Structures	Just Above the Base	Small	Small	Small
	Change with Increasing Elevation	Increasing	Increasing	Increasing
Approximate Axial Distance from Base to Elevation at which Structures Penetrate to the Centerline		3-5 diameters	1 diameter	1 diameter

that only a fraction of the total vorticity present at any elevation is a consequence of local production from baroclinic vorticity generation. The rest is advected vorticity created lower in the fire. The vertical centerline fire velocity increases as elevation increases, as caused by the summation of the local vorticity production and its advection. As the centerline velocity increases, the mean velocity gradient between the centerline and surrounding flow increases (a consequence of the vorticity present). As the ratio of production to advection goes down, the flow will have structures that better approximate those found in classical nonbuoyant flows. Under these conditions, vorticity/mean strain interactions may result in energy cascading to smaller and smaller length scales. In a fire, the elevation at which the ratio of production to advection is sufficiently small enough to make the classical -5/3 power law cascade applicable is unclear.

In a Crosswind

Just as in cases with no crosswind, fires and jets have qualitatively similar structures in the presence of a crosswind. This feature is expected because the primary difference between jets and fires is the source of vorticity production. The advection of vortical structures is the same for both. Interesting descriptions of vortical structure dynamics in jets in crosswinds can be found in Fric and Roshko, 1994, and Morton and Ibbetson, 1996. Figure 34, taken from Fric and Roshko, 1994, shows the types of vortical structures found in jets.
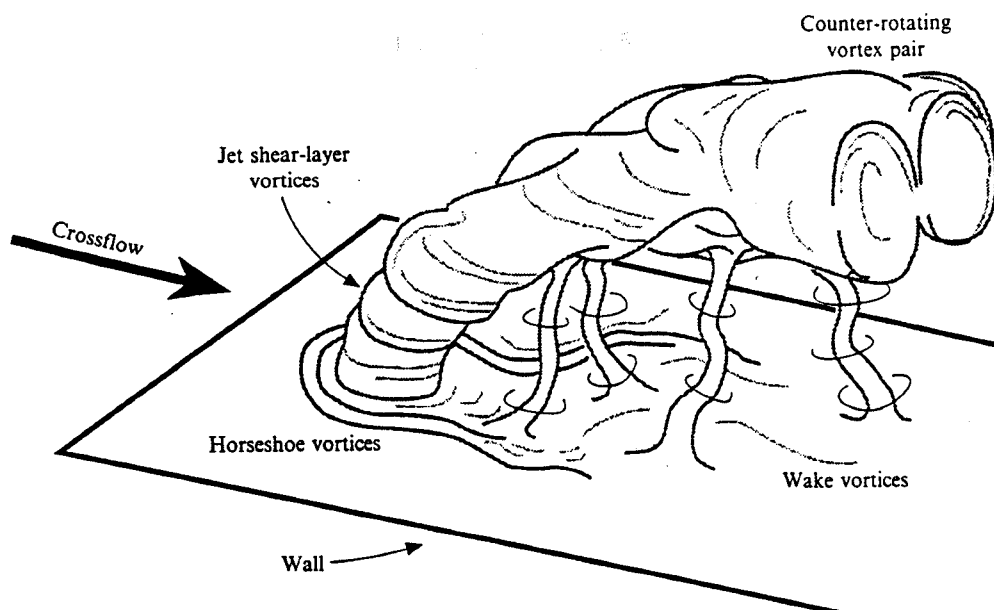
Figure 34. Vortical Structures in Jets in Crossflow. Four types of structures are shown: jet shear layer vortices, counter-rotating vortex pairs, horseshoe vortices on the wall, and wake vortices. From Fric and Roshko, 1994.

Four types of structures are shown: jet shear layer vortices, counter-rotating vortex pairs, horseshoe vortices on the wall, and wake vortices. The similarities and differences between jets and fires are seen by comparing each of the four structure types for the two flows.

The shear layer vortices in jets do not exist in fires. As stated previously, the azimuthal, ringlike vortical structures found in fires are present because of baroclinic vorticity generation and amalgamation. As stated with respect to Figure 33, amalgamation occurs in both jets and fires. Therefore, the source of the vorticity is different, but the structures themselves are similar. This similarity means that the crosswind does not suppress the formation of ringlike structures on the upwind side of the fire as shown in Figures 7, 8, and 16. The wind may quantitatively affect the rate of baroclinic vorticity production because the air entrained into the fire is not quiescent, but has momentum associated with it because of the wind. The entrainment of this air with its associated horizontal momentum causes the mean tilt of the plume downwind. The tilt angle may affect the production of baroclinic vorticity. Further, the entrainment of air with a mean momentum results in higher advection of the vortices away from the toe of the fire. From visual observation, "puffing" does not occur because the vortices are advected downstream before they can grow large enough to make their induced velocity field affect the toe of the fire. However, the production and amalgamation is such that the passage of the vortical structures at a fixed point on the leading edge appears to be quite regular, the same as the structures in a jet in crossflow.

Morton and Ibbetson, 1996, argue for a mechanism of boundary layer/shear layer interaction to produce the counter-rotating vortical structures found on the leeward side of jets in cross-flow. This same type of interaction may be present in fires, with the caveat that the vorticity in the fire plume is produced by baroclinic vorticity production, rather than a no-slip condition at the exit nozzle, as in a jet.

In addition to the Morton and Ibbetson mechanism on the leeward side of fires, the pressure and density gradients are misaligned, producing baroclinic vorticity with the correct sign as the counter-rotating pair, as shown in Figure 28. The pattern found in jets is therefore reinforced in fires. It is unclear what mechanism is dominant because both produce the same rotational structures. As stated for Figures 11 and 12, the rotational structures are long-lived but are not completely stable. As a result, sometimes a single structure exists. The source of this instability is not clear; the counter-pair may convect each other. It appears that the base of the columnar vortices is being slowly swept downstream as they strengthen. Once they reach a given distance downstream from the pool, they appear to quench. One may infer that as the vortex moves away from the leeward side of the fire, fuel vapor can no longer be entrained. This is reinforced by observing that very little smoke remains within the vortex when it stops burning, suggesting that it is being fuel starved at the point it quenches. At quench, flame and smoke structures stop marking the columnar vortex location. It is unclear what happens to the vorticity in the vortex because it can no longer be visualized once combustion ceases and smoke is no longer entrained. This happens to each vortex, and when one "dies," the flow reorients and a new vortex is formed in the fire.

Horseshoe vortices are found upstream of jets, but may be only weakly present in fires. According to Morton and Ibbetson, 1996, horseshoe vortices form because of the vorticity in the boundary layer on the ground. The adverse pressure gradient formed on the ground surface upstream of the stagnation point produces vorticity of opposite sign. The amount is sufficient to cancel the boundary layer vorticity except for the amount entrained. The jet in crossflow has considerable momentum when it leaves the mouth of the jet. As a result, the jet in crossflow strongly deflects the horizontal crossflow upward and around the jet. This deflection results in the adverse pressure gradient. The stronger the pressure gradient, the less flow is entrained in the jet in the boundary layer. If the jet were a solid cylinder, there would be no penetration at all.

A fire differs substantially from a jet because its vertical (or buoyant) momentum is very low at the base of the fire. As noted earlier, the entrainment of air, with relatively high horizontal momentum, into the plume, with relatively low vertical momentum, results in a net deflection of the plume/air mixture toward the horizontal. Baroclinic vorticity generation results in increased vertical momentum as the elevation in the fire increases. Hence, the strongest deflection is at the toe, as shown in Figure 10. The deflection from the vertical will decrease with elevation (for a wind profile constant with elevation) until the end of the continuous flame zone, when the buoyancy begins to decrease from entrainment.

In addition to deflecting the plume, the entrainment of air with significant horizontal momentum near the fire edges at the fire base, results in the burning fuel/air eddies being

50

convected downstream of the pool, very low to the ground. Evidence for combustion near ground level well downstream of the pool can be found in soot footprints, as shown in Figure 15, and from video records of the combusting columnar structures. The phenomena has been termed "flame drag" (Moorhouse, 1982; Welker and Sliepcevich, 1967). It is not surprising that combustion near the ground can occur a diameter or more downstream from the fuel source in a high crosswind because the vertical momentum in the fuel plume at the base of the fire is very low. Rotational structures that have engulfed flame surfaces and volumes of both fuel (with low vertical momentum) and air (with high horizontal momentum) will have little tendency to loft relative to their downstream displacement until combustion results in sufficient buoyancy for the eddies. It can be surmised that the burn-out of these eddies marks the visible extent of the fire downstream of the fuel source near ground level.

Wake vortices are found in fires as well as jets. According to Morton and Ibbetson, 1996, wake vortices form in jets by the same mechanism that produces the counter-rotating structures on the leeward side. When boundary layer vorticity is entrained into the jet, its sign is opposite that of the shear layer vorticity, and this results in the vortex tipping to the vertical on the leeward side. If the boundary layer vortex stays coherent and attached to the columnar vortex, then one end of the boundary layer vortex is pulled up the leeward side of the fire with the columnar vortex, while the other end remains fixed in the boundary layer. This explanation is consistent with observations of wake vortices from fires, as shown in Figures 18 and 19. These wake vortices are marked by dust in the vortex, which indicates that the vorticity is produced in the ground boundary layer rather than in smoke, as would be expected if the vorticity was produced by baroclinic vorticity in the fire.

Effect of Objects

As shown in Figure 27, objects in a flow-field generate vorticity in their boundary layers. The amalgamation process also occurs for vorticity shed from objects in cross-flow. Large-scale rotational structures caused by the alternate shedding of vortices from the object, shown in Figure 35a, are common features of wake flows. If the object and its resulting wake are completely immersed in the vapor dome, or completely removed from the fire, then the rotational motion of the flow may do little to affect the fire.

However, as shown heuristically in Figure 35b, if the object is partially engulfed, or if its wake carries significant vorticity into the fire, then the rotational structures enhance the mixing between fuel and air. This increases the amount of interfacial area and therefore the amount of combustion. The result will be a "hot spot" downstream of the object in the wake region in cross-flow. The actual combustion behind an object may not occur as shown in Figure 35b, as the volumetric expansion from combustion may stabilize or otherwise alter the shedding process. Stabilization of a combustion zone without vortex shedding is quite common at very high speeds associated with gas turbine combustors, in which significant premixing of the fuel and air occurs upstream of the object (see Hertzberg et al., 1991).

51
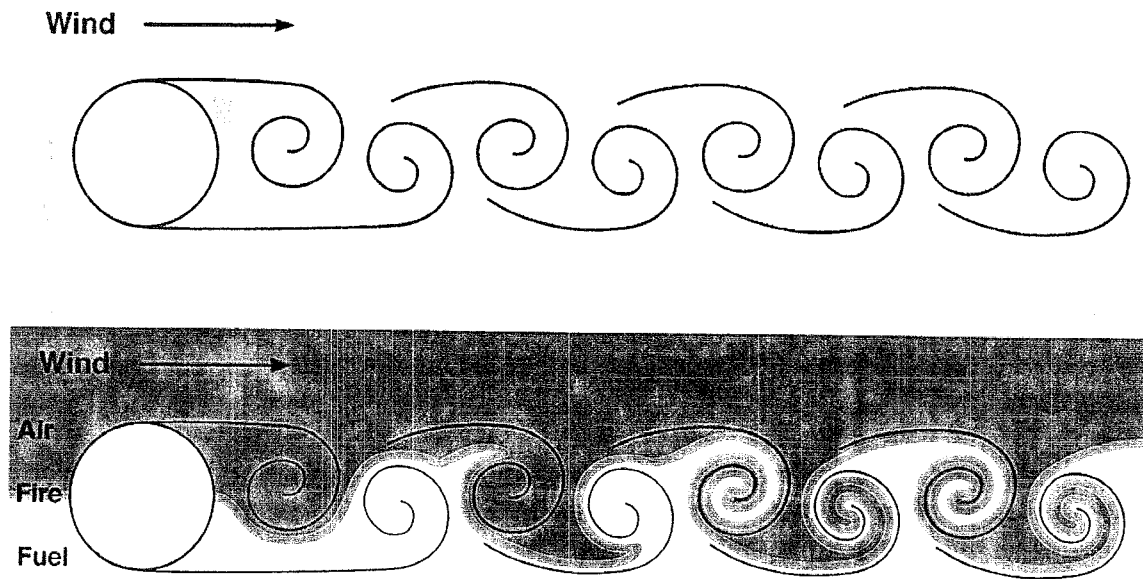
Figure 35. Wake Flow Behind an Object in Crossflow. (a) Large-scale coherent structures in the momentum field. (b) Superimposed scalar species field if the object is partially engulfed in a fire. Blue is air, yellow is fuel, and red is fire.

It is not necessary to have a crosswind to have vorticity generation and advection into the wake of an object. The fire generates a radial inflow in the absence of a crosswind. Figure 36 shows the wake vortices resulting from the flow-field as induced by the fire itself. Inflow about the plate (shown in Figure 36a), results in standing vortices on the fire side of the plate. These vortices entrain fuel vapor at their base and become columnar flames. Figure 36a is intended to be representative of the test shown in Figure 5. But in Figure 5, it is difficult to see the standing flame that occurred on the right side of the fire near the
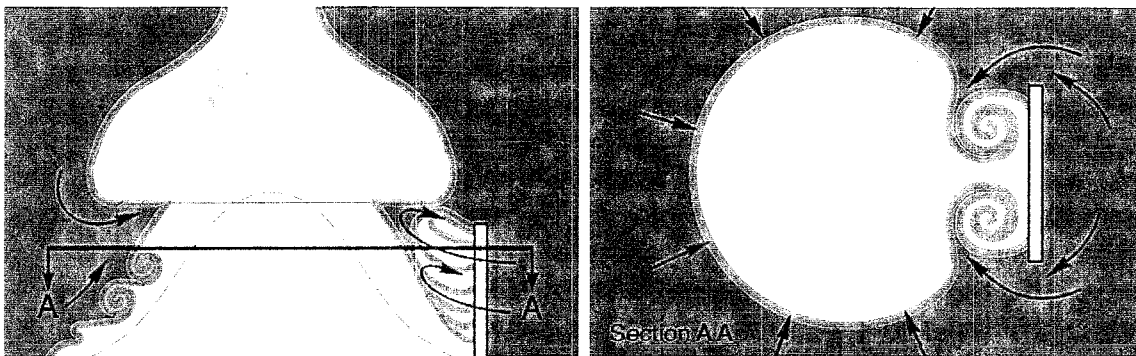
Figure 36. Example of Object Inducing Wake Flow in a Fire without a Crosswind.

base. The heat flux from the flames in columnar vortices adjacent to an object wake may be very significant.

Entrainment, Stirring, and Mixing

Baroclinic vorticity production, amalgamation, and cascading have been presented as the dominant physical mechanisms for the production and transport of rotational motion in a fire. Each of these processes has an impact on the production and transport of scalar fields in a fire. On the other hand, the production and transport of scalars has an impact on the production of rotational motion. As noted for Equation 2 and Figure 30, density variations within the scalar field are responsible for the generation of rotational motion through baroclinic vorticity production. Thus, there is a tight coupling between the scalar field and the momentum field that is not found in momentum driven flows.

A distinction is made in the processes of entrainment, stirring, and mixing, primarily on the length scale of the process involved. The largest scale rotational structures are primarily responsible for the gross entrainment of air into the fire. As Figure 31 shows, the scale of the largest structures continuously increases as distance increases from the base of the fire because of the amalgamation process. Hence, the depth to which air can penetrate into the fire increases with increasing elevation until air is drawn into the centerline of the fire. Because combustion cannot occur in the absence of air, the growth rate of the large-scale structures influences the size of the region in which pure fuel exists, that is, the vapor dome.

The stirring of the fuel and air is a consequence of advective scalar transport over the range of turbulent length scales between the largest scale responsible for entrainment, and the smallest scales where diffusive transport begins to dominate. Fuel and air transport by the range of turbulent eddies in a fire results in a substantial increase in surface area between fuel and air. This increase in surface area increases the combustion rate, hence the fuel is consumed faster. For example, laminar flame heights can be up to an order of magnitude longer than turbulent flame heights (Hottel, 1959).

In classical turbulence descriptions, the smallest structures in a flow are those with length scales on the order of diffusive length scales. Turbulent kinetic energy is lost in these structures by viscous diffusion. Mixing to a molecular level is a diffusive process that occurs on similar length scales for gases. Since flame zones occur only when reactants are mixed to a molecular level, these also occur at the smallest length scales of turbulence. The interactions at these length scales are the subject of decades of laboratory scale research in turbulent combustion.

Since combustion is occurring at the smallest length scales and air is being entrained at the largest length scales, the entire turbulent-length-scale range plays a role in the amount of interfacial area available for combustion. Further, more is involved in stirring and mixing than just the rotation of the underlying momentum field. As discussed with respect to Figure 35, the key element to the formation of high temperature regions is not just mixing, but a mixing of fuel and air such that combustion is increased. If mixing occurs in a region

53

that is air or fuel starved, the increase in the mixing rate will not necessarily lead to a large increase in combustion rate. An example of this behavior is the rollup and burnout of a fuel-rich eddy that, as we will argue in a subsequent section, results in a lot of smoke but not necessarily heat. On the other hand, given the optimal concentrations for the turbulent structure, significant increases in temperatures can result. An example of this behavior is the factor of two elevation in heat flux behind the objects in Figures 5 and 22. The question of what concentrations for the scale and intensity of rotational structures will result in significant combustion rates requires quantitative analysis beyond the current study.

Vapor Dome

The convergence of the baroclinic mixing layer along the side of the fire determines the extent of the fuel-vapor dome. In large hydrocarbon pool fires, the fuel evaporation rate is sufficiently high that a region of pure fuel vapor exists under the mixing layer. In pool fires less than a meter in diameter, the flame surface (thin mixing layer) converges to a central column very quickly, effectively limiting the size of the vapor dome. The presence of a vapor dome has several interesting thermal consequences. For example, the buoyancy of the fire is caused by the density difference between the fire plume and the surrounding air. Equivalently, the baroclinic vorticity production also depends on this density difference.

The presence of a single flame sheet cannot account for the net circulation required to produce the upward flow near the base of the fire. The reason for this is that the baroclinic vorticity production on each side of the flame zone cancels if the density of the fuel and air are equal, as shown in Figure 37a. There is a net upward velocity within the flame zone in Figure 37a, but no net circulation to cause vertical velocity on the plume (fuel) side of the flame zone. On the other hand, if the density of the fuel is considerably less than that of the air, then there is a net circulation across the flame zone and an induced upward velocity on the plume (fuel) side, as shown in Figure 37b. From a linear momentum perspective, the concept is clear; if the fuel vapor is not buoyant relative to the air as in Figure 37a, then it will not rise because of buoyancy, regardless of whether a flame zone is on its boundary or not. On the other hand, if the fuel vapor is buoyant as in Figure 37b, then the fuel vapor will rise regardless of the presence of the flame zone.

For the fire plume to be buoyant at its base, the fuel vapor must be less dense than the surrounding air. The attainability of this condition for vapors from liquid hydrocarbon fuels is not at all obvious. The molecular weight of aviation fuels like JP-4 or JP-8 can be five to six times that of air. At ambient temperature, the vapor is not buoyant but negatively buoyant, that is, it will spread along the ground like gasoline vapor. To make the plume neutrally buoyant, the absolute temperature would have to be five to six times that of air (~300 K), or between 1500 K and 1800 K. Thermocouple measurements of average temperatures in the vapor dome region of large fires do not support the existence of a temperature this high in the vapor dome region of the fire. The thermocouple temperature data are more consistent with 1000 K levels (Gritzo et al., 1995). The temperature directly above the pool will be close to the mid-fraction boiling temperature of the fuel, typically
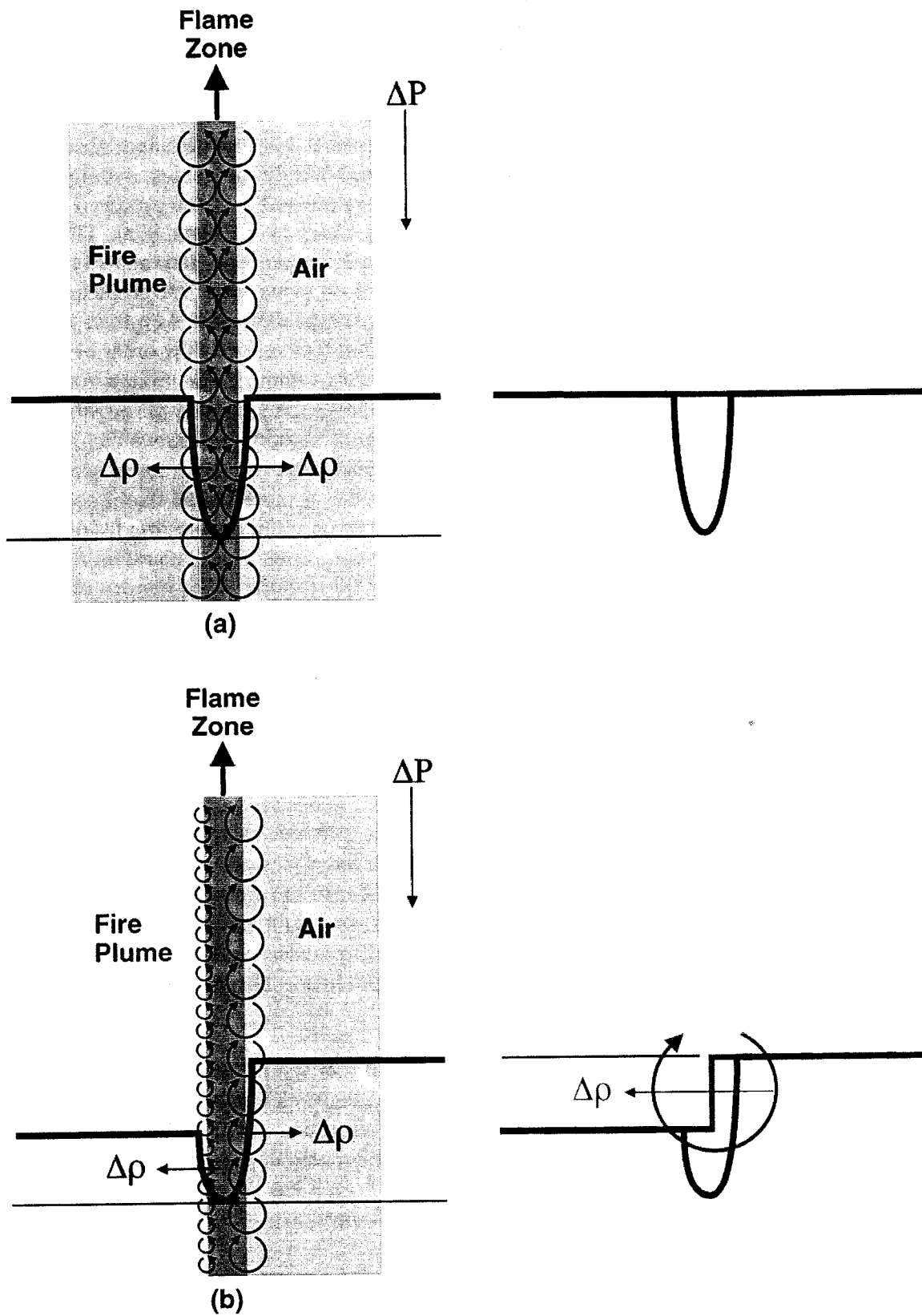
Figure 37. Flame Zones Do Not Necessarily Generate Net Circulation across Them.
(a) Fuel and air have equal densities, so no net circulation occurs across them.
(b) Fuel is less dense than the air, so net circulation occurs.

on the order of 500 K for jet fuels, but the temperature rises to the 1000 K level within the vapor dome region.

One explanation consistent with the experimental evidence is that the fuel vapor absorbs thermal radiation and thermally cracks into low molecular-weight molecules, thereby decreasing its density at constant mass. Constant temperature and pressure pyrolysis (fuel only, no air) calculations at 1000 K using the iC_8H_{18} mechanism of Curran et al., 1995, show that within approximately one second, the fuel vapor decomposes into approximately 2% hydrogen, 40% methane, 12% acetylene, 15% ethylene, and 13% propane with the balance being higher hydrocarbon fragments. The average molecular weight of this mixture is much closer to air, so a density ratio of air to hot fuel vapor on the order of three is possible. This density ratio will increase outside the vapor dome in the mixing zone where hot combustion products will further raise the average temperatures to roughly the 1300 K level. Based on fuel vaporization rates, the vertical velocity just above the fuel pool is on the order of centimeters per second, so residence times on the order of seconds are possible for vapor dome heights on the order of a meter or more. In all likelihood, at the 1000 K level soot will quickly form out of some of the unsaturated and ring fragments and the soot particle/gas mixture may become strongly absorbing, thus accounting for a temperature rise from 500 K at the fuel surface to the 1000 K levels in the interior of the vapor dome.

Effect of Vortical Structures on Combustion

To have combustion with normal hydrocarbon fuels under typical temperatures and pressures, three elements must be present at a molecular level: air, fuel, and an ignition source. As we presented previously, the largest turbulent scales are responsible for air entrainment and the turbulence at length scales from the diffusive to the large scales are responsible for increasing the surface area of the fuel/air interfaces. Combustion occurs at all fuel/air interfaces except under conditions that would result in quenching. The flame zone is not infinitely thin, however, because the air must mix with the fuel on a molecular level for combustion to occur. Once molecularly mixed, reactions can occur within a finite-thickness flame sheet that release heat and form products. These length scales are shown heuristically in Figure 38.

Therefore, there are three processes that affect the rate of fuel vapor consumption in a fire: 1) convective stirring that produces large interfacial area between fuel and air, 2) diffusion of species across the interface resulting in molecular mixing, and 3) chemical kinetic rates of heat release. Each of these processes can control the process depending on the flow conditions and chemistry. However, for large buoyant fires, it has long been argued that the fuel vapor combustion rate is limited by the rate of convective stirring.

Characteristic time scales can be associated with each of the processes involved in large fires. Convective stirring occurs over time scales normally associated with an eddy roll-over time, that is, the eddy diameter divided by the mean velocity. Using a 1 meter diameter eddy as a typical intermediate scale eddy in a large fire, the rollover time scale is on the order of 0.1 - 1 s for velocities of 1 to 10 meters per second, which are typical in fires.

Large Scale Structures	Intermediate Scale Structures	Small Scale Structures
Control Air Entrainment	Enhance the Flame Area	Strain the Diffusive Combustion Zone
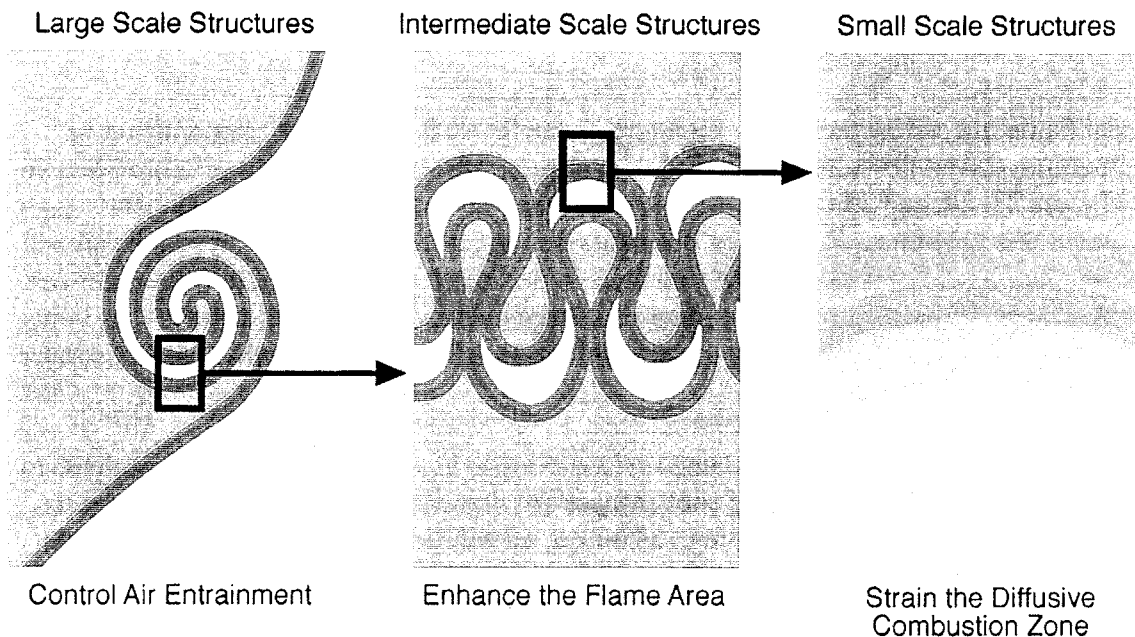
Figure 38. Momentum Length Scales and Their Effect on the Combustion Process.

Of course, the smaller the eddy at a fixed velocity, the shorter the eddy rollover time. Hence the classical turbulence result: small eddies are typically associated with higher strain rates even though they have lower values of kinetic energy. Thus, smaller eddies are capable of increasing the interface area between the fuel and air substantially, thereby decreasing the characteristic times. As the turbulence intensity is increased, the dissipation length scale decreases, and the characteristic times decrease accordingly. Therefore, at high enough turbulence levels, neither the diffusive nor kinetic time scales are fast enough and quenching occurs.

Diffusion times are typically estimated by the square of the flame thickness divided by the diffusion coefficient. Non-premixed flame zones are typically on the order of a millimeter in thickness and diffusion coefficients are on the order of 0.1 cm^2/s, yielding a time scale on the order of 0.1 s. Intense strains can reduce the thickness of a flame zone by an order of a magnitude, thus decreasing the characteristic diffusive time scales to milliseconds before flame failure (see critical velocity gradients at the boundary of a nozzle in Lewis and von Elbe, 1987). Thus while laminar unstrained flames have relatively long, diffusion-controlled time scales, turbulence induces strain that decreases the diffusive length scales, and thereby decreases the diffusive time scales.

Chemical kinetic time scales can be very fast compared to the convective and diffusive time scales. Laminar flames, both diffusive and premixed, are typically controlled by diffusion time scales. Turbulence, by inducing strain and rapid area increase, decreases the characteristic time scales and therefore increases the combustion rate. In the idealization that mixing time scales are infinitely fast, combustion can be modeled as a perfectly stirred

reactor. The blowout of this reactor is then limited by chemical kinetic rates alone. Residence times corresponding to flame blowout in perfectly stirred reactors are typically on the order of tenths of milliseconds.

Local flame quenching caused by high turbulence levels is a common phenomenon in momentum driven flows, such as in lifted jet flames. However, the flame structures shown in Figures 23, 24, and 25 suggest that the turbulence levels in fires are not sufficiently high to create this phenomenon. Rather, observations suggest that the flames appear as almost continuous, wrinkled sheets. With velocities in the meter per second to tens of meter per second range at the center of a fire plume for large diameter fires, local velocity gradients sufficient to result in flame quenching are difficult to achieve and are unlikely to exist over much of the flame surface.

On the other hand, smoke on the flame surface exterior in a fire suggests that a mechanism exists whereby fuel in the form of soot escapes the flame surface. This feature is consistent with significant flame quenching. However, as will be discussed in the next section, we postulate that the burnout of air in amalgamating eddies results in this effect, not turbulence-induced quenching. The smoke produced low in a fire is often re-entrained by the large-scale structures. Following burn-out and re-entrainment, significant pre-mixing of the relatively cool, soot-laden fuel in the eddies and the surrounding air may have occurred. Under these conditions, some premixed combustion will result. In premixed combustion, the flame surface is not trapped to the mixing surface but can move through the premixture at a rate given by the premixed laminar flame speed. The possible presence of both premixed and non-premixed combustion occurring within fires is another example of the complexity involved in fire phenomena.

For regions of the fire undergoing diffusive combustion, the rate at which the fuel vapor is being consumed in the fire by diffusive combustion processes can be defined by the product of two terms: 1) interface area between fuel and air that is burning and 2) the combustion rate per unit area. The interfacial area is controlled both by momentum processes as shown in Figure 38 and by scalar processes as shown in Figure 39. Burn-out of either the fuel or the air results in a decrease in the interfacial area, thereby limiting area growth from turbulent mixing processes. The combustion rate per unit area is affected by the local strain field produced by the turbulence at length scales within an order of magnitude of the flame thickness.

As discussed previously, the flame affects the local turbulence field through two ways: dilatation and baroclinic vorticity generation. As shown in Figure 26, dilatation results in a decrease in the rotational velocity of rotating structures. This is often referred to as laminarization in the jet combustion literature (see Takagi et al., 1981). As shown in Figure 37, baroclinic vorticity generation by the flame does not account for net circulation through the flame zone. However, the difference in density between the fuel on one side and the air on the other side does. It is interesting to consider how much of the wrinkling in Figures 23 through 25 is caused by: 1) local baroclinic vorticity generation, 2) advected turbulence cascading down to dissipative scales, or 3) other combustion induced instabilities. Visualization is not sufficiently quantitative to address such questions. However, the

Flow Strained
Diffusive
Combustion

Air Depletion
Results in a
Decrease in
Combustion
Rate

Fuel Burnout
Results in a
Decrease in
Combustion
Rate
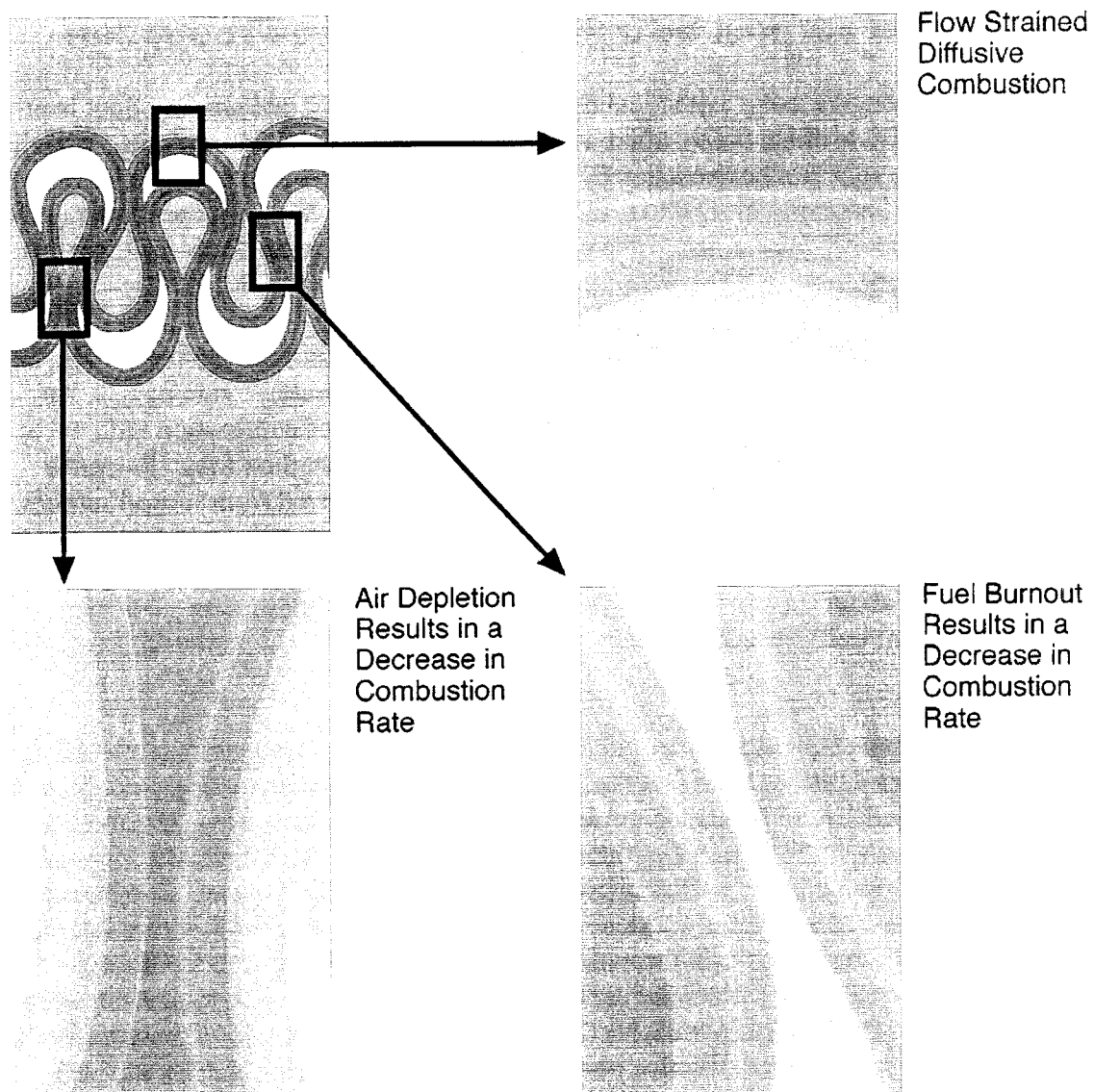
Figure 39.   Scalar Processes Affecting Combustion in Fires.

nature of the turbulence at the flame length scales is important in determining the local heat release rates through both the flame area and strain rates. Given that there is a source term for vorticity present at the combustion interface, it is unclear how much of classical turbulence theory applies around the flame zones. Further research in this area is clearly required.

Effect of Vortical Structures on Smoke Production

To avoid confusion, we make a practical distinction between soot and smoke. Soot is produced on the fuel side of the flame, often within millimeters of the flame surfaces. We will refer to smoke as soot that has penetrated the flame surface of the fire (by any of several means) and therefore exists in a primarily cool air environment. Visually, the smoke is the black cloud that surrounds the fire, while soot is typically seen as the flame itself (that is, luminous emission).

Soot and smoke in laboratory flames is an area of active research (see Hamins, 1993). In addition to the mechanisms for smoke production found in laboratory scale flames, we argue that smoke can be produced as a result of the interaction of combustion with medium-scale, turbulent-mixing processes in large liquid hydrocarbon fires. Evidence that turbulent mixing is a key parameter in large fires can be inferred from several sources. Fires require a minimum scale to be turbulent. Drysdale, 1985, summarized liquid regression and fire height data against the burning regime. He notes that fires are laminar up to a base diameter of about 0.1 m. From a base diameter between approximately 0.1 m to 1-2 m, the fires are transitionally turbulent. Above approximately 1-2 m, the fires are fully turbulent.

There are a number of changes in fire characteristics, as the fire diameter increases to the 1-2 m diameter level, that suggest that the role of turbulence in scalar mixing (and thereby the combustion and smoke formation processes) is important in large fires. Notarianni, et al., 1993, and Evans, 1994, report that the smoke yield in the plume above a fire increases with increasing fire diameter for fires up to approximately 2 m in diameter. For greater fire diameters, the smoke yield is constant at about 15%. Drysdale, 1985, shows that the liquid-fuel surface-regression-rate increases with increasing fire diameter for fires up to about 1 m in diameter. For greater fire diameters, the liquid-fuel surface-regression rate is constant at approximately 5 mm/min. McCaffery, 1979, and Hagglund and Persson, 1976, show that the average surface emissive power (thermal radiation from the fire surface) increases with increasing fire diameter for fires between 1-2 m in diameter. For fire diameters between 1 and 20 m, there is a large decrease in the average surface emissive power with increasing fire diameter, from an approximate average of 130 kw/m^2 to 40 kw/m^2. Further increases in fire diameter between 20 and 100 m also result in a decrease in average surface emissive power with increasing fire diameter; however, the decrease is much less pronounced, from about 40 kw/m^2 to 20 kw/m^2, respectively. Further, from the 18.9 m diameter pool fires shown throughout this report, we have noticed that smoke is formed from soot, which is transported in turbulent eddies along the sides of the fire. The eddies are typically on the order of a meter in diameter when the smoke first appears.

Smoke is formed at a short distance up from the toe of the fire, and large fractions of the external surface of the fire are shielded by the smoke layer.

To explain these data, we have postulated a mechanism based on turbulent mixing that is at least partly responsible for the smoke formation in turbulent liquid hydrocarbon fires. We propose that smoke is formed from soot inside of eddies on the order of a meter in diameter or larger. The proposed process is shown in Figure 40. As we argued previously, there is a tight coupling between the scalar density field and the underlying velocity field through the baroclinic vorticity generation mechanism that distinguishes buoyant flows from momentum driven flows. As a result of this tight coupling, rotational motion is produced along the interface between the hot plume and the cold surrounding air. The surface of the fire marks the interface between fuel and air.

As shown in Figures 29 and 30, kinematics at the interface between the hot plume and cold air suggest flame surfaces, about equal parts air and hot fuel, are entrained in a rotational structure as it amalgamates. Combustion occurs simultaneously with the amalgamation process along the flame zones between the air and the fuel. Combustion continues until one or both of the reactants are depleted from the eddy (assuming that local quench-
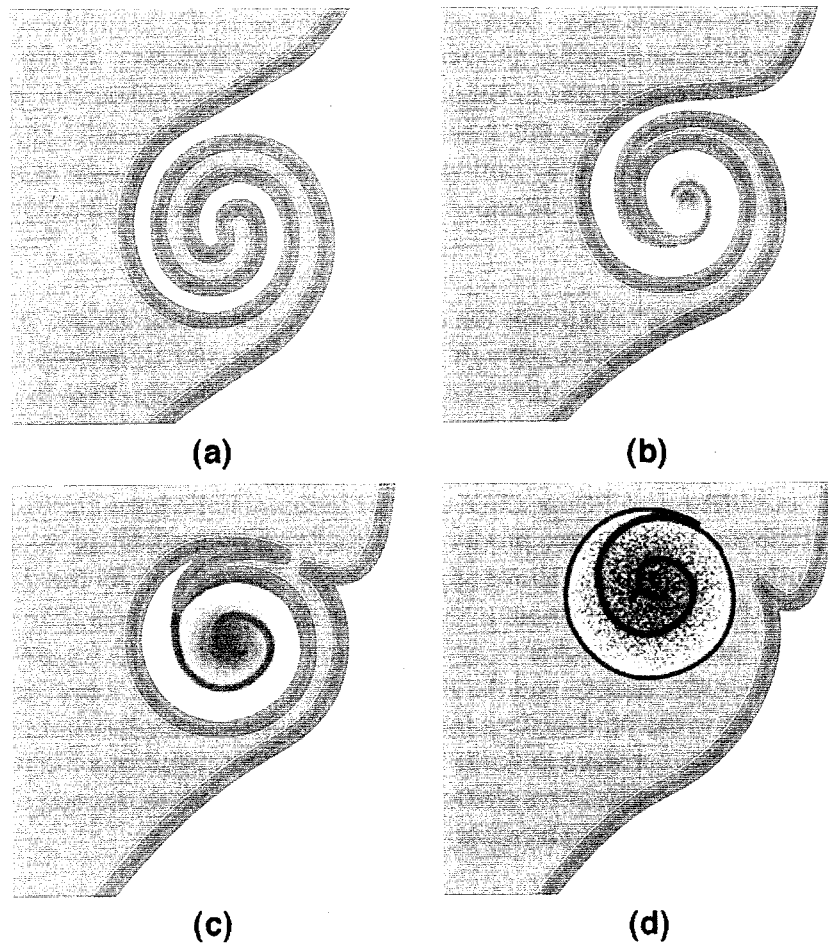

(a) (b)

(c) (d)

Figure 40. Proposed Mechanism for Smoke Formation in Fires. See text for explanation of the process.

61

ing does not occur because of turbulence or other means). Stoichiometry for typical hydrocarbon fuels requires between 10 to 100 times the amount of air as fuel on a volume basis (for fuels ranging from methane to heavy liquid hydrocarbons, respectively). Even if pyrolysis occurs, reducing the fuels to the methane/ethane level, the amount of fuel contained within the eddy is, by a factor of 10, greater than what can be consumed by the available air in an eddy.

Soot is formed within the eddy during combustion, caused by pyrolysis occurring as a result of the interaction of the fuel and high-temperature products on the fuel side of the flame zone. Soot may also be present from previous pyrolysis because of the high temperatures within the vapor dome. In addition, soot production continues after the burnout of the air because hot combustion products will continue to be intermixed with excess fuel. Because there is no air present within the burned-out eddy, no oxidation of the soot will occur unless the eddy mixes with air and becomes reignited. We propose that combustion products surrounding the hot, fuel-rich eddy interfere with the formation of ignitable mixtures on the surface of the eddy, thereby preventing its reignition by the adjacent flame surface. Because the burned-out eddy is at a relatively high temperature compared to an air / product mixture on the exterior of the flame surface, the eddy lofts upward away from the flame surface because of buoyancy. Soot production ceases as the hot eddy cools both radiatively and by mixing with cooler air (and/or air/product mixtures). As the eddy cools, the soot in the interior agglomerates to become smoke. There is evidence in small-scale combustion experiments to support this mechanism. Recently, Gutmark et al., 1995, have shown that soot can be suppressed by timing air injection to coincide with vortex formation in a forced plume. This is consistent with observations of fires such as that shown in Figure 17.

This proposed mechanism also explains the observed data discussed above. A minimum fire diameter is required to generate enough vorticity (i.e., rotational velocity at a given scale) causing circulation to form eddies that entrain air and fuel faster than the flame zone will consume them. This rapid entrainment is necessary to form the fuel-rich pockets embedded in the rotating eddy before the flame zones in the eddy consume the air present. In transitionally turbulent fires below about a meter in diameter, eddies are formed but do not result in sufficient entrainment to produce hot, fuel-rich pockets when the air is consumed, though fully turbulent fires above approximately a meter do. As the fire diameter is increased and the flow becomes more turbulent, the flame surface becomes wrapped around more eddies, making it thicker in that along any line of sight, there are several flame surfaces between the surface and the interior of the fire. As the flame becomes "thicker," the radiation to the pool surface increases. However, once the flame is optically thick in a radiative sense, increases in flame thickness will not result in a higher fuel evaporation rate. Hence, for fire diameters above about 1 m, increases in diameter will not increase the fuel evaporation rate (Drysdale, 1985).

Similarly, for radiative heat flux to an object on the outside of the fire, the increasing optical thickness of the convoluted flame surfaces will result in higher heat fluxes up to approximately 1-2 m. However, above 1-2 m smoke formed in the eddies will shield the hot flame zones. As the fire size increases above 1-2 m, an increasing fraction of the sur-

face area of the fire becomes radiatively blocked by the somewhat cooler, smoky eddies. As a result, the average emissive power (kw/m^2) of the fire decreases with increasing scale. However, only a fraction of the fire surface is covered with a smoke layer. Therefore, as the blockage of the luminous soot zones becomes complete, the average emissive power should become somewhat independent of scale. Thus, the increasing, decreasing, and leveling of the average surface emissive power with increasing fire diameter (McCaffery, 1979; Hagglund and Persson, 1976).

Our observation has been that smoky eddies moving along the sides of the fire are re-entrained by larger eddies farther up from the base of the fire. The scale of the eddies along the surface of the fire increases continuously by amalgamation until the eddies reach the scale of the fire radius, or fire diameter. The largest eddies typically form at an approximate elevation of one radius to one diameter above the fire. Because the end of the continuous flame zone is two to three diameters above the fire, smoke formed in smaller eddies along the edge of the fire gets entrained and potentially recombusted in these very large eddies. The burnout of these diameter-sized eddies then determines the overall smoke yield above the fire. This observation is consistent with the smoke yield data reported by Notarianni, et al., 1993, and Evans, 1994, indicating that the smoke yield in the plume above the fire is constant for fire diameters above 1-2 meters.

The mechanism proposed above does not explain smoke formation in smaller fires and is not meant to imply that other mechanisms for smoke production do not exist. Clearly, smoke is produced at the tip of small flames above burners under certain flow conditions, which is not explained by the mechanism proposed. However, in large fires the amount of smoke produced is copious, and it is difficult to determine how existing mechanisms of smoke formation (such as by soot penetration of flame zones) can account for the amount and the location at which the smoke appears to form.

Effect of Turbulence on Radiative Properties

Fires are comprised of a participating media. As such, radiative transport through them is an extremely nonlinear process. Because of the high soot loadings, it is generally accepted that thermal transport from a large hydrocarbon pool fire is primarily caused by the soot (as opposed to gas) emission. Assuming that the soot particles are small and that radiative scattering can be ignored, the principal variables governing radiative transport are the soot volume fraction and the temperature. Radiation is dependent on the soot volume fraction through an exponential extinction coefficient and on the temperature to the fourth power.

The source terms for both temperature and soot are the flame zones that are primarily diffusively controlled processes (at least at low turbulence levels). However, because temperature and soot are scalar properties, their transport is governed by convective time and length scales. As a result, there are significant spatial and temporal fluctuations in the radiation transport within a fire at convective time and length scales.

Therefore, there will be large fluctuations in radiative transport on the time scales of the turbulence. These large property and temperature fluctuations, and the highly nonlinear nature by which they determine the radiative transport, require that the convective time and length scales are resolved to predict thermal loading adequately. This observation has important implications for the modeling of fires because the equations of motion are traditionally time-averaged over the turbulence time scales. If time-averaged equations are used, then a first-order-accurate, computationally efficient means of estimating the time-averaged radiative transport must also be defined.

Numerical Simulation of Vortical Structures in Pool Fires

As demonstrated in previous sections, convective turbulent motion plays a role in a broad range of both the length and time scales involved in fires. The first section of this report identified vortical structures with sufficiently small length scales to tightly bend the flame fronts on the millimeter scale up to ring-like vortex structures that had length scales on the order of the fire diameter (many meters). The time scales range from the Kolmogorov times for submillimeter eddies on the order of milliseconds to the puffing frequencies on the order of seconds for large diameter fires. In addition to the convective length and time scales, fires involve diffusive length and time scales, from the submillimeter and submilli-second range required for resolution of species diffusion gradients in flame zones to the tens of meters and thousands of seconds required to resolve the length and time scales of a fire/object interaction. In all, more than five orders of magnitude in temporal and spatial resolution are required to simulate directly all of the relevant scales.

Unfortunately, given the present level of computational resources, no numerical simula-tion tool is capable of simultaneously resolving all required length and time scales associ-ated with fire phenomena. There are basically two approaches: either starting with the smallest length scales and resolving all the physical processes up to the largest length scales that one can compute, or starting with the largest length scales and resolving down-scale with as many grid cells as one can compute. The first approach is a direct numerical simulation (DNS) and is preferable from a scientific perspective. However, the largest length scales that can be modeled are on the order of centimeters. Even with the tremen-dous growth in both speed and memory for computing hardware, DNS will likely be lim-ited to length scales significantly smaller than the diameter of large fires. The second approach uses engineering simulation. Physical mechanisms with length scales below the minimum that can be resolved are "modeled" with mathematically ad hoc assumptions that attempt to represent the physical phenomena as realistically as possible. The engi-neering approach is used here, with models for combustion, soot, and turbulent processes.

Time scales also play a role in the selection of the approach used to model the turbulent processes. From fire observations, the rotational structures can be divided into two classes: those that have time-mean definition at a fixed location and those that do not. The columnar vortices are relatively steady and have a temporal mean definition. On the other hand, the ring- and ring-arc-like vortices do not have a definition in the mean because they are always convected with the flow. This distinction is important for determining the type of averaging used in the Navier-Stokes equations required to resolve the vortices.

The goal of the present numerical study is to evaluate two common means of averaging the Navier-Stokes equations, the Reynolds-Averaged Navier-Stokes (RANS), and the Large Eddy Simulation (LES). The effect of the averaging processes on the ability to resolve the large-scale coherent structures in fires is studied. The RANS equations are time-averaged, while the LES equations are spatially averaged. The RANS equations should resolve tur-bulent structures that have a time-mean definition relative to the turbulent time scales, but

will not resolve rotational structures that have no time mean definition. LES, on the other hand, should resolve spatially large structures that have no time mean definition. The scope of the present study is modest, as qualitative differences are sought rather than quantitative evaluation. Full implementation of an LES solution, with the concurrent full suite of verification and validation runs, is intended eventually.

To solve the Navier-Stokes equations in an engineering sense, it is necessary to average the equations so that those length and time-scales that can be resolved on a grid are represented in the averaged equations and those length and time-scales that must be modeled are represented by unresolved terms in the averaged equations. Or, for any variable, ϕ, the instantaneous value of the variable is

$$\phi = \bar{\phi} + \phi' \tag{3}$$

where $\bar{\phi}$ is the resolved variable in the averaged equations and ϕ' is the unresolved component of the variable that requires modeling.

The traditional RANS approach averages the governing equations in time. In RANS, the "resolved" component of the instantaneous variable is defined as the time-mean variable. Or, for any variable, ϕ, the resolved variables are defined as,

$$\bar{\phi} = \frac{1}{\Delta t} \int_{t}^{(t + \Delta t)} \phi \, dt \tag{4}$$

The time-scale over which the variables are averaged, Δt, is typically defined as "long" relative to the turbulence time scales of the problem. Given this definition, the modeled component, ϕ', is interpreted as temporal fluctuations caused by turbulent motion. The averaging time-scale, Δt, need not be infinite. Transient calculations can be conducted provided there is no statistical coupling between the resolved components undergoing the transient and the turbulent fluctuations. However, by the time-averaging assumption in Equations 3 and 4, solution of the RANS equations can only yield information on rotational structures that have a time-mean definition that is long relative to the modeled temporal fluctuations. Since the "turbulence" is being modeled as temporal fluctuations, it is necessary to average the equations over a time scale corresponding to the passage of a statistically significant number of the slowest (that is, largest) rotational structures.

The turbulence literature is rich with models that permit closure of the transport equations. Closure models range in complexity from simple mixing models to full second order closure of the Reynold stress terms by modeled terms in their transport equations. The solution method chosen is the standard two equation k-ε model. The k-ε model uses a mean-gradient approximation in the RANS equations, in which the inherently convective motion of turbulence is modeled as a diffusive flux with a nonlinear "turbulent eddy viscosity." By treating the convective turbulent motions as diffusive, the transient rotating structures appear in the solutions as diffusive mean flow velocity gradients.

It should be noted that RANS equations *by mathematical assumption* cannot resolve turbulence that has no time-mean definition. In actuality, if the mean-gradient "turbulent eddy viscosity" assumption closure model is used, one can begin observing turbulent eddies being convected in the solution. If the value chosen for the turbulent eddy viscosity is too small, then these transient features can be observed. (With zero eddy viscosity, the momentum equations are the same as in DNS - although the grid is too coarse for quantitative solutions, given the large length scales). An eddy viscosity must be calculated by the closure model as being sufficiently large that turbulent eddies are suppressed; otherwise, the averaging procedure is not strictly valid mathematically.

Large Eddy Simulation (LES) is another averaging procedure. In LES, the meaning of the resolved component and the modeled fluctuating component differs from RANS. Instead of time averaging, LES uses spatial averaging. Or, for any variable, ϕ, the resolved variables are defined as

$$\bar{\phi} = \int_{-\infty}^{\infty} G(x - \xi)\phi(\xi)d\xi \tag{5}$$

In Equation 5, G is a filter function. While G can be quite general, it can also be a "top-hat" function in which G is unity in a grid volume and zero elsewhere for each grid volume. In this case, the variable $\bar{\phi}$ becomes the volume average of the variable. The modeled variable, ϕ', is interpreted as the ensemble of instantaneous spatial fluctuations that have length scales smaller than the grid within the grid volume at a given time. The integration of all the spatial fluctuations will result in the volume average value.

Because the variables, and functions of the variables such as the derivatives, comprising the Navier-Stokes equations have not been time-averaged, LES permits temporal resolution of the flow-field for time scales less than the passage time for eddies that are larger than the grid. This approach permits vortical motions that are large relative to the grid to be resolved. This is the most attractive feature of LES. However, spatial averaging is not without disadvantages. In RANS, correlations between the nonlinear advective terms at the "resolved" level (called Leonard stresses) and correlations between the "resolved" and modeled terms (called Cross-stresses) are zero. In LES, these terms are still present in the mean flow equations. Therefore in RANS, the terms that need modeling are "only" the Reynold stresses, while in LES, Leonard, Cross, and Reynolds stresses require modeling.

To compare the RANS and LES approaches for capturing the large-scale structures, the same numerical model, with the same physical submodels except for the turbulence model, was used for both approaches. Buoyant production of turbulence was not modeled in either approach. A description of the numerical model follows. The RANS model and results will be presented, followed by the LES model and results.

Numerical Model

The VULCAN fire field model (under joint development at Sandia and at SINTEF/NTH, Norway) was used as a basis for both the RANS and the LES calculations. VULCAN is derived from the KAMELEON fire model (Holen et al., 1990).

VULCAN uses an extension of the SIMPLEC method of Patankar and Spalding, 1972, to solve the conservation equations for mass, momentum, and energy transport on a structured three-dimensional Cartesian finite difference grid. First- and second-order accurate upwind schemes can be used for the convective terms in the discretized partial differential equations. A staggered grid is used to solve for the x, y, and z velocities. The turbulence in the flow can be modeled by using either a standard two equation k-ε model or an LES formulation (both are discussed at length in subsequent sections).

The combustion model in VULCAN is based on Magnussen's EDC (or Eddy Dissipation Concept) (see Magnussen et al., 1979, or Magnussen and Hjertager, 1976). The EDC is a general concept for describing the interaction between the turbulence and the chemistry in flames. The EDC assumes that the combustion process occurs in the turbulent fine structures, which are modeled as perfectly stirred reactors. The version of the EDC employed in this study uses irreversible, infinitely fast combustion assumptions. The infinitely fast combustion assumption does not allow for finite rate chemistry effects. However, an extinction test is included in the model. Local extinction is assumed to occur when the time scale for turbulent mixing (calculated based on the turbulence model) is less than the chemical time scale, which must be pre-calculated by the user and entered as an input to the model. It should be noted that the EDC can also be formulated in other ways (e.g., equilibrium chemistry or finite rate formulations), if desired.

The modeling of soot formation is based on a two step process first proposed by Tesner, et al., 1971, for acetylene fuel. The first step treats the formation of radical nuclei, and the second step treats the formation of soot particles from the radical nuclei. Magnussen, 1989, has modified the formulation for application to fuels other than acetylene. Once soot is formed, the EDC is also capable of modeling the combustion of soot in the flame.

Thermal radiation of the combustion products (including soot, CO_2 and H_2O) is modeled using the Discrete Transfer Method of Shah, 1979. This method is used primarily because it represents an acceptable compromise between computational speed and accuracy for many problems. The soot and combustion gases are treated as a gray gas with an effective absorption and emission coefficient based on the local concentrations and temperature.

The eddy viscosity near solid surfaces is calculated using the logarithmic wall function method of Launder and Spalding, 1972. A similar approach is used to model the convective heat transfer to solid surfaces. The transient thermal response of solid surfaces is included in VULCAN.

RANS Approach and Results

Model Description

Reynolds stresses are modeled as a mean gradient times a turbulent eddy viscosity,

$$\bar{\rho}\overline{u_i'u_j'} = \mu_t\frac{\partial\bar{u}_i}{\partial x_j}. \tag{6}$$

Scalar convective fluxes are closed in a similar fashion with a mean gradient approximation in which the turbulent eddy viscosity is divided by a turbulent Prandtl/Schmidt number, that is,

$$\bar{\rho}\overline{u_i'u_j'\Phi'} = \frac{\mu_t}{\sigma_\Phi}\frac{\partial\bar{\Phi}}{\partial x_j}. \tag{7}$$

The turbulence model is a standard two equation $k - \varepsilon$ model formulation. The turbulent eddy viscosity is defined as

$$\mu_t = c_\mu\rho\frac{k^2}{\varepsilon}. \tag{8}$$

The transport equation for turbulent kinetic energy is

$$\frac{\partial}{\partial t}(\rho k) + \frac{\partial}{\partial x_i}(\rho u_i k) = \frac{\partial}{\partial x_i}\left(\frac{\mu_t + \mu_l}{\sigma_k}\frac{\partial k}{\partial x_i}\right) + \mu_t\left(\frac{\partial u_i}{\partial x_j} + \frac{\partial u_j}{\partial x_i}\right)\left(\frac{\partial u_j}{\partial x_i}\right) - \rho\varepsilon. \tag{9}$$

The transport equation for the dissipation of turbulent kinetic energy is

$$\frac{\partial}{\partial t}(\rho\varepsilon) + \frac{\partial}{\partial x_i}(\rho u_i\varepsilon) = \frac{\partial}{\partial x_i}\left(\frac{\mu_t + \mu_l}{\sigma_\varepsilon}\frac{\partial\varepsilon}{\partial x_i}\right) + C_1\mu_t\left(\frac{\partial u_i}{\partial x_j} + \frac{\partial u_j}{\partial x_i}\right)\left(\frac{\partial u_j}{\partial x_i}\right)\frac{\varepsilon}{k} - C_2\rho\frac{\varepsilon^2}{k} \tag{10}$$

Values for the constants in the equations are given in Table 2.

Table 2. Standard k - ε Model Constants

C_μ	σ_Φ	σ_k	σ_ε	C_1	C_2
0.09	0.9	1.0	1.3	1.44	1.92

Model Results

Several open pool fire calculations using VULCAN in RANS mode with the k - ε model were performed to investigate the ability of such a model to capture the large-scale turbulent structures that exist in large pool fires. For the following RANS calculations, a first-order upwind scheme was used to discretize the convective terms. At the time these calculations were performed (which was before the development of the LES capability), no second-order scheme had yet been incorporated into VULCAN. The first-order upwind scheme is known to introduce more numerical diffusion into the results, relative to a second-order scheme. Because of the scoping nature of these calculations, they were given nominal values for wind speeds and have not been redone with a second-order scheme.

For all the following RANS calculations, an 18.9 m diameter pool fire with JP-4 fuel was simulated. Various wind speeds were used, generally corresponding to test conditions so that comparisons could be made. The domain modeled was 100 m × 100 m (horizontally) and 60 m high. The grid was generally a 30 × 30 × 20 mesh of control volumes within the domain, although some finer meshes were used to assess the grid sensitivity of the results. Relatively uniform grid spacing was used over the pool surface, approximately 1 m × 1 m (horizontal area per control volume). Significantly larger grid spacing is used as the boundaries of the domain are approached. Grid spacing vertically above the pool started at 0.6-1.0 m for the first control volume, and increased toward the top boundary.

All calculations were three-dimensional. The zero wind calculations were performed using a plane of symmetry through the center of the pool, while the nonzero wind cases were performed without the use of any symmetry boundaries. Constant pressure boundaries were used for the zero wind calculations, and on the downstream boundaries of the nonzero wind cases. For the nonzero wind cases, the upstream velocity is specified using an atmospheric boundary layer assumption on the profile. At such a boundary, the ratio of the velocity at any height relative to the velocity at a height of 10 m above the ground is given as a function of the height relative to a height of 10 m, assuming a power law relationship.

All calculations were performed in a transient manner using time marching until a relatively steady flame shape was achieved. This generally existed 10-20 seconds following ignition in the calculations. Time steps were generally limited to 0.1 seconds maximum, with smaller values used near ignition. Fuel evaporation from the pool was modeled using either a user specified value or a vaporization model based upon the incident local heat flux to the pool. The results were not highly sensitive to this choice, other than the results with the vaporization model generally predicted higher evaporation rates of fuel, and hence longer flame heights.

Four wind speeds were used in the calculations: 0 m/s, 1.4 m/s, 2.3 m/s, and 7.2 m/s. Comparisons can be made to photographs taken from large-scale tests conducted at NAWC, with approximately the same wind speed, pool size, and fuel. The wind speeds were selected from periods in the tests when the wind speed and direction was relatively steady. Fires of this size puff, producing large vortical structures with a relatively regular

frequency. But the nature of a RANS calculation, as discussed earlier, is to average the turbulence over an appropriate length of time. Therefore, to make a comparison of flame shapes between the RANS calculations and the test results, the test photographs were taken with very slow shutter speeds (4-30 seconds). The average puffing frequency for fires of this size is just under 1/3 Hz. A shutter speed of 4 seconds ensured that at least one puffing cycle was recorded on the exposure, providing a form of averaging of the test results for comparison. The test photographs are purely optical, and because flame emission is quite different (optically) than smoke emission, large regions of smoke along the flame surface sometimes obscure the flame emission in the test photographs. In contrast, the results of the RANS calculations are presented purely in terms of the calculated *instantaneous* temperature field. Because of the time averaging inherent in the RANS approach, the calculated results show little change from time step to time step (once the fire has established itself). Thus, a qualitative comparison of flame shapes can be made.

The results for the zero wind speed case are shown in Figure 41. The calculation results are presented in terms of instantaneous temperature field in a vertical plane through the center of the pool (the symmetry plane used in the calculations). The RANS mode calculation with a k - ε model produces a flame shape in good qualitative agreement with the test photograph. The puffing motions have been essentially averaged out in the RANS results. The result is a single column of flame and smoke that rises vertically, in good agreement with the time-averaged photograph.

A more interesting case is generated with a wind speed of 2.3 m/s. Because of the three-dimensional nature of the results, the calculation results are presented in terms of the maximum temperatures throughout the flame volume *projected* to a vertical plane through the center of the pool. This allows a better picture of the volume occupied by the three-dimensional flame surface. As shown in Figure 42, good agreement is again seen between the RANS-calculated flame shape and the test photograph. This slight wind tilts the flame
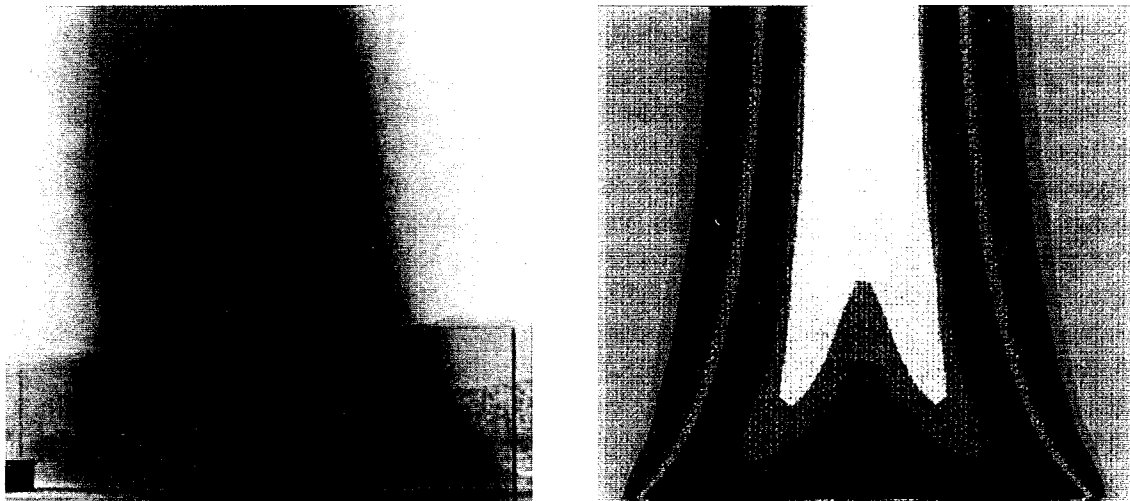

Figure 41.   Results of RANS Calculation with Zero Wind Speed: Flame Shape Comparison.   Left: NAWC test; conducted with a 0.7 m/s crosswind (see Figure 6). Right: RANS calculation with zero wind.
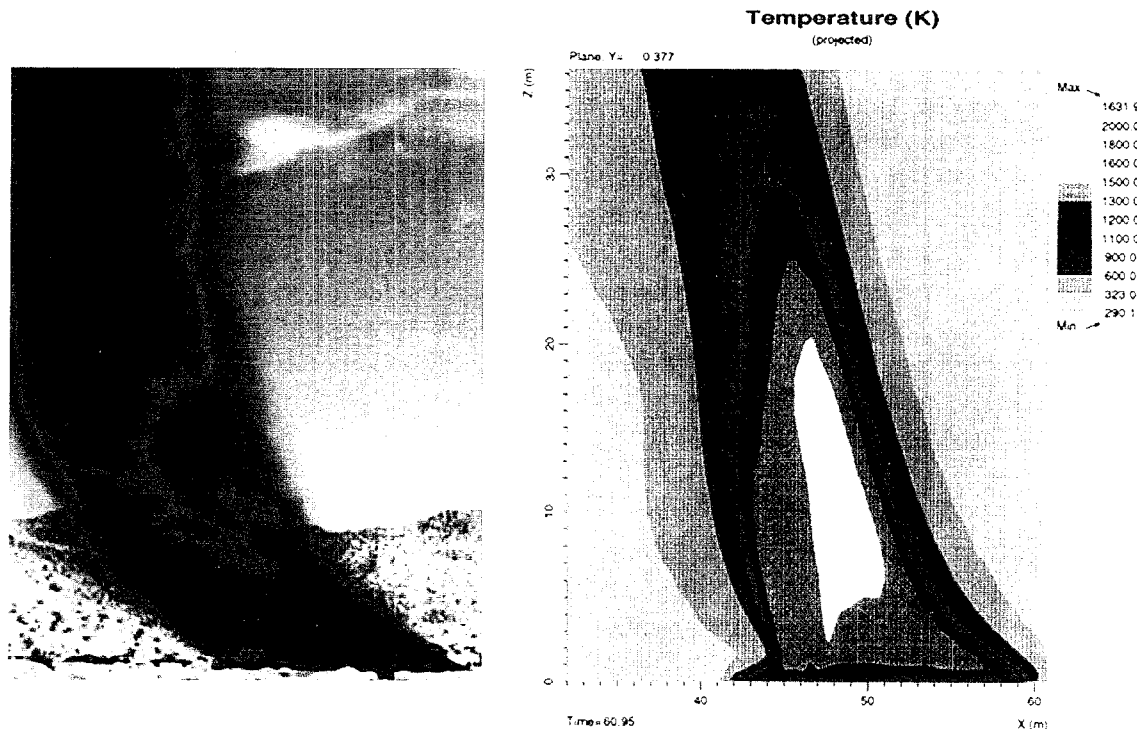
Figure 42. Results of RANS Calculation with 2.3 m/s Wind Speed: Flame Shape Comparison. Left: NAWC test; conducted with a 2.4 m/s crosswind (see Figure 10). Right: RANS calculation.

away from the vertical. There is reasonable agreement in the angles of tilt between the RANS results and the test results.

As discussed previously, crosswinds produce an interesting effect along the leeward side of the pool in the form of counter-rotating vortices. Because these structures have a time-mean definition, a RANS formulation should predict their existence. Figure 43 shows a vertical cross-section of temperatures through the calculation domain near the leeward edge of the pool, as predicted with the RANS formulation for the 1.4 m/s wind case. Also shown for comparison is a photograph (instantaneous) from a test with a 1.2 m/s wind. The photograph is taken from the leeward side of the pool, looking upwind. The RANS calculations are qualitatively in good agreement with the test photograph, as large, counter-rotating structures are predicted near the leeward edge of the pool. A horizontal plane through the calculation results (not shown) indicates that these two columns are indeed strong counter-rotating vortices. Both calculations and the photograph indicate an interior region between the columnar vortices free of flames. Several calculations were performed for this case to investigate the effect of grid refinement on the columnar vortices and flame shape. There was little effect of grid refinement on the flame shape. While grid refinement did not influence the general shape of the columnar vortices, it did cause some small change in the horizontal cross-section of these vortices.
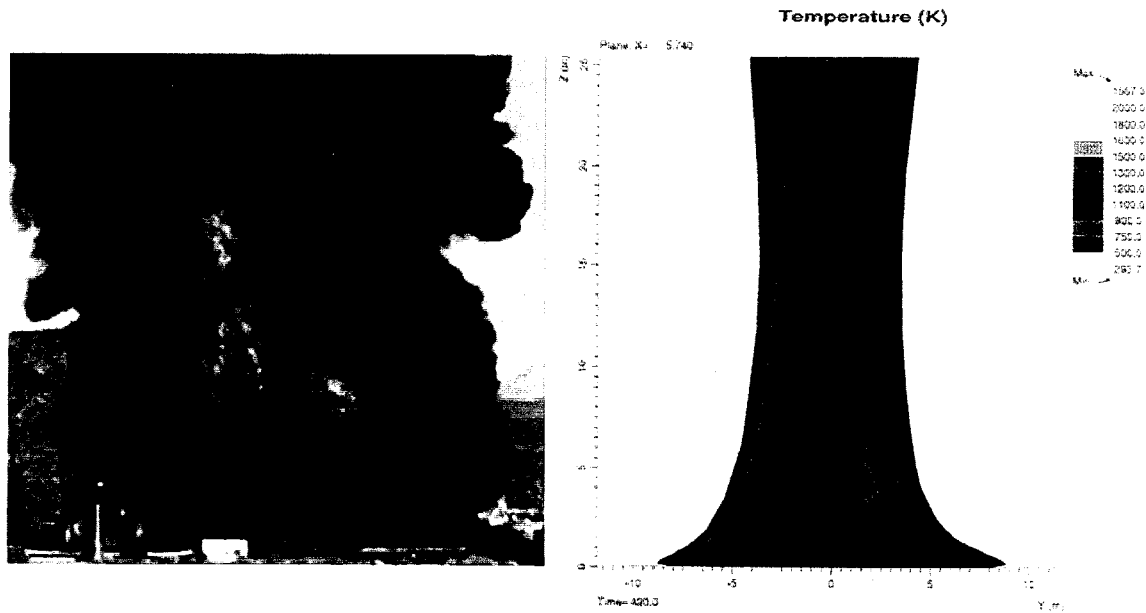
Figure 43. Results of RANS Calculation with 1.4 m/s Wind Speed: Comparison of Columnar Vortices Near Leeward Edge of Pool. Left: NAWC test, 7/13/94; conducted with a 1.2 m/s crosswind. Right: RANS calculation.

The results of a RANS simulation with a 7.2 m/s wind speed are shown in Figure 44, along with a photograph from a test with a 5.5 m/s wind speed. At the 5-7 m/s wind speed, the flame volume tilts much farther, and a portion of the flame zone lays on the ground beyond the leeward edge of the pool. The calculations indicate that the flame volume attaches to the ground for an additional pool diameter downwind of the pool. The test photograph, which is scaled for comparison with the calculations, indicates good agreement in flame attachment. The flame footprint, or the area near the ground, can also be

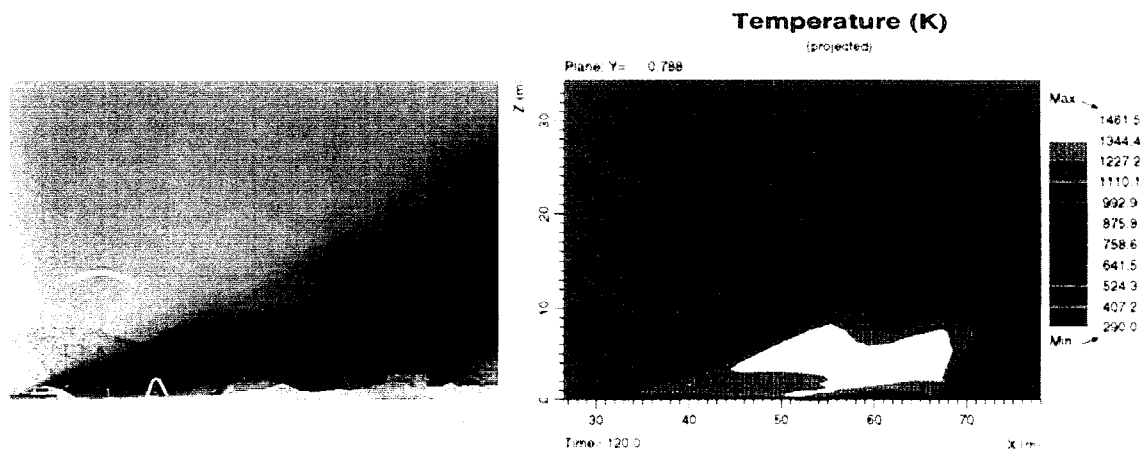Figure 44. Results of RANS Calculation with 7.2 m/s Wind Speed: Flame Shape Comparison. Left: NAWC Test, 3/18/94; conducted with a 5.5 m/s crosswind approximately 60° off the camera normal. Exposure time is 8 seconds. Right: RANS calculation.

visualized by looking at the temperatures in a horizontal plane just above the ground (Figure 45). For comparison, a post-test photograph is shown. The flame area in the test can be estimated from the region in the photograph that is free from soot deposition. The qualitative agreement is again good. The counter-rotating vortices that appeared in the 1.4 m/s wind speed fire are also present in the 7.2 m/s wind speed fire. They follow the streamwise direction and are close to the ground, tending to sweep fluid under and into the flame volume.

No puffing was observed in any of the RANS calculations once the calculations reached a steady state. As discussed previously, puffing motions will be suppressed when the eddy viscosity used in the calculations is high. In the above calculations, the suppression of puffing is caused by either the long time scales over which the turbulence is averaged in the k - ε model or significant numerical diffusion because of the first order upwind scheme used. Further investigations will be required.

It should be noted, however, that even with a standard k - ε model, the initial puff or fireball that forms during the initial transient, as the fire plume establishes itself after ignition, is always calculated. The rollup of this initial ring vortex is not suppressed by the eddy viscosity in the standard k - ε model, even though the ring vortices formed during the quasi-periodic steady-state are effectively suppressed. However, the initial puff or fireball has no time mean definition just the same as the azimuthal ring vortices. Further, the initial ring vortex associated with the starting transient is not necessarily stronger than those formed during the quasi-periodic steady state.

We conjecture that the initial ring vortex is captured because a finite length vortex sheet has a very strong tendency to roll up on itself. If the edge of the fire is viewed as a vortex sheet, as suggested heuristically by Figure 30, then during the initial transient the sheet is no longer than the growing fire plume. The initial ring vortex is the vortex at the end of this finite length sheet and forces the sheet to roll up on itself. On the other hand, during
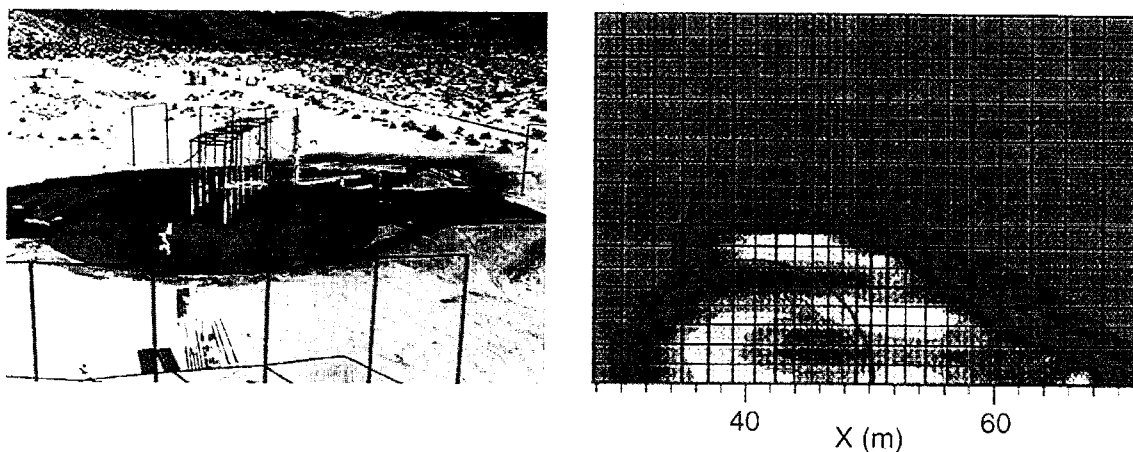

Figure 45. Results of RANS Calculation with 7.2 m/s Wind Speed: Flame Footprint Comparison. Left: NAWC Test, 3/18/94 (see Figure 15); Right: Temperature near ground in RANS calculation.

the quasi-periodic steady state the fire completely exits the computational domain and can be considered an infinite sheet. In this case, there is no end vortex and the eddy viscosity in the standard k - ε model effectively prevents the infinite sheet from becoming unstable, producing roll up.

LES Approach and Results

Model Description

The current study uses traditional closure assumptions for LES, except for the turbulent eddy viscosity model. It was assumed that the Leonard stresses and Cross stresses are zero everywhere, that is, they have been ignored. The Reynold stresses are treated by the same eddy viscosity treatment used in Equation 6, and the scalar fluxes are treated the same as in Equation 7. The usual subgrid model for LES, using an eddy viscosity model treatment, is the Smagorinsky model. It was simpler to modify the VULCAN code to implement a k - L subgrid model because it already had the k - ε model implemented, and the combustion model requires k - ε as input.

Because the objective was to tie the turbulence to the grid, the use of the grid to calculate the local length scale precluded using one of the transport equations. The dissipation equation (Equation 10) was dropped, because it is an assumed equation, while the k equation has a theoretical basis. Then an algebraic relation between k, L, and ε was used to pass ε and k to the combustion model so that no changes were required in the model formulation. The model is similar to that proposed by Deardorff, 1980.

The equations and constants for the subgrid model are as follows.

The turbulent eddy viscosity is defined as

$$\mu_t = c_\mu \rho L k^{1/2}. \tag{11}$$

Transport equation for turbulent kinetic energy is the same as Equation 9.

The grid definition for the turbulent length scale is

$$L = (\Delta x \Delta y \Delta z)^{1/3}. \tag{12}$$

The relation for the dissipation of turbulent kinetic energy is

$$\varepsilon = c_\varepsilon \frac{k^{3/2}}{L}. \tag{13}$$

Values for the constants in the equations are given in Table 3.

Table 3. k - L Model Constants

C_μ	σ_Φ	σ_k	c_ϵ	C_1	C_2
0.0856	0.42	1.0	0.845	1.44	1.92

The constants in Table 3 were taken directly from the derivation of Schmidt and Schumann, 1989, based on nonbuoyant turbulence. A second-order accurate advection scheme was implemented into VULCAN to perform the LES simulations with reduced numerical diffusion.

Model Results

Because the structures that cause puffing in no wind scenarios have no time-mean definition and cannot be resolved with a RANS approach, the ability of the LES approach was evaluated to determine the puffing frequency. A relatively coarse $35 \times 35 \times 38$ grid was chosen, as shown in Figure 46. A double plane of symmetry was chosen to reduce the effect of grid coarseness on the results. However, the choice of the double symmetry plane also precluded capturing the asymmetric (± 1) mode present with the puffing (0) mode in plumes and jets.

A typical instantaneous result is shown in Figure 47. The simulation was conducted with methane at a fixed inlet mass rate of 0.077 kg/m^2/s. The horizontal cross-section near the base of the fire shows the relatively cool vapor dome in the center. While the cross-section of the rising eddy is not perfectly symmetric (for unknown reasons, although unequal grid size is a possibility), it is clearly ring-like.

Animations were generated from several runs with different fuels and at different fire diameters. Puffing was seen in each, although the amplitude depended on the fuel type and generally decreased with decreasing scale. The puffing was periodic, but with some variation puff to puff. Figure 48 shows four frames from a puffing sequence for a 15.2 m diameter fire. This sequence can be qualitatively compared to the video sequence in Figure 5 (18.9 m diameter fire, NAWC) as follows: the first frame in Figure 5 corresponds roughly in phase with the second frame in Figure 48; the third frame in Figure 5 corresponds roughly in phase with the third frame in Figure 48; the fifth frame in Figure 5 corresponds roughly in phase with the fourth frame in Figure 48; and the seventh frame in Figure 5 corresponds roughly in phase with the first frame of Figure 48.

The animations were run over a statistically significant (> 20) number of puffs. The average frequency for the puffing was taken by counting the puffs on the animation and dividing by the total animation time. The results were compared against the experimentally measured puffing frequencies (Cetegen and Ahmed, 1993) in Figure 49. The calculated results show excellent agreement with the experimental data, demonstrating the potential of the LES method.
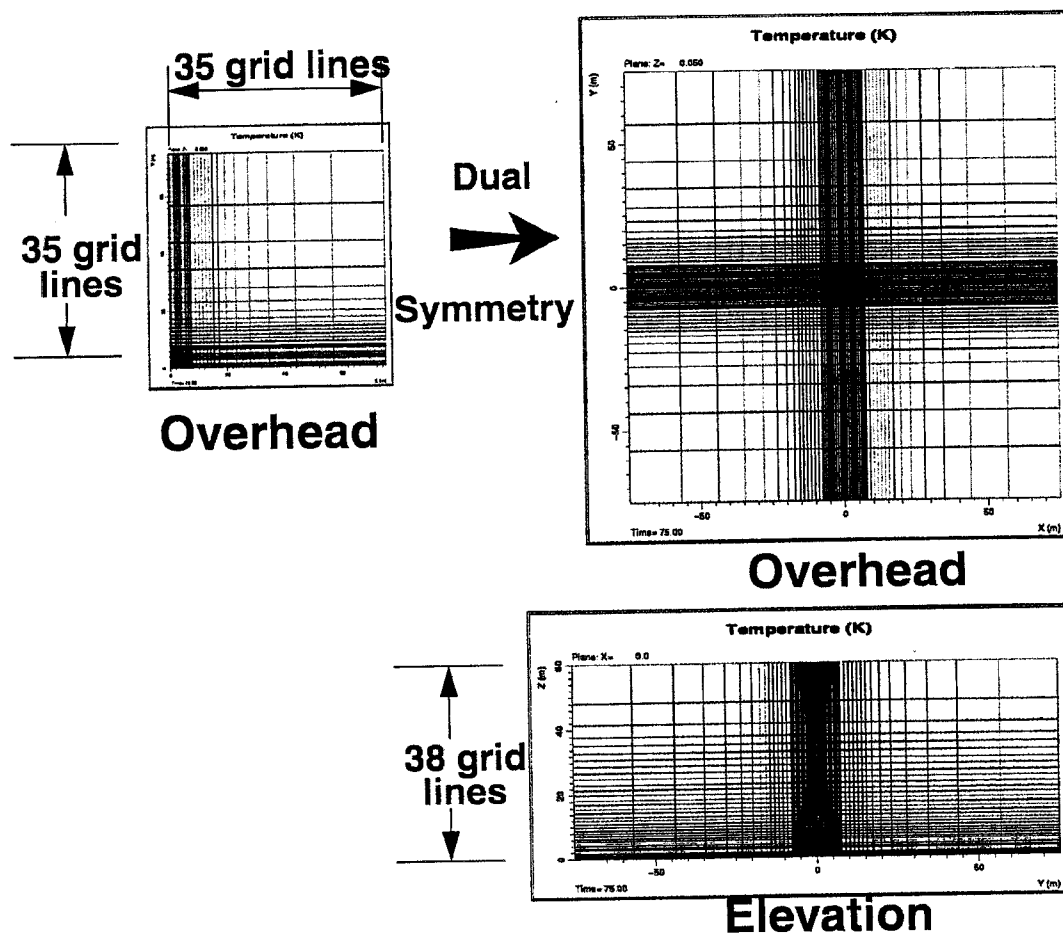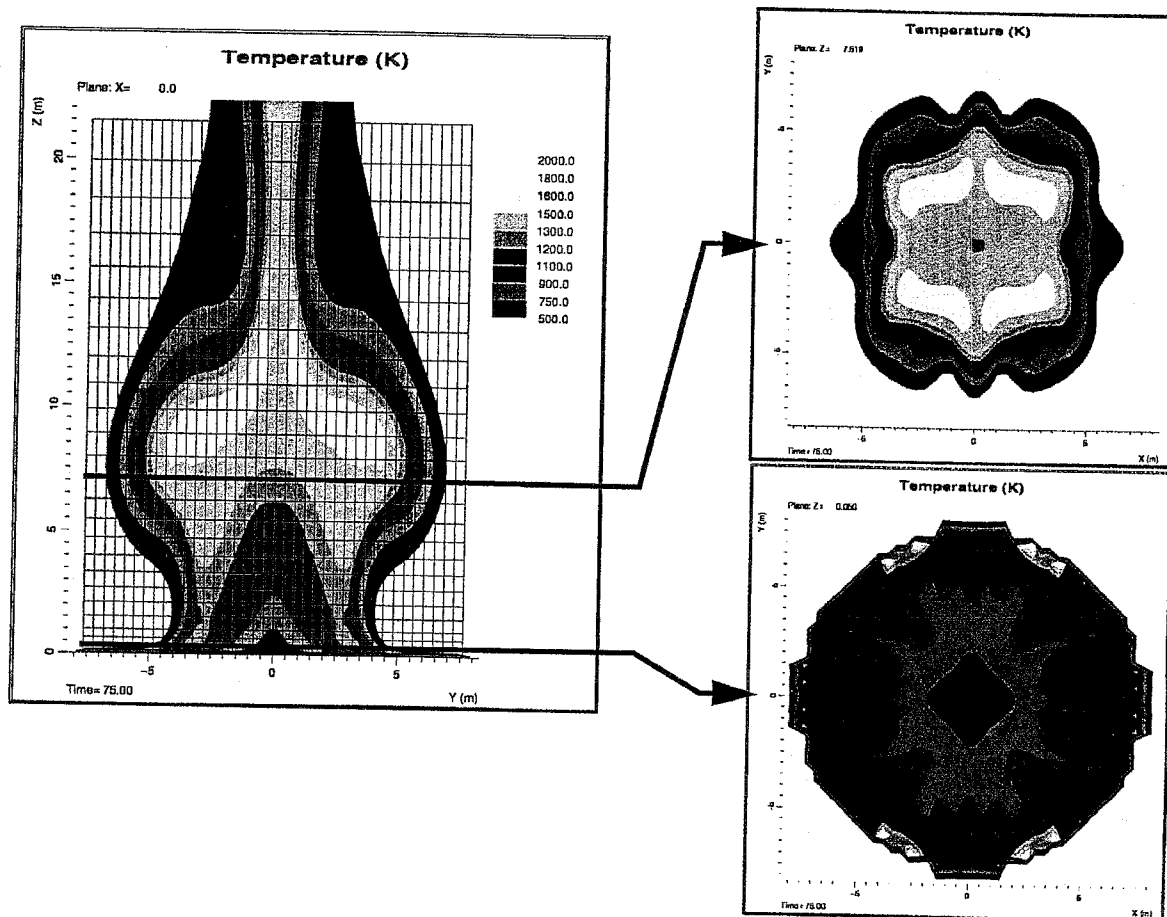
Figure 46.   Grid Used for LES Study.

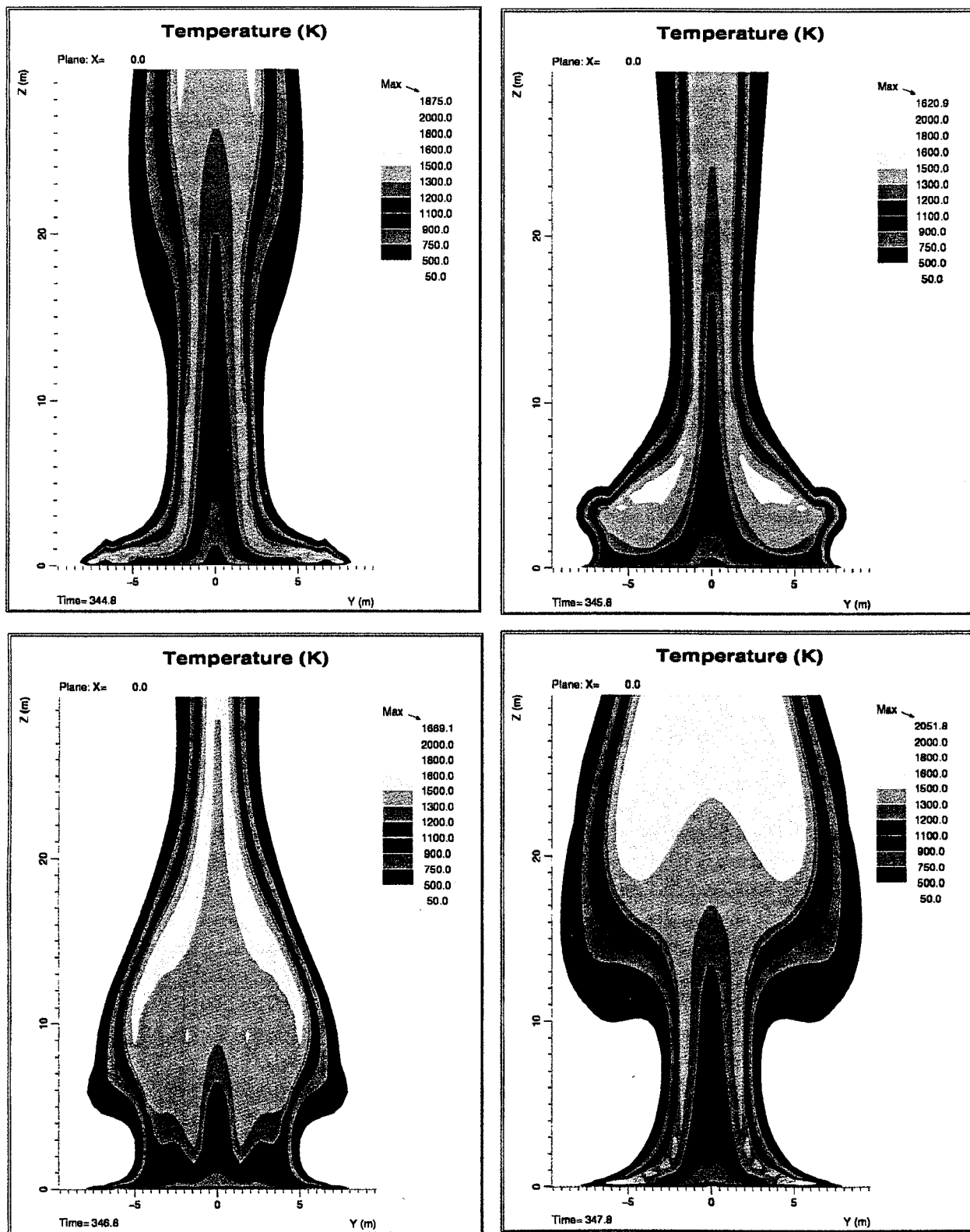Figure 47. Typical Instantaneous Result from the LES Solution.

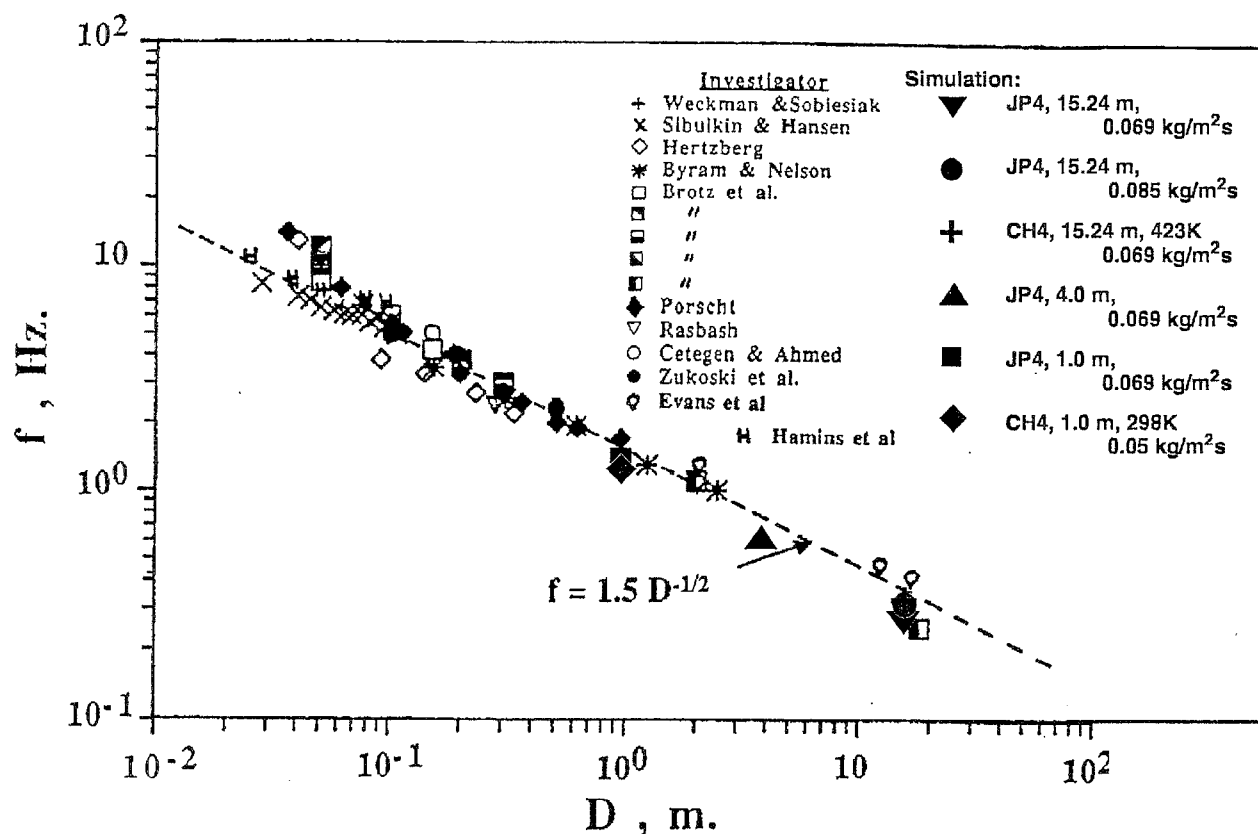Figure 48. Sequence of Frames Showing the Development of a Puff.

79

Figure 49. Comparison of Calculated and Experimentally Measured Puffing Frequencies. Experimental data reported in Cetegen and Ahmed, 1993.

Figure 50 shows comparisons of the time-averaged LES model results with thermocouple data for a JP-4 fire from a 15.2 m diameter pool (Johnson et al., 1982). The wind in the test was low, ~0.8 m/s, and the measured average mass flux was between 0.075 kg/m^2/s and 0.12 kg/m^2/s. The calculation used a mass flux of 0.077 kg/m^2/s and a running average was kept. The time-averaged result (averaged over a significant number of eddies) shows no evidence of the transient passage of those eddies that were resolved by the LES approach. The overall flame profile appears very similar to the RANS results in Figure 41, and the qualitative comparison with experimental data for the overall fire shape is good.

However, two caveats must be given. First, the code calculated gas temperatures that were not the same as thermocouple temperatures. Thermocouples are heated/cooled convectively and radiatively and can differ substantially from the local gas temperature. Second, the calculated time-averaged temperature values were not time step invariant. The height of the bulge varied somewhat with time step (unlike the puffing frequency, which was time step invariant for an order of magnitude change in time steps). Possibly, the simple time marching scheme employed was not sufficient to acquire stable statistics. Because of the scoping nature of the study, a pseudo-time stepping scheme, adequate for the time-aver-
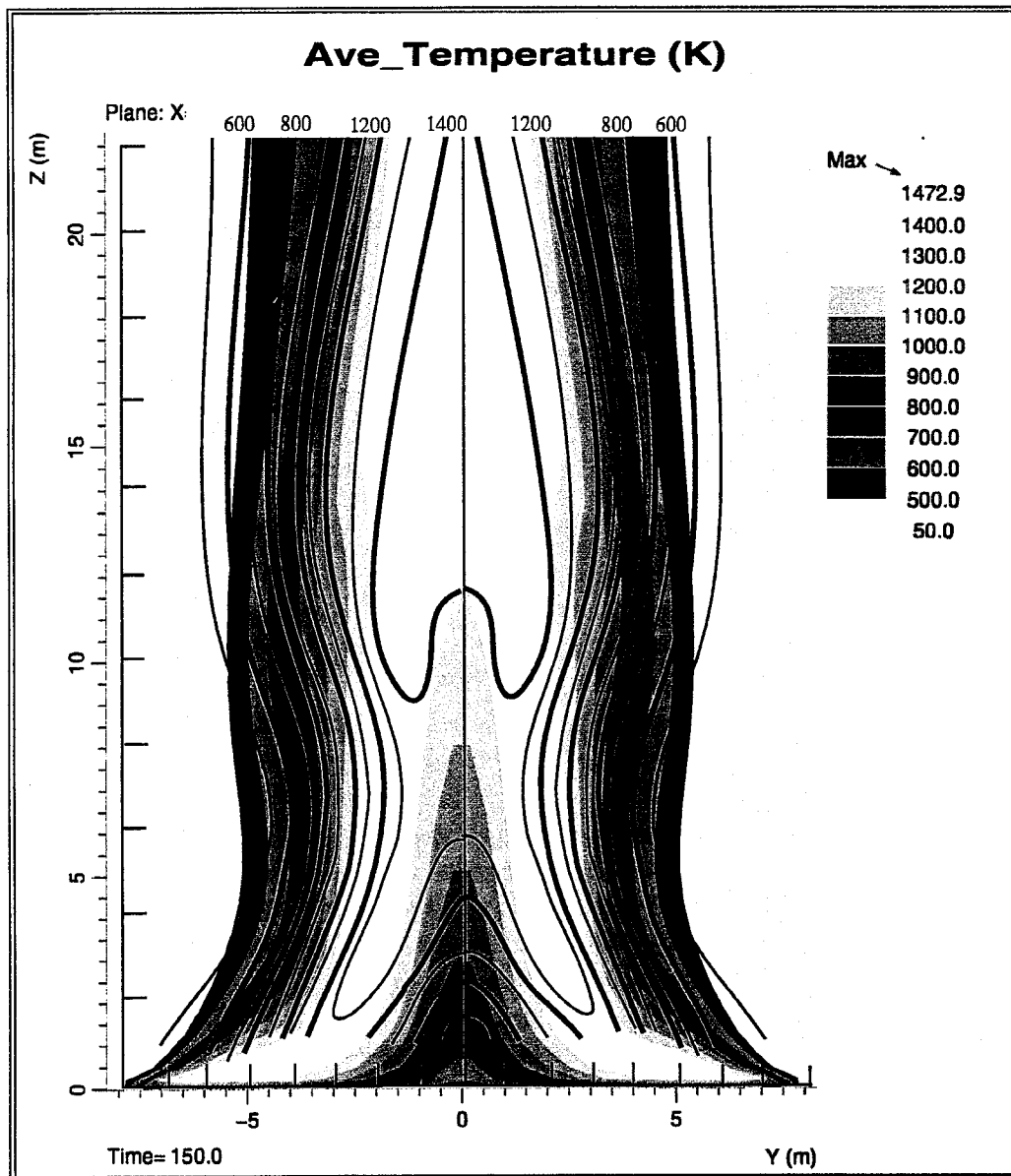
Figure 50. Comparison of Calculated Time-Averaged Temperatures and Experimentally
Measured Thermocouple Temperatures.

aged RANS approach, was used with only 40 to 80 time steps per puff instead of a rigorously time-accurate scheme.

The results also showed some interesting structures, as shown in Figure 51. Finger-like structures formed at the base of the calculation for the 15.2 m diameter fire. These structures are very reminiscent of finger-like structures on transitionally turbulent pool fires that are less than a meter in diameter. Because grid convergence studies were not conducted, one can only speculate on the results. However, physically, the flow at the base of
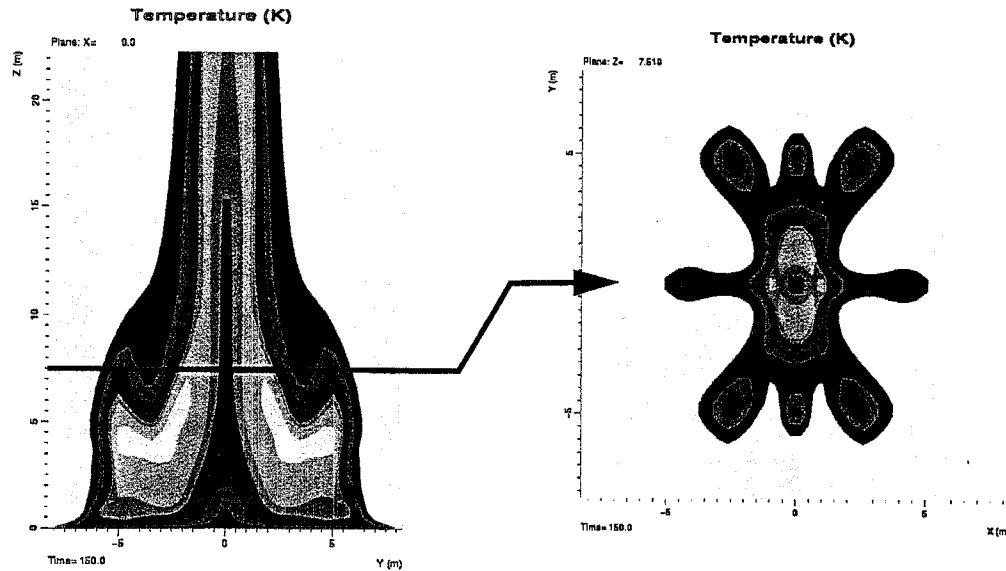
Figure 51. Finger-Like Structures in the Calculations at the Base of the Fire.

a fire has very low total circulation (that is, nearly laminar) because of the low flow veloc-
ities present. We have argued that baroclinic vorticity generation is responsible for much
of the rotational motion. Because this production mechanism is embedded in the fire sur-
face, some distance above the toe of the fire is needed to increase circulation substantially.
This effectively means that the fire undergoes a laminar to turbulent transition at a given
elevation above the toe. The turbulence model implemented is not adequate to predict this
transition, nor is the grid resolution sufficient to resolve these flows. However, the first
structures formed in the calculations above the grid level near the base of the fire appear
strikingly similar to the first turbulent structures that form in a transitionally turbulent fire,
even though the scale of the fire should be too large to permit such structures.

LES calculations for fires in crosswinds were not carried out for this study. However, LES
simulations by Baum et al., 1994, have shown that the smoke plume trajectories above the
fire can be predicted and that the twin columnar vortices present in a crosswind can extend
into the smoke plume for many kilometers. The columnar vortices are predicted in the cal-
culations even though the fire is modeled as a heat and smoke source.

While more work is needed to make the study results quantitative, the results to date
clearly show the potential for LES methods in fire simulation. The ability to resolve the
temporal fluctuations is important in determining the time-averaged heat flux to an object
because of the nonlinear nature of the radiative process. The time-average temperature to
the fourth power is not the same as the temperature to the fourth power averaged over
time. The difference can have a significant impact on the calculation of radiative heat flux.

82

Conclusions

Vortical structures with a range of length scales exist in large pool fires. Some structures are transient and some are relatively steady. The source of the vortical structures is speculated to be baroclinic vorticity generation. Amalgamation of smaller structures creates larger structures in a fire.

Because the vortical structures are a result of advection in the momentum equation, and advection processes are pervasive throughout the fire, the presence of these vortical structures affects a broad range of phenomena including entrainment, stirring, combustion, soot formation, smoke production, and radiation. Further, since fire is a natural balance, turbulent transport processes in a fire indirectly affect all aspects of the fire. Figure 52 shows the important phenomena in a fire and the interconnectivity between the phenomena.

While fires are a complex phenomena, engineering simulation of the dominant features is possible. Time-averaged RANS solutions are adequate for resolving turbulent structures that have a time-mean definition. However, they cannot capture the transient structures. Volume-averaged LES solutions can resolve transient structures that are larger than the grid resolution. Closure assumptions for both types of equations will remain suspect until the difference between the length scales and energy spectra in buoyant turbulence versus those found in momentum driven turbulence are clearly delineated because all closure models currently used are primarily based on momentum driven flows.
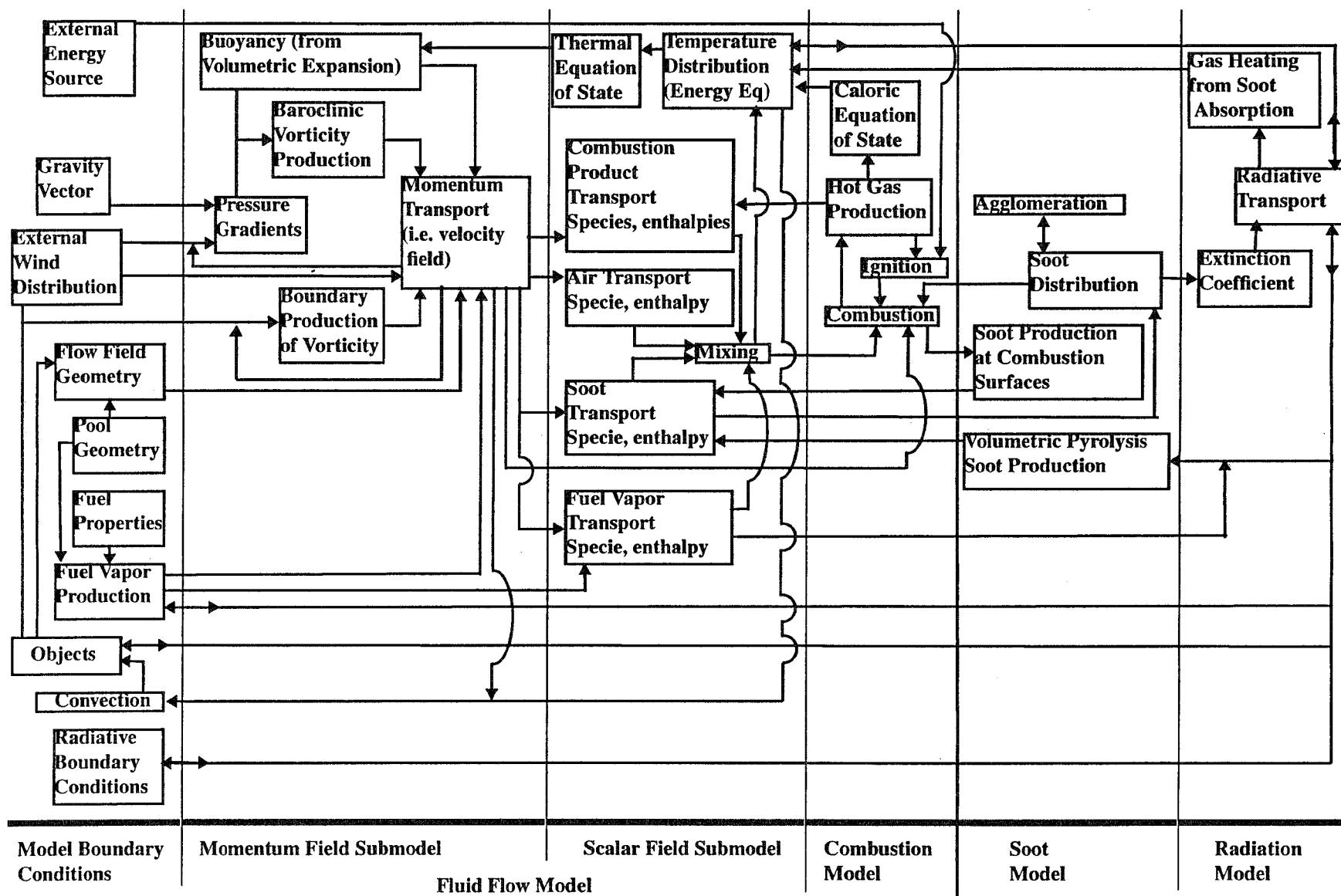
Figure 52. Summary of Important Physical Phenomena in Fires.

References

Baum, H.R., McGrattan, K.B., and Rehm, R.G., 1994, "Simulation of Smoke Plumes from Large Pool Fires," *The Twenty-Fifth Symposium (International) on Combustion*, The Combustion Institute, pp. 1463-1469.

Bernal, L.P., 1988, "The Statistics of the Organized Vortical Structure in Turbulent Mixing Layers," Physics of Fluids, A, Vol. 31(9), pp. 2533-2543.

Cetegen, B.M. and Ahmed, T.A., 1993, "Experiments on the Periodic Instability of Buoyant Plumes and Pool Fires," *Combustion and Flame*, Vol. 93, pp. 157-184.

Curran, H.J., Gaffuri, P., Pitz, W.J., Westbrook, C.K., Callahan, C., Dryer, F.L., and Held, T., 1995, "A Modeling Study of the Combustion of n-Heptane and iso-Octane in a High Pressure Turbulent Flow Reactor," Presented at the Joint Technical Meeting of the Combustion Institute, April 23, San Antonio, Texas.

Deardorff, J.W., 1980, "Stratocumulus-Capped Mixed Layers Derived From A Three-Dimensional Model," *Boundary Layer Meteorology*, Vol. 18, pp. 495-527.

Drysdale, D., 1985, *Introduction to Fire Dynamics*, John Wiley & Sons, New-York, p. 153.

Dai, Z. and Faeth, G.M., 1995, "Evaluation of Approximate Models of Buoyant Turbulent Flows," *Proceedings International Conference on Fire Research and Engineering*, 10-15 September (Eds. P. Lund and E.A. Angell), Society of Fire Protection Engineers, Boston, MA, pp. 141-146.

Evans, D.D., 1994, "In Situ Burning of Oil Spills: Smoke Production and Plume Behavior," National Institute of Standards and Technology, Gaithersburg, MD, NIST Special Publication 867 (N.H. Jason, Ed.), August, pp. 29-38.

Fric, T.F. and Roshko, A., 1994, "Vortical structure in the wake of a transverse jet," *Journal of Fluid Mechanics*, Vol. 279, pp. 1-47.

Gritzo, L.A., Moya, J.L., Nicolette, V.F., 1994, "Continuous Flame Zone Measurements and Analysis from Large, Open JP-4 Pool Fires including the Effects of Wind," *Proceedings of the 1994 NIST Annual Conference on Fire Research*, Gaithersburg, MD, October, Extended Abstract Only.

Gritzo, L.A., Nicolette, V.F., Moya, J.L., Skocypec, R.D., and Murray, D., 1995, "Wind-Induced Interaction of a Large Cylindrical Calorimeter and an Engulfing JP-8 Pool Fire," *Proceedings of the Symposium on Thermal Sciences in Honor of Chancellor Chang-Lin Tien*, Berkeley, CA, November 14.

Gutmark, E.J., Parr, T.P., Wilson, K.J., Schadow, K.C., 1995, "Application of Active Combustion control Via Synchronized Fuel Injection into Vortices," Presented at ISTP-8 and to appear in *Transport Phenomena in Combustion*, (S.H. Chan, ed.),Taylor and Francis.

Hägglund, B. and Persson, L., 1976, "The Hear Radiation from Petroleum Fires," Försvarets Forskningsanstalt, Huvudavdelning 2, 104 50 Stockholm, FOA Rapport C 20126-D6(A3), July.

Hamins, A., 1993, "Soot," *Environmental Implications of Combustion Processes*, (Ed. I. K. Puri), CRC Press, Boca Raton, Florida.

Hamins, A., Yang, J.C., and Kashiwagi, T., 1992, "An Experimental Investigation Of The Pulsation Frequency of Flames," *The Twenty-Fourth Symposium (International) on Combustion*, The Combustion Institute, pp. 1695-1702.

Hertzberg, J.R., Shepherd, I.G., and Talbot, L., 1991, "Vortex Shedding Behind Rod Stabilized Flames," *Combustion and Flame*, Vol. 86, pp. 1-11.

Holen, J., Brostrom, M., and Magnussen, B.F., 1990, "Finite Difference Calculation of Pool Fires, *The Twenty-Third Symposium (International) on Combustion*, The Combustion Institute, pp. 1677-1683.

Hottel, H.C., 1959, "Certain Laws Governing Diffusive Burning of Liquids," *F. Res. Abs. and Rev.*, 1, p. 41.

Johnson, H.T., Linley, L.J., and Mansfield, J. A., 1982, *Measurement of the Spatial Dependence of Temperature and Gas and Soot Concentrations Within Large Open Hydrocarbon Fuel Fires*, NASA Technical Memorandum 58230.

Lakkis, I. and Ghoniem, A., 1995, "Numerical Simulation of Time Dependent Phenomena in Large Fire Plumes," *Proceedings - International Conference on Fire Research and Engineering*, 10-15 September (Eds. P. Lund and E.A. Angell), Society of Fire Protection Engineers, Boston, MA, pp. 41- 46.

Launder, B.E. and Spalding, D.B., 1972, *Computer Methods in Applied Mechanics and Eng.* 3, p. 269.

Lewis, B. and von Elbe, G., 1987, *Combustion, Flames, and Explosions of Gases*, 3rd Edition, Academic Press, Orlando, Fl.

McCaffery, B.J., *Purely Buoyant Diffusion Flames: Some Experimental Results*, NBSIR 79-210, National Bureau of Standards, Gaithersburg, 1979.

Magnussen, B.F. and Hjertager, B.H., 1976, *The SIxteenth Symposium (International) on Combustion*, The Combustion Institute.

Magnussen, B.F., Hjertager, B.H., Olsen, J.G., and Bhaduri, D., 1979, *The Seventeenth Symposium (International) on Combustion*, The Combustion Institute, pp. 1677-1683.

Magnussen, B.F., 1989, "The Eddy Dissipation Concept," *Proc. of Eleventh Task Leaders Meeting*, IEA Working Group on Conservation in Combustion, Lund, Sweden.

Moorhouse, J., 1982, "Scaling Criteria for Pool Fires Derived From Large-Scale Experiments," *I. Chem. Sym.*, 71, pp. 165-179.

Morton, B.R. and Ibbetson, A., 1996, "Jets Deflected in a Crossflow," *Experimental Thermal and Fluid Science*, 12:112-133.

Notarianni, K.A., Evans, D.D., Walton, W.D., Madrzykowski, D., and Lawson, J.R., 1993, "Smoke Production from Large Oil Pool Fires," *Proceedings of the Sixth International Fire Conference*, Interflam '96, pp. 111-119.

Patankar, S.V. and Spalding, D.B., 1972, *Int. Jou. Heat and Mass Transfer*, Vol. 15, p. 1787.

Schmidt, H. and Schumann, U., 1989, "Coherent structure of the convective boundary layer derived from large-eddy simulations," *J. Fluid Mech.*, Vol. 200, pp. 51-562.

Shah, N.G., 1979, The Computation of Radiation Heat Transfer, Ph.D. Thesis, University of London, Faculty of Engineering.

Soma, S. and Saito, K, 1991, "Reconstruction of Fire Whirls Using Scale Models," *Combustion and Flame*, Vol. 86, pp. 269-284.

Takagi, T., Shin, H., and Ishio, A., 1981, "Properties of Turbulence in Turbulent Diffusion Flames," *Combustion and Flame*, Vol. 40, pp. 121-140.

Tieszen, S.R., 1995, "Fuel Dispersal Modeling for Aircraft-Runway Impact Scenarios," Sandia National Laboratories, Albuquerque, NM, SAND95-2529, November.

Tieszen, S.R. and Attaway, S.W., 1996, "Fuel Dispersal in High-Speed Aircraft/Soil Impact Scenarios," Sandia National Laboratories, Albuquerque, NM, SAND96-0105, January.

Tennekes, H. and Lumley, J.L., 1972, *A First Course In Turbulence*, The MIT Press, Cambridge, MA.

Tesner, P.A., Snegiriova, T.D., and Knorre, V.G., 1971, *Combustion and Flame*, Vol. 17, p. 253.

Welker, J.R. and Sliepcevich, C.M., 1967, "Wind Interaction Effects on Free Burning Fires," Tech. Report # 1441-3 to Office of Civil Defense of U.S. Bureau of Standards.

Distribution:

1   Boeing Defense and Space Group
        Attn: Earl E. Wilhelm
        P.O. Box 3707, MS 4C-67
        Seattle, WA 98124-2207

1   DODESB
        Attn: Mr. John E. Deplitch
        Hoffman 1
        2461 Eisenhower Ave.
        Alexandria, VA 22331

1   Director, Defense Special Weapon Agency
        Attn: CSTI
        6801 Telegraph Road
        Alexandria, VA 22310-3398

1   Director, Defense Special Weapon Agency
        Attn: Major Joe Crews
        6801 Telegraph Road
        Alexandria, VA 22310-3398

1   Director, Defense Special Weapon Agency
        Attn: James V. Brackett
        6801 Telegraph Road
        Alexandria, VA 22310-3398

1   U.S. Department of Energy
        Albuquerque Operations Office
        Albuquerque Headquarters
        Attn: H.T. Season
        P.O. Box 5400
        Albuquerque, NM 87115

1   U.S. Department of Energy
        Albuquerque Operations Office
        Albuquerque Headquarters
        Attn: R.O. Gergen
        P.O. Box 5400
        Albuquerque, NM 87115

1 U.S. Department of Energy
  Albuquerque Operations Office
  Albuquerque Headquarters
  Attn: Roger Cartee
  P.O. Box 5400
  Albuquerque, NM 87115

1 U.S. Department of Energy
  Albuquerque Operations Office
  Albuquerque Headquarters
  Attn: Karl Rueb
  P.O. Box 5400
  Albuquerque, NM 87115

1 En'Urga Inc.
  Attn: Y. Sivathanu
  1291-A Cumberland Ave.
  West Lafayette, IN 4 7906

2 FAA Technical Center
  Attn: Thor Eklund, Richard Lyon
  Fire Research Branch, AAR-423
  Atlantic City International Airport
  Atlantic City, NJ 08405

1 K-Tech Corp.
  Attn: Ned Keltner
  901 Pennsylvania NE
  Albuquerque, NM 87110

1 Kaman Sciences
  Attn: Wayne Young
  P.O. Box 7463
  Colorado Springs, CO 80933

1 Lawrence Livermore National Laboratories
  Attn: Doug Stevens
  P.O. Box 808, L-85
  Livermore, CA 94550

1 Lawrence Livermore National Laboratories
  Attn: Allen Kuhl
  P.O. Box 808, L-006
  Livermore, CA 94550

1   Lawrence Livermore National Laboratories
Attn: Barbara Kornblum
P.O. Box 808, L-140
Livermore, CA 94550

1   Logicon RDA
Attn: Art Barondes
6940 South Kings Highway, Suite 210
Alexandria, VA 22310

1   Los Alamos National Laboratories
Attn: Ron Flurry
P.O. Box 1663, MSC931
Los Alamos, NM 87545

1   Los Alamos Technical Associates
Attn: Lou Reidl
2400 Louisiana Blvd. NE
Building 1, Suite 400
Albuquerque, NM 87110

1   Massachusetts Institute of Technology
Attn: Professor A. Ghoniem
Room 3-342
77 Massachusetts Ave.
Cambridge, MA 02139

1   National Center for Atmospheric Research
Attn: Terry Clark
Mesoscale & Microscale Meteorology Division
3450 Mitchell Lane
P.O. Box 3000
Boulder, CO 80307

3   National Institute of Standards and Technology
Attn: D. Evans, R. Gann, K. McGratten
Fire Science Division
BFRL, Building 224
Room B250
Gaithersburg, MD 20899

1   Commander
Naval Air Warfare Center
Attn: Doug Murray
Code 528200D
China Lake, CA 93555

1   Commander
Naval Air Warfare Center - Weapons Division
Attn: Leo Budd
Code 418300D
China Lake, CA 93555-6001

1   Commander
Naval Air Warfare Center - Aircraft Division
Attn: Bill Leach
Code 43520, B562-3
Lakehurst, NJ 08733-5100

1   NWI
Attn: Col. John Curry, Technical Director
1651 First Street SE
Kirtland AFB, NM 87117

1   NWI
Attn: Dr. Dermod Kelleher, Technical Director
1651 First Street SE
Kirtland AFB, NM 87117

1   NWIE
Attn: Michael Martinez
1651 First Street SE
Kirtland AFB, NM 87117

1   PLG Inc.
Attn: David Johnson
4590 MacArthur Blvd. Suite 400
Newport Beach, CA 92660

2   Purdue University
Attn: Prof. J. P. Gore, Prof. S. Frankel
Thermal Sciences and Propulsion Center
West Lafayette, IN 47907-1003

2   SINTEF/Norwegian Institute of Technology
Attn: J. Holen, B. Magnussen
Applied Thermodynamics
Kolbjorn, Hejes Vei 1B
Trondheim, Norway N-7034

1   TRW Inc.
Attn: Kiran Magiawala
Space and Technology Division, MS R1-1062
One Space Park
Redondo Beach, CA 90278

1   University of Connecticut
Attn: Professor B.M. Cetegen
Department of Mechanical Engineering
191 Auditorium Rd.
Storrs, CT 06269-3139

1   University of Kentucky
Attn: Professor K. Saito
Department of Mechanical Engineering
Lexington, KY 40506

2   University of Michigan
Attn: Prof. G.M. Faeth, Prof. J.F. Driscoll
Department of Aerospace Engineering
1320 Beal Ave., 3000 Francios-Xavier Bagnoud Bldg.
Ann Arbor, Mi 48109-2118

1   University of Notre Dame
Attn: Professor K.T. Yang
Aerospace & Mechanical Engineering Dept.
Notre Dame, IN 46556

1   University of Texas at Austin
Attn: Professor O.A. Ezekoye
Department of Mechanical Engineering
ETC 7.130
Austin, TX 78712

1   VTT
Attn: Olavi Keski-Rahkonen
Fire Technology Laboratory
Kivimiehentie 4
Espoo, Finland SF-02150

1   Weidlinger Associates
Attn: H. Levine
4410 El Camino Real, Suite 110
Los Altos, CA 94022

1   Wright Laboratories
Attn: M. Bennett
FIVS Bldg. 63
1901 Tenth Street
Wright Patterson Air Force Base, OH 45433-7605

1   Wright Laboratories
Attn: M. Roquemore
POSC Bldg. 490
1790 Loop Road N.
Wright Patterson Air Force Base, OH 45433-7103

1	MS0427	W.R. Reynolds, 2103
1	MS0715	C.E. Olson, 6606
1	MS9042	C.M. Hartwig, 8345
1	MS9042	G.H. Evans, 8345
1	MS9042	C.D. Moen, 8345
1	MS9042	W.S. Winters, 8345
1	MS9056	L.A. Rahn, 8351
1	MS9051	W.T. Ashurst, 8351
1	MS9051	J. Chen, 8351
1	MS9051	A.R. Kerstein, 8351
1	MS9051	R.W. Schefer, 8351
1	MS0841	P.J. Hommert, 9100
2	MS0828	R.D. Skocypec, 9102
1	MS0826	W.L. Hermina, 9111
1	MS0826	S.N. Kempka, 9111
1	MS0826	J.A. Schutt, 9111
1	MS0834	A.C. Ratzel, 9112
1	MS0834	M.J. Martinez, 9112
1	MS0835	T.C. Bickel, 9113
1	MS0835	S.P. Burns, 9113
1	MS0835	R.J. Cochran, 9113
1	MS0825	A.R. Lopez, 9115
1	MS0825	F.G. Blottner, 9115
5	MS0835	C.W. Peterson, 9116
10	MS0835	S.R. Tieszen, 9116
1	MS0836	L.A. Gritzo, 9116
1	MS0836	J.H. Strickland, 9116
1	MS0836	V.F. Nicolette, 9116
1	MS0819	M.A. Christon, 9231
1	MS0819	E.A. Boucheron, 9231
1	MS1111	R.C. Schmidt, 9221
1	MS1111	J.N. Shadid, 9221
1	MS0507	K.G. McCaughey, 9700
5	MS0865	J.L. Moya, 9735

1	MS0865	T.Y. Chu, 9735
1	MS0865	W. Gill, 9735
1	MS0429	W.C. Nickell, 12300
1	MS0492	P.E. D'Antonio, 12324
1	MS0492	G.A. Sanders, 12332
1	MS0405	D.D. Carlson, 12333
1	MS0405	M.K. Fuentes, 12333
1	MS0405	T.R. Jones, 12333
1	MS9018	Central Technical Files, 8523-2
5	MS0899	Technical Library, 4414
2	MS0619	Review and Approval desk, 12630 For DOE/OSTI